VAVRINA, GERARD AMBROSE. Resonance Spectroscopy of the ^{29}Si(p,γ)^{30}P Reaction. (Under the direction of Dr. G. E. Mitchell and Dr. E. F. Moore.)

The excitation functions of the ^{29}Si(p,γ)^{30}P, ^{29}Si(p,p$_1\gamma$)^{29}Si and ^{29}Si(p,p)^{29}Si reactions were measured in the energy range $E_p = 1.0 - 2.0$ MeV. The gamma-ray decay of 17 resonances in the ^{29}Si(p,γ) reaction was measured in the range $E_p = 1.04 - 1.75$ MeV. This research was performed at the High Resolution Laboratory (HRL) at Triangle Universities Nuclear Laboratory. The motivation for these measurements was the result of a study of the fluctuation properties of ^{26}Al, which indicated partially chaotic dynamics at all excitation energies. The work presented in this dissertation was performed to provide experimental data on the fluctuation properties of ^{30}P. Specifically, this work represents a major step toward the goal of determining a pure and complete level scheme of ^{30}P for excitation energies up to 8820 keV.

A proton beam with an energy resolution of approximately 220 eV was used for the excitation function measurements. New resonances at $E_p = 1.0380$, 1.4333, and 1.5787 MeV were identified in the ^{29}Si(p,γ) reaction. The absolute strengths of 21 resonances in the ^{29}Si(p,γ) excitation functions were measured.

The gamma-ray decay measurements were performed with a Compton-suppressed HPGe gamma-ray detection system. Analysis of the gamma-ray spectra of 17 resonances yielded excitation energies and branching ratios for each resonance. Angular momentum and parity selection rules and a comparison of reduced transition strengths to recommended upper limits restricted the possible spin J, parity π, and isospin T assignments of each resonance. Excitation energies, branching ratios, and $J^\pi;T$ assignments were determined for 3 previously unobserved resonances. Previous unambiguous quantum number assignments for five of the resonances were confirmed. Of these seventeen resonances studied, 10 were assigned a definite J, 12 a definite parity, and 6 a definite T. The results of this work also indicated the need for angular distribution measurements on several resonances to remove remaining ambiguities.

RESONANCE SPECTROSCOPY OF THE $^{29}Si(p,\gamma)^{30}P$ REACTION

by

GERARD AMBROSE VAVRINA

A dissertation submitted to the Graduate Faculty of
North Carolina State University
in partial fulfillment of the
requirements for the Degree of
Doctor of Philosophy

Department of Physics

Raleigh
1996

APPROVED BY:

_____	_____
_____	_____
Co-chair of Advisory Committee	Co-chair of Advisory Committee

Dedication

to Dad and Mom

Biography

Gerard Ambrose Vavrina

Personal:

Born 14 November 1967 Baltimore, MD

Education:

B.S. in Physics, Loyola College, 1989

M.S. in Physics, North Carolina State University, 1991

Military:

1LT U.S. Army May 1992 - present

Educational Delay Program 21 May 1989 - present

Commissioned 2LT U.S. Army 21 May 1989

Memberships:

Sigma Pi Sigma

American Physical Society

Abstracts:

"A High-Resolution Study of ^{30}P", P. M. Wallace, E. G. Bilpuch, G. E. Mitchell, E. F. Moore, J. F. Shriner, Jr., G. A. Vavrina, and C. R. Westerfeldt, Bull. Am. Phys. Soc. **41**, 984 (1996)

"A Compton-Suppressed Spectrometer for the Study of ^{29}Si(p,γ)", G. A. Vavrina, E. G. Bilpuch, C. R. Bybee, J. M. Drake, G.E Mitchell, E. F. Moore, J. F. Shriner, Jr., P. M. Wallace, C. R. Westerfeldt, Bull. Am. Phys. Soc. **39**, 8 (1994)

"A High-Resolution Study of the ^{29}Si(p,γ) Reaction" P. M. Wallace, E. G. Bilpuch, C. R. Bybee, J. M. Drake, G.E Mitchell, E. F. Moore, J. F. Shriner, Jr., G. A. Vavrina, C.

R. Westerfeldt, Bull. Am. Phys. Soc. **39**, 8 (1994)

"A Beam Characteristics Study of an RF Ion Source", G. A. Vavrina, C. R. Jackson, G. E. Mitchell, E. G. Bilpuch, and C. R. Westerfeldt, Bull. Am. Phys. Soc. **36**, 2731 (1991)

"Evaluation of a New ECR Ion Source for a Single-Ended Van de Graaff Accelerator", C. R. Jackson, G. A. Vavrina, G. E Mitchell, E. G. Bilpuch, and C. R. Westerfeldt, Bull. Am. Phys. Soc. **36**, 2731 (1991)

Acknowledgements

An immense amount of dedication on the part of many people contributed to the research presented in this dissertation.

I would like to express deepest appreciation to my advisors Dr. Gary Mitchell and Dr. Frank Moore. I have benefited greatly from the knowledge and experience I gained from Dr. Mitchell throughout my graduate career. I greatly appreciate the enthusiastic support and vital assistance of Dr. Moore throughout this project.

I am greatly indebted to Dr. John Shriner for his invaluable advice and insight throughout all phases of this work.

I thank Dr. Russell Roberson for his commitment to this research and to the High Resolution Laboratory. I sincerely appreciate the interest and advice of Dr. Edward Bilpuch during this project.

I would like to thank Sidney Edwards and Patrick Mulkey for their expert maintenance and repair of the various electronics used in these experiments.

I especially thank Chris Westerfeldt for his expert guidance with all operations of the High Resolution Laboratory. I greatly appreciate his patience, which I'm sure I often tested, and his commitment to this project. I thank Paul Carter and Richard O'Quinn for their tireless efforts in the repair and maintenance of HRL equipment.

I greatly appreciate the essential efforts of Dr. Paul Wallace, Amzie Adams and Matt LaBonte in assisting with the collection of my thesis data. Thanks also to Lynne Fittje, Chris Grossmann, Suzanne Huerth, Joey Hutchins, Lance McLean, and Dr. Joann Shriner for their help with data collection. I wish to also express my thanks to Dr. Randy Bybee, Bret Crawford, Lisa Lowie, and Dr. Sharon Stephenson for the many helpful discussions and continual support throughout my graduate work.

I wish to deeply express thanks to Mom and Dad, Kathy and Kevin, and Thuy, whose love and understanding were always a welcome source of encouragement.

This work was supported by the United States Department of Energy.

Contents

List of Tables

List of Figures

Chapter 1

Introduction

Statistical nuclear spectroscopy has enjoyed a rebirth in the last decade due to immense interest in the behavior of chaotic quantum systems and tests of symmetry breaking. The statistical approach to the nuclear system concedes that, due to its complexity, a detailed description of the dynamics of a highly excited system is not possible. Rather, statistical spectroscopy attempts to explain the average behavior of a nuclear system in which a large number of particles interact within an unknown potential. The fluctuations about this average behavior then reveal new features of the nuclear system and are used for tests of quantum chaos and of symmetry breaking.

The focus on the statistical properties of energy levels in the nuclear system studied in this work is embodied in the Gaussian Orthogonal Ensemble (GOE) of Random Matrix Theory (RMT). In analogy to statistical mechanics, an ensemble of random Hamiltonian matrices is introduced. Each matrix $\mathcal{H}$ represents a possible Hamiltonian that describes equally probable interactions between particles within the system. The ensemble is defined by Time Reversal Invariance (TRI) and rotational symmetry, which constrain each $\mathcal{H}$ to be a real symmetric matrix. The independent elements of $\mathcal{H}$ are assumed statistically independent of each other, which results in a Gaussian distribution of those matrix elements. The GOE is the ensemble of matrices that follow the above criteria.

The GOE as applied to nuclear physics was established by the pioneering work of Wigner [Wig57] and of Dyson and Mehta [Dys63]. Statistical properties of nuclear spectra

are obtained by computing averages of certain quantities (such as level spacings, reduced widths, etc.) over the GOE ensemble and examining fluctuations about those averages. Since the GOE does not account for the specific properties of the nuclear Hamiltonian, the fluctuation properties of a system about some average are generic in nature and so are expected to be broadly applicable. The GOE of RMT thus makes general, parameter-free predictions of the expected behavior of the fluctuation properties of a nuclear system.

The predictions of RMT are used in the investigation of the poorly understood criteria for chaos in quantum systems. A useful approach to this investigation is the study of quantum analogs of systems whose classical behavior is known to be chaotic. This approach was used by Bohigas et al. [Boh84] in a study of the fluctuations of the quantized energy levels of Sinai's billiard. These fluctuations were found to be consistent with the predictions of the GOE of RMT. In addition, Bohigas conjectured that *all* quantum analogs of TRI chaotic classical systems have fluctuation properties that obey the GOE statistics [Bro81] of RMT. This conjecture sparked much interest since it established a connection between fluctuation properties of a quantum system and the underlying degree of chaos of the system. An extensive amount of analytical and numerical tests have supported the validity of this conjecture. In addition, other calculations have supported the ansatz that systems whose analogs are regular obey Poisson statistics. It is therefore important to test the predictions of GOE as observed by the fluctuation properties of a quantum system in as many different systems as possible. Nuclear energy levels within a compound nucleus provide the best empirical tests of the GOE of RMT to date.

The fluctuation properties of a nuclear system are investigated using certain statistical measures. The Dyson-Mehta Δ_3 [Dys63] statistic examines the long-range order, or spectral rigidity, of a set of energy levels characterized by the same symmetries (this set is called a "sequence"). This order is a key prediction of the GOE of RMT. The linear correlation coefficient ρ examines the correlations (or absence of) between adjacent spacings in a particular system. For a detailed description of the application of these two statistics to nuclear systems, see Porter [Por65]. The most common statistic is the nearest neighbor spacing (NNS) distribution for a sequence of energy levels, which reveals the short range

order of a system. For convenience, this distribution is expressed in terms of $x = s/D$, where s is the spacing between adjacent energy levels and D is the average spacing of the levels in the sequence. Fig. 1.1 shows NNS distributions with Poisson and GOE statistics.

For the GOE, this NNS distribution is essentially a Wigner distribution

$$P(x) = \frac{\pi}{2} x e^{-\frac{\pi}{4}x^2}. \tag{1.1}$$

This type of distribution manifests another key prediction of the GOE that levels within a sequence tend to repel each other. Note that this "level repulsion" is demonstrated by this NNS distribution approaching zero as x approaches zero. A system that follows GOE statistics therefore disallows any degeneracies within a sequence.

A NNS distribution that obeys Poisson statistics depends on x as

$$P(x) = e^{-x}. \tag{1.2}$$

This distribution describes a random system of uncorrelated energy levels with no special symmetries, such as the nuclear spin and parity (J^π). Systems that follow Poisson statistics allow degeneracies, in fact, $s = 0$ is the most probable level spacing here. An empirical interpolation formula developed by Brody [Bro73] often is used for describing spectra that fall between the GOE and Poisson extremes.

The GOE places stringent conditions on the quality of data used for these statistical measures. The appropriate sequences must be both pure (few or no misassigned levels) and complete (few or no missing levels). Any mixing of levels with different quantum numbers within a sequence tends to cause the NNS distribution to approach a Poisson distribution. At the time of the development of the GOE model, the quality of data was such that statistical analyses of the best available data "neither proved or disproved" [Dys62] this model. Not until the early 1970's, with the data of Liou et al. [Lio72] and the later work of Watson et al. [Wat81] could the predictions of the GOE of RMT be tested. In addition, a collection of neutron resonances in heavy nuclei and proton resonances in the f-p shell (called the Nuclear Data Ensemble) were found to be consistent with the predictions of the GOE of RMT [Haq82][Boh85].

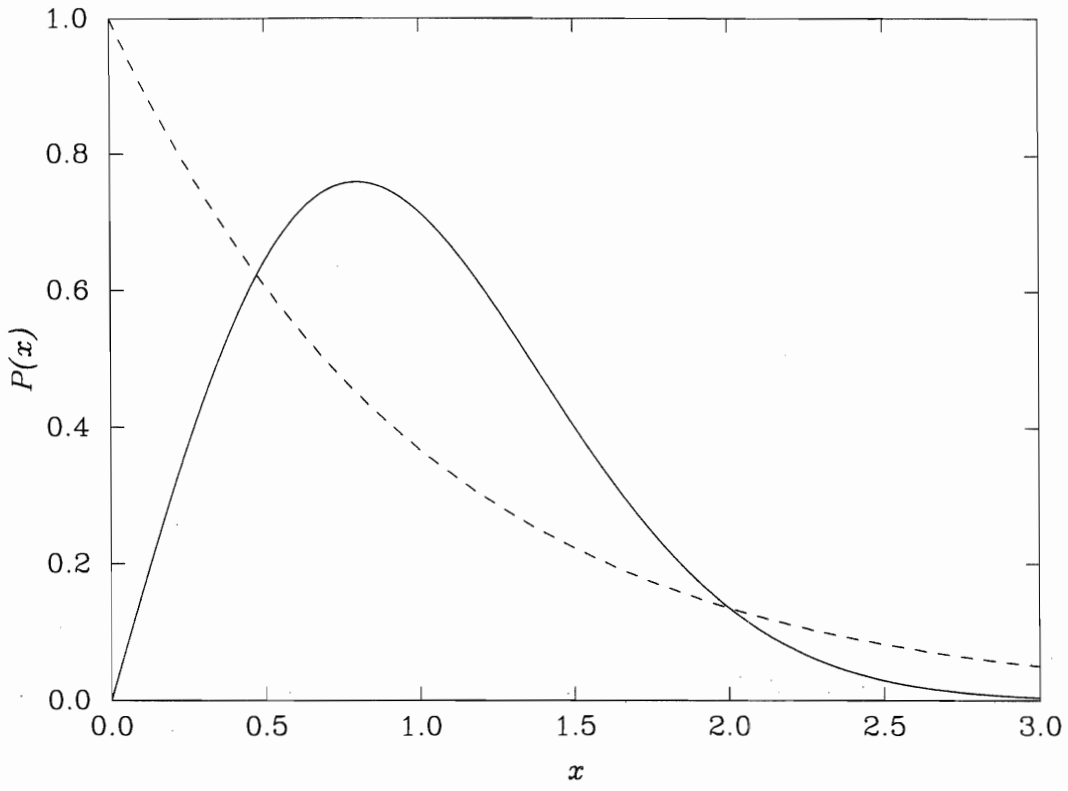

Figure 1.1. The NNS distribution for GOE and Poisson statistics. The Poisson distribution is the dashed curve, and the GOE is the solid line.

Therefore, empirical tests of the GOE were extended into other regions of excitation energies and nuclear masses [Mit88]. Shriner et al. [Shr91] studied the fluctuation properties of low-lying states over an extensive mass region. The results of this study found that the lightest nuclei reflected GOE behavior and the heaviest nuclei reflected Poisson behavior. The behavior of the lightest masses was not surprising, since these nuclides are well described by the shell model, which generally agree with GOE statistics [Bro81]. However, the intermediate masses displayed a smooth transition from GOE to Poisson behavior. This movement toward Poisson behavior perhaps is due to the mixing into the overall sequence of the rotational quantum number K.

A study of the fluctuation properties of ^{26}Al was undertaken to test the GOE of RMT from the simple levels near the ground state through the complex levels of the resonance region [Mit88] [Shr90]. This nuclide was chosen since its level scheme represented the most

pure and complete data set at that time [End86] [End88a]. The 100 positive parity states (of the 160 total states) were used, since a shell model comparison to these states existed. Mitchell and Shriner [Shr90] found that the fluctuations were intermediate between GOE and Poisson statistics.

In addition, these tests on the ^{26}Al nuclide were the first experimental tests of the predictions of the GOE for isospin symmetry breaking. A surprising result of this study was that an examination of the NNS distributions for the 100 levels of both $T = 0$ and $T = 1$ and for the 75 levels of $T = 0$ gave the same result. Since isospin is considered an almost perfect quantum number ($\sim$ 97% in ^{26}Al), different results were expected for these two sequences. This result can be understood from the fact that even a small breaking of a symmetry causes the same characteristic fluctuations as when that symmetry is absent [Pan81]. This behavior was confirmed theoretically by Guhr and Weidenmüller [Guh90] specifically for isospin. Guhr and Weidenmüller also calculated the Coulomb mixing matrix element (since the Coulomb interaction mixes the levels of different isospin), which agreed with the earlier measurements of Simpson [Sim78]. This was the first empirical test of the sensitivity of a fluctuation property (here the NNS distribution), to the breaking of a symmetry (here isospin).

However, the ^{26}Al spectrum is too limited to establish definitively this explanation. The additional data needed for this purpose must meet the same requirements as ^{26}Al. Self-conjugate nuclei such as $^{26}_{13}$Al contain states of different isospin co-existing over an energy range from the ground state through the resonance region. The level density should be sufficient for good statistics, but sparse enough to allow adjacent levels to be resolved. A low proton separation energy, S_p, minimizes the number of levels that are within the difficult region surrounding S_p. In the mass region near ^{26}Al, the best candidates are ^{22}Na, ^{30}P, ^{34}Cl, and ^{38}K. The Na and K nuclides require gas targets, which is not compatible with the existing High Resolution laboratory (HRL) system. Of the two remaining nuclides, ^{30}P met all the above criteria and required the target (^{29}Si) that was easiest to fabricate.

The work presented in this thesis is part of several experimental studies performed within the HRL group of the Triangle Universities Nuclear Laboratory (TUNL) to establish

a pure and complete level scheme for ^{30}P from the ground state through the resonance region ($E_x \leq 8020$ keV). The research at the HRL was undertaken both to confirm and to augment the existing spectroscopic knowledge of ^{30}P obtained from various studies over the past thirty years. Elastic scattering measurements are useful for locating energy levels and assigning J and π to levels above S_p. Therefore, this effort began with the elastic scattering experiments of Nelson [Nel83b] and Frankle [Fra91], which covered $E_p = 0.94 - 3.3$ MeV. The capture reaction excitation function and γ-ray decay data of Reinecke et al. [Rei85] covered the proton energy range of $E_p = 0.3 - 2.3$ MeV. Frankle [Fra91] then remeasured this excitation function in the proton energy range $E_p = 2.0 - 3.0$ MeV using the higher resolution HRL system and located several new resonances. Therefore, the first phase of the work presented in this dissertation consisted of a measurement of the ^{29}Si(p,γ) excitation function from $E_p = 1.0 - 2.0$ MeV to augment the data of Frankle.

Studies of the gamma-ray decay from (p, γ) resonances are useful for investigating resonant levels and bound levels. An analysis of the strengths of these γ-ray decays is useful for restricting the possible spin (J), parity (π), and isospin (T) assignments to a resonant level and also to the various bound levels populated by these decays. The combination of high-resolution gamma-ray detectors together with the excellent HRL proton beam energy resolution form a powerful system to meet the strict requirements of purity and completeness. Therefore, a Compton-suppressed Spectrometer System (CSS) using High Purity Germanium (HPGe) detectors described by Drake [Dra94] and Bybee [Byb95] was designed and implemented at the HRL. The sensitivity for the detection of weak γ-ray transitions by this detector system allows easier identification of energy levels and assignments of $J^\pi; T$. The second phase of this work thus consisted of collecting high-resolution gamma-ray decay data for 17 ^{29}Si(p,γ) resonances from $E_p = 1.04 - 1.75$ MeV.

Chapter 2 of this dissertation gives a brief overview of the relevant theoretical topics pertinent to this research. Chapter 3 describes the experimental arrangement for both phases of the measurements performed in this work. Chapter 4 presents the analysis and results of the excitation function measurements. Chapter 5 discusses the analysis and summarizes the results of the gamma-ray decay measurements. Chapter 6 summarizes

the results of the research presented in this dissertation. Appendices A and B present in tabular form the results of branching ratio measurements and of γ-ray strength analyses, respectively.

Chapter 2

Theory

This chapter frames the theoretical context of the experiments reported in this dissertation. Since the relevant theoretical topics discussed here are well established, expressions are given without proof. Section 2.1 describes the compound nucleus formalism used to describe the reactions studied in this research. Section 2.2 explains the differential cross section formula that characterizes the nuclear resonances investigated in these experiments. Section 2.3 focuses on the selection rules for the gamma-ray decay from the ^{30}P compound nucleus that restrict the J^{π} and T values of a particular state. Section 2.4 discusses the theoretical estimates of the transition probabilities (or strengths) of these gamma-ray decays.

2.1 Background

The observation of cross sections for slow neutrons that were much greater than nuclear dimensions [Fer34] provided the first experimental evidence of the phenomenon of nuclear resonances. A firm experimental foundation for these resonances was created by the subsequent work with proton resonances of Hafsted and Tuve [Haf35], as well as many other subsequent researchers. The existence of these well-isolated, sharp resonances indicated a lifetime of $\sim 10^{-15}$ seconds, much longer than the more typical duration of $\sim 10^{-21}$ seconds for other types of nuclear reactions.

Bohr [Boh36] developed the basis of understanding these resonances in the cross sections for nuclear reactions in terms of the virtual states of a nucleus. Bohr assumed that a nuclear reaction could be divided into two independent mechanisms: the formation of a compound system and the subsequent disintegration of the system into various reaction products. A typical reaction of the type studied in this work can then be described by a two-body interaction, $a + X \rightarrow C^* \rightarrow b + Y$. Here, a particle a incident on a target nucleus X forms the compound nucleus C^*, which subsequently decays into a residual nucleus Y and an exiting particle b.

The "Bohr assumption" was based on the premise that the interaction between the incident particle and the target nucleus was strong and of a short range. This strong interaction caused particle a, which came within range of this interaction, to quickly share its energy among the various target nucleons. It was therefore improbable that a single nucleon could escape from the compound nucleus, so a virtual or "quasi-stationary" state was created, with a lifetime τ_s, until the system eventually disintegrated into its reaction products. A resonance in the cross section for a particular reaction will occur near the energy of the incident particle for which this compound state was formed.

However, the finite lifetime of a particular level s in the compound nucleus causes an uncertainty in its energy, or width Γ^s [Bla91] given by

$$\Gamma^s = \frac{\hbar}{\tau_s}. \tag{2.1}$$

These levels of a compound nucleus excited by an incident proton, form a discrete spectrum above the proton separation energy, S_p, provided Γ^s is smaller than the distance to the neighboring levels. Due to their finite lifetimes, these discrete compound states have properties such as total angular momentum J, parity π, and isospin T that can be measured by nuclear scattering experiments.

2.2 Differential Cross Section

Following the "Bohr assumption", many efforts were made to theoretically describe the characteristics of resonance reaction cross sections. The formal theory for resonances was

well developed by the late 1950's. The elegant R-matrix theory of Wigner and Eisenbud [Wig47] accounted for the existence of resonances and described their cross sections with a small set of observables [Vog59]. An extensive description of R-matrix theory, including an extension to capture reactions is given by Lane and Thomas [Lan58]. Blatt and Biedenharn [Bla52] used the collision matrix formalism of Wigner and Eisenbud [Wig47] to derive a general expression for the differential cross section for resonance reactions. The cross section formula below is based on [Bla52] as modified by Huby [Hub54].

It is convenient to describe the various modes of formation and decay of a resonance as entrance and exit channels respectively. The entrance channel of a reaction involves three different angular momenta: a projectile spin $\vec{i}$, a target spin $\vec{A}$, and the relative orbital angular momentum $\vec{\ell}$ of the incident projectile and the target nucleus. The channel spin representation is used here to couple these angular momenta according to

$$\vec{J} = (\vec{i} + \vec{A}) + \vec{\ell} = \vec{s} + \vec{\ell}, \tag{2.2}$$

where $\vec{J}$ is the total angular momentum of the compound nucleus formed by the resonance reaction and $\vec{s}$ is the entrance channel spin. In this work, we are interested in capture reactions in which the compound state decays by the emission of gamma-rays of multipolarity $\vec{L}$ to a lower state $\vec{C}$. Therefore, the exit channel is characterized by the coupling of the residual nuclear spin $\vec{C}$ to the multipolarity $\vec{L}$ according to

$$\vec{J} = \vec{C} + \vec{L}. \tag{2.3}$$

For an unpolarized beam, the differential cross section can be written in this notation as

$$\begin{aligned} \frac{d\sigma}{d\Omega} &= \left(\frac{\lambda}{\hat{i}\hat{A}}\right)^2 \sum (-1)^{s-\ell_1+\ell_2-2J_2+C-L_1+L_2}\, \overline{Z}(\ell_1\, J_1\, \ell_2\, J_2; s\, k) \\ &\quad \overline{Z}_1(L_1\, J_1\, L_2\, J_2; C\, k)\, \langle C\, L_1 | S | J_1\, s_1\, \ell_1 \rangle \langle C\, L_2 | S | J_2\, s_2\, \ell_2 \rangle^* \\ &\quad Q_k P_k(\cos\theta). \end{aligned} \tag{2.4}$$

The summation here is over s, C, ℓ_1, ℓ_2, L_1, L_2, J_1, J_2, and k; the quantity $\hat{a}$ is $\sqrt{2a+1}$. Equation 2.4 represents an average over initial spin directions and a sum over the final

states. The subscripts (1) and (2) on certain quantities of Equation 2.4 represent values for two possible paths through the resonance reaction. For example, an isolated resonance would have $J = J_1 = J_2$. The variable λ is the reduced wavelength of the projectile, θ is the angle between the direction of the incident beam and the axis of the γ-ray detector and Q_k is a correction for the finite size of the detector as defined by Ferguson [Fer65]. P_k is a Legendre polynomial of degree k.

The dependence of the cross section on the coupling of the various angular momenta in the entrance and exit channels are contained in the $\overline{Z}$- and $\overline{Z}_1$-coefficients, respectively. The $\overline{Z}$-coefficient is essentially the Z-coefficient defined by Blatt and Biedenharn [Bla52] as modified by Huby [Hub54]. The $\overline{Z}_1$-coefficient is a modification [Bie60] of the Z_1-coefficient [Sha54] for the case of gamma-rays in the exit channel. These coefficients contain the various angular momentum coupling terms that give the probability of forming a specific state such as J_1 from ℓ_1 and s and likewise for J_2 [Bie60]. Therefore, for example, conservation of angular momentum requires that $\vec{J}_1 = \vec{\ell}_1 + \vec{s}$ and $\vec{J}_2 = \vec{\ell}_2 + \vec{s}$; otherwise the $\overline{Z}$-coefficient is zero.

The elements of the scattering matrix $\langle C\, L\, |S|\, J\, s\, \ell \rangle$ [Wig47] contain the dynamics of a specific reaction. These matrix elements are given (in the single-level approximation) by

$$\langle C\, L\, |S|\, J\, s\, \ell \rangle = \frac{e^{i\xi_\ell} g_{Js\ell} g_{CL}}{(E - E_{res}) - i(\frac{\Gamma}{2})}, \tag{2.5}$$

where the squares of g_{Jsl} and g_{CL} are the partial widths of the entrance and exit channels, respectively, of a particular reaction. The total width Γ is given by the sum over N open channel widths given by

$$\Gamma = \sum_{\alpha=1}^{N} \Gamma_\alpha. \tag{2.6}$$

The term ξ_ℓ is the Coulomb phase shift, which survives in Equation 2.4 when different values of ℓ contribute to a given entrance channel spin (ℓ-mixing). Substitution of the elements of the scattering matrix of Equation 2.5 into Equation 2.4 for a single, isolated resonance then produces the familiar Breit-Wigner shape of a resonance observed in the laboratory (see Chap. 4).

2.3 Radiative Transitions

This research is primarily concerned with the study of the transitions between two states of ^{30}P accompanied by the emission of a gamma-ray. It is useful to classify this emitted radiation according to its angular momentum $\vec{L}$ (with a z-component m) and its parity. For each unit of angular momentum of the radiation, two types are possible: electric and magnetic. The electromagnetic field of the compound nucleus ^{30}P can then be expanded in a complete set of electric and magnetic multipoles. Gamma-rays are then considered as multipole radiation of multipolarity L emitted from the oscillating components within the compound nuclear system. For the derivation of the multipole expansion of the electromagnetic field see Blatt and Weisskopf [Bla91]. The transitions between two states via γ-ray emission must obey conservation of total angular momentum and parity. These conservation principles give rise to selection rules, which govern the possible multipolarity type of the emitted radiation. In addition, transitions can be characterized by the isospin of the initial and final states, T_i and T_f. This symmetry also leads to selection rules, that help determine possible gamma-ray transitions.

2.3.1 Angular Momentum and Parity Selection Rules

Consider a single quantum of multipole radiation with an angular momentum of magnitude $\sqrt{L(L+1)}\hbar$ and z-component $m\hbar$. The compound nucleus emits this multipole $\vec{L}$ in a transition from an initial state of angular momentum $\vec{J}_i$ to a final state of $\vec{J}_f$ such that the total angular momentum of the system is conserved,

$$\vec{J}_i = \vec{J}_f + \vec{L}. \tag{2.7}$$

This selection rule thus associates multipole radiation of order L with the angular momentum difference between the initial and final states. Equation 2.7 then implies that a multipole of order L may only be emitted provided that

$$|J_i - J_f| \leq L \leq J_i + J_f. \tag{2.8}$$

Equation 2.8 demonstrates that the angular momentum values J_i and J_f of the states involved in the transition generally permit several orders of multipoles to be emitted.

However, if $J_i = 0$ or $J_f = 0$, only pure multipole radiation of a specific type is allowed. Also, since no multipole radiation of order $L = 0$ exists, gamma-ray transitions cannot occur between states with $J_i = J_f = 0$.

Gamma-ray transitions must also conserve parity. The electric and magnetic radiation emitted in a particular transition are distinguished by their angular momentum and by their parity. Electric multipole radiation of order L, (EL) and magnetic radiation, (ML), have opposite parity [Sie87],

$$\pi(EL) = (-1)^L = -\pi(ML). \tag{2.9}$$

Therefore, the type (electric or magnetic) of emitted multipole radiation is related to the relative parity of the initial and final states. Parity conservation can then be expressed in terms of the parity of the initial π_i and final π_f states as [Bla91]: $\pi_i = \pi_f$ for even EL and odd ML radiation, $\pi_i = -\pi_f$ for odd EL and even ML radiation. These selection rules do not permit simultaneous emission of electric and magnetic radiation of the same order L from a compound nucleus. When simultaneous EL and ML emission does occur, the radiation types will differ by one unit of multipolarity L.

2.3.2 Isospin Selection Rules

The selection rules for isospin assume that isospin is a good symmetry due to the charge independence of the nuclear force. However, this is only an approximate symmetry, since the Coulomb force mixes states of different isospin within the wavefunction describing a particular compound system. However, the isospin selection rules are generally valid for light nuclei, since the Coulomb energy is small compared with the total binding energy of the nucleus. The selection rules for a gamma-ray transition from a state of of isospin T_i to as state of isospin T_f are

$$|T_i - T_f| \equiv \Delta T = 0, \pm 1. \tag{2.10}$$

A second selection rule is used specifically for E1 transitions within self-conjugate nuclei (such as ${}^{30}_{15}P$). For this case, only transitions characterized by $\Delta T = \pm 1$ are allowed [Wil60]. This rule is only approximately true, since the "isospin forbidden" isoscalar transitions ($T_i = T_f$) are observed experimentally, although greatly suppressed in intensity.

2.4 Transition strengths

The conservation laws invoked to produce the selection rules discussed previously establish the connection between the multipolarity of the emitted radiation and the characteristics of the states involved in a given transition. This connection is then used to obtain additional information about these compound nuclear states by considering not just the possibility (as with selection rules) but the *probability* that a transition will occur. As described below, the probability of the emission of multipole radiation is directly related to the rate of emission of the energy of this radiation. This energy is intimately associated with the multipole moments produced by the charges and currents within the source of that radiation, the compound nucleus.

First consider a single nucleon of charge e and mass M (with no intrinsic spin) making the transition from an initial state φ_i to a final state φ_f. The current density operator $\vec{j}$ is then given by [Bla91]

$$\vec{j} = \frac{e}{2M}\left[\varphi_f^*(\vec{p}\,\varphi_i) + (\vec{p}\,\varphi_f)^*\varphi_i\right], \tag{2.11}$$

where $\vec{p} = -i\hbar\vec{\nabla}$ is the linear momentum operator of the nucleon. The nuclear charge density can be written as a function of the position of the nucleon $\vec{r}$ within the nucleus as

$$\rho = e\,\varphi_f^*(\vec{r})\varphi_i(\vec{r}). \tag{2.12}$$

Both current and nuclear charge density operators are periodic functions of time.

The nuclear currents and charge densities for a compound nucleus composed of Z protons and A total nucleons are then assumed to be the sum of the individual quantities of Equations 2.11 and 2.12 over all nucleons. Here, the nucleons are assumed point particles, moving independently within some potential well. A derivation that includes the small effects of the finite size of the nucleons is described by Bohr and Mottelson [Boh69]. The possibility of meson exchange and quark motion contributions to the multipole moments has also been neglected here. The various quantities given below are written in the long-wavelength limit : $\kappa R \ll 1$, where κ is the wavenumber of a photon and R is the radius of the compound nucleus. In other words, the wavelength of the multipole radiation is much greater than the dimension of the nucleus. This is a reasonable assumption for the energies

of the gamma-rays considered in this work.

The electric and magnetic multipole moments Q_{Lm} and M_{Lm} are related to the current and charge densities of a classical system according to [Bla91]

$$Q_{Lm} = \int r^L Y^*_{Lm}(\theta, \phi)\, \rho(\vec{r})\, dV \tag{2.13}$$

and

$$M_{Lm} = -\frac{1}{c(L+1)} \int r^L Y^*_{Lm}(\theta, \phi) \vec{\nabla} \cdot (\vec{r} \times \vec{j})\, dV. \tag{2.14}$$

The integration here extends over the volume of the charge distribution $\rho(\vec{r})$. Substitution of Equations 2.11 and 2.12 into these two equations give the matrix elements of the electric and magnetic multipole moments for a quantum system such as the compound nucleus. These are given by [Bla91]

$$\hat{Q}_{Lm} = e \sum_{k=1}^{Z} \int r_k^L Y^*_{Lm}(\theta_k, \phi_k) \varphi_f^* \varphi_i\, d\tau \tag{2.15}$$

and

$$\hat{M}_{Lm} = -\frac{1}{L+1} \frac{e\hbar}{Mc} \sum_{k=1}^{Z} \int r_k^L Y^*_{Lm}(\theta_k, \phi_k)\, \vec{\nabla} \cdot (\varphi_f^* \vec{L}_k \varphi_i)\, d\tau, \tag{2.16}$$

where κ is the wavenumber of the radiation. The operator $\vec{L}_k = -i\vec{r}_k \times \vec{\nabla}_k$ is the angular momentum operator. The single particle wavefunctions φ are now functions of both the radial position and spin coordinates of the nucleons within the compound nucleus. The angular dependence of these wave functions is contained in the spherical harmonic (Y_{Lm}) terms. The summation is carried out only over the protons since these matrix elements arise from the oscillating charges and currents within the nucleus.

In addition to the nuclear charges and currents, the spins of the nucleons cause an oscillating density of magnetization $\vec{M}$ within the nuclear volume that is an additional source of radiation. This magnetization causes the transitions between two compound states and is given by [Bla91]

$$\vec{M} = \frac{e\hbar}{2Mc} \mu \left[\varphi_f^*\, \vec{\sigma}\, \varphi_i \right]. \tag{2.17}$$

The terms in the brackets are summed over the two possible spin states of the nucleon and integrated over angular variables only. The quantity $\vec{\sigma}$ is the Pauli spin operator and μ

is the intrinsic magnetic moment ($= 2.78\mu_N$ for the proton; μ_N is a nuclear magneton) of a particular nucleon. The electric and magnetic multipole moments associated with this source of radiation are given by [Bla91]

$$Q'_{Lm} = -\frac{i\kappa}{L+1}\int r^L\, Y^*_{Lm}(\theta,\phi)\vec{\nabla}\cdot(\vec{r}\times\vec{M})\,dV. \tag{2.18}$$

and

$$M'_{Lm} = -\int r^L\, Y^*_{Lm}(\theta,\phi)\,\vec{\nabla}\cdot\vec{M}\,dV \tag{2.19}$$

Substitution of Equation 2.17 into these two equations gives the the electric and magnetic multipole matrix elements induced by this density of magnetization [Bla91],

$$\hat{Q}'_{Lm} = -\frac{i\kappa}{L+1}\,\frac{e\hbar}{2Mc}\sum_{k=1}^{A}\mu_k\int r_k^L\, Y^*_{Lm}(\theta_k,\phi_k)\,\vec{\nabla}\cdot(\varphi_f^*\vec{r}_k\times\vec{\sigma}_k\varphi_i)\,d\tau \tag{2.20}$$

and

$$\hat{M}'_{Lm} = -\frac{e\hbar}{2Mc}\sum_{k=1}^{A}\mu_k\int r_k^L\, Y^*_{Lm}(\theta_k,\phi_k)\,\vec{\nabla}\cdot(\varphi_f^*\vec{\sigma}_k\varphi_i)\,d\tau. \tag{2.21}$$

Note that these matrix elements are summed over all of the nucleons, since the magnetic moments (μ_k is for the k^{th} nucleon) of both neutrons and protons are included in these expressions.

These multipole matrix elements are related to transition probabilities through the Poynting vector and the amplitude of the multipole radiation. The Poynting vector determines the flow of energy in the multipole radiation and is defined as [Jac75]

$$\vec{S} = \frac{c}{4\pi}\vec{E}\times\vec{H}, \tag{2.22}$$

where $\vec{E}$ and $\vec{H}$ are the electric and magnetic fields of the radiation. These electric and magnetic fields can be expanded in a complete set of electric and magnetic multipoles of amplitudes $a_E(L,m)$ and $a_M(L,m)$ respectively. The magnitude of the Poynting vector $|\vec{S}|$ is proportional to the rate of emission of energy dU into a solid angle $d\Omega$ at the surface of the compound nucleus. Therefore, the energy emitted in pure multipole radiation of a certain type and amplitude $a_\Theta(L,m)$ can be written

$$dU_\Theta(L,m) = \frac{c}{2\pi\kappa^2}\,X^*_{Lm}X_{Lm}\,|a_\Theta(L,m)|^2\,d\Omega, \tag{2.23}$$

where $\Theta = E(M)$ for electric(magnetic) multipole radiation. The vector spherical harmonics terms X_{Lm} are orthogonal functions given by

$$X_{Lm} = \frac{\vec{L}Y_{Lm}(\theta,\phi)}{\sqrt{L(L+1)}}, \tag{2.24}$$

where $\vec{L}$ is again the angular momentum operator. The X_{Lm} terms within Equation 2.23 describe the angular distribution of the radiation, which is the same for electric and magnetic radiation of the same order and z-component [Bla91]. Integration of Equation 2.23 over 4π solid angle gives the total energy emitted per unit time, U_Θ,

$$U_\Theta(L,m) = \frac{c}{2\pi\kappa^2}\left|a_\Theta(L,m)\right|^2. \tag{2.25}$$

The amplitudes of the electric multipole radiation are related to the electric multipole matrix elements according to [Bla91]

$$a_E(L,m) = \frac{-4\pi\kappa^{L+2}}{(2L+1)!!}\left(\frac{L+1}{L}\right)^{1/2}\left(\hat{Q}_{Lm} + \hat{Q}'_{Lm}\right), \tag{2.26}$$

where $(2L+1)!! \equiv 1\cdot 3\cdot 5\cdots(2L+1)$. The corresponding amplitudes for the magnetic radiation are given by

$$a_M(L,m) = \frac{4\pi}{(2L+1)!!}\left(\frac{L+1}{L}\right)^{1/2}\left(\hat{M}_{Lm} + \hat{M}'_{Lm}\right). \tag{2.27}$$

Equations 2.26 and 2.27 then directly relate the amplitudes of a particular type of multipole radiation with the source of that radiation.

The division of the rate of emitted energy of Equation 2.25 by $E_\gamma = \hbar\omega$ discretizes the radiation emission to give the probability of emission of a single photon per unit time. This transition probability per unit time for one quanta of energy E_γ and multipolarity L can then be expressed in terms of multipole matrix elements using Equations 2.26 and 2.27 as [Wei51]

$$T_{fi} = \frac{8\pi(L+1)}{\hbar L[(2L+1)!!]^2}\left(\frac{E_\gamma}{\hbar c}\right)^{2L+1}\left|\hat{D}_{Lm} + \hat{D}'_{Lm}\right|^2, \tag{2.28}$$

where the gamma-ray energy $E_\gamma = \hbar c\kappa$. In this equation, $\hat{D}$ represents the the appropriate multipole matrix element for emission of either electric or magnetic multipole radiation. It

is customary to express Equation 2.28, in terms of the *reduced* transition probability B for a transition from a state of J_i to a state of J_f [Rin80],

$$T_{fi} \equiv \frac{\Gamma_\gamma}{\hbar} = \frac{8\pi(L+1)}{\hbar L[(2L+1)!!]^2}\left(\frac{E_\gamma}{\hbar c}\right)^{2L+1} B(\Theta L). \tag{2.29}$$

Here, Γ_γ is the gamma-ray width for the particular transition. The reduced transition probability (or strength) is therefore (from Equation 2.28) simply the square of the multipole matrix elements that describe the emission of radiation from the compound nucleus.

The kinematics term $(E_\gamma/\hbar c)^{2L+1}$ demonstrates a clear preference for the compound nucleus to decay (for a given multipole order) by more energetic gamma-rays. This term (for typical E_γ of this work) decreases dramatically with increasing multipole order L. The transition probability cannot be calculated exactly, since we do not know the exact form of the wave functions describing the initial and final states of a transition. However, predictions of the relative magnitudes of the transition probabilities for different types of multipole transitions are possible due to the sensitivity of Equation 2.29 to the order L.

Weisskopf [Wei51] derived theoretical estimates for T_{fi}, which aid in assigning quantum numbers to various ^{30}P states presented in this dissertation. Weisskopf assumed that the multipole radiation was accompanied by the transition of a single proton moving independently within a nuclear potential. The initial and final states of the proton were described by a wave function of the form [Wei51]

$$\varphi = u(r)Y_{Lm}(\theta, \phi). \tag{2.30}$$

This wave function was assumed constant within the radius R of the compound nucleus and zero for $r > R$. The spin of the proton was also neglected; estimates of T_{fi} with the spin included are given by Wilkinson [Wil60]. Therefore, from Equation 2.15 (with $k = 1$), the matrix element of the electric multipole moment is estimated [Bla91] as

$$\hat{Q}_{Lm} \approx \frac{e}{\sqrt{4\pi}}\left(\frac{3}{L+3}\right)R^L. \tag{2.31}$$

The contribution of the spins of the nucleons to the electric matrix elements, $\hat{Q}'_{Lm}$ can be neglected relative to the contribution of the nuclear charge density to $\hat{Q}_{Lm}$ [Wei51].

However, the magnitude of the orbital magnetic multipole moment, $\hat{M}_{Lm}$, is comparable to the magnitude of the spin magnetic multipole moment, $\hat{M}'_{Lm}$ [Jac75]. The factor $\vec{L}/(L+1)$ in Equation 2.16 is about three times the magnitude of $\mu\vec{\sigma}$ in Equation 2.21. The divergence of the appropriate terms in Equations 2.16 and 2.21 is estimated to be $\sim 1/R$. These estimates using wave functions of the form Equation 2.30 give [Bla91]

$$\frac{|\hat{M}_{Lm} + \hat{M}'_{Lm}|^2}{|\hat{Q}_{Lm}|^2} \approx 10 \left(\frac{\hbar}{McR}\right)^2. \tag{2.32}$$

Equations 2.31 and 2.32 are then used to produce expressions for the reduced transition strengths for electric and magnetic multipole radiation [Rin80],

$$B_W(EL) = \frac{e^2}{4\pi} \left(\frac{3}{L+3}\right)^2 R^{2L} \tag{2.33}$$

and

$$B_W(ML) = \frac{10}{\pi} \left(\frac{3}{L+3}\right)^2 R^{(2L-2)}\, {\mu_N}^2. \tag{2.34}$$

Here, the nuclear radius $R = (1.2)A^{1/3}$fm. Although these estimates are "exceedingly crude" [Wei51], they are useful since the transition probabilities are extremely sensitive to L. For instance, for gamma-ray energies less than 1 MeV, the transition probabilities for both electric and magnetic radiation change by a factor of 10^6 with a change of L of one unit of angular momentum [Sie87]. Although an excited compound state may be able to decay to several different final states, the state in question will prefer to decay to states that can be reached by emission of a gamma-ray with small L. In addition, magnetic radiation is about 100 times less probable than electric radiation of the same order [Sie87]. In transitions involving a mixture of multipoles, $M(L)$ radiation often successfully competes with $E(L+1)$. The specific use of these theoretical estimates with experimental data is discussed in Chap. 5.

Chapter 3

Experimental Equipment and Procedures

The research performed in the High Resolution Laboratory (HRL) at TUNL has utilized experimental systems with excellent beam energy resolution in order to produce precise nuclear structure data. Advances in technology have been utilized in modifications made since the introduction of the original design described by Parks and Williamson [Par58]. This high resolution system was automated in the early 1980's, which resulted in increased reproducibility and reliability of excitation function data, as well as greater ease of data acquisition. With the design of a new spectrometer system [Dra94], the system was further upgraded to include acquisition [Byb95] of high resolution gamma-ray decay data. The experiments described in this dissertation utilized this new system to acquire both excitation function and gamma-ray decay data.

3.1 Accelerator and Homogenizer Systems

This research was performed at the High Resolution Laboratory and utilized proton beams produced by a HVEC KN Van de Graaff accelerator. A detailed description of this accelerator and the associated system used to reduce fluctuations in the beam energy, the homogenizer system, is given by Westerfeldt et al. [Wes88][Wes95]. A brief overview is

given below.

A diagram of the accelerator and homogenizer system is shown in Fig. 3.1. The terminal of the accelerator contains a 165 MHz radio frequency (RF) ion source [Moa51][Rut51] which produces a high frequency gas discharge of hydrogen ions within a cylindrical Pyrex "bottle". These ions are then extracted from this "bottle", focused and accelerated into a beam of a given energy and separated into two ionic species by the analyzing magnet. The atomic H^+ beam is deflected 25° and subsequently steered and focused onto a ^{29}Si target at the gamma-ray chamber. The molecular HH^+ beam is deflected 17° into an electrostatic analyzer (ESA) in order to measure the fluctuations in the terminal voltage and ultimately to reduce the energy fluctuations of the atomic beam at the target.

For a given energy, the molecular beam is steered into the ESA and strikes a pair of vertically oriented slits, which are used as feedback slits for the corona stabilizer system and as object slits for the analyzer. Any changes in beam energy produce corresponding changes in the beam path through the stable field of the analyzing magnet. The resulting fluctuations in the position of the beam on the corona slits are thus used as a measure of the AC and DC components of the beam energy. The difference in currents striking the slits is formed into an error signal, which controls the amount of current flowing to a set of corona needles located between the dome and wall of the accelerator. Electrons emitted from these needles ionize a portion of the N_2 and CO_2 insulating gas molecules near the corona needles. The resulting negatively charged ions drift to the positive terminal and neutralize some of the positive charges there. The resulting redistribution of charges on the dome helps stabilize the terminal voltage. The variations in corona current as the terminal voltage changes thus provide a feedback signal used to reduce fluctuations of the terminal voltage and therefore of the beam energy.

The error signal input into the corona control circuit is often combined with a capacitive pickoff plate (CPO) signal to optimize the stability of the terminal voltage. The CPO consists of an electrically isolated metal plate located inside the accelerator vessel. The CPO signal is used to reduce the AC component of the terminal voltage in the absence of beam entering the ESA. In addition, when combined with the slit error signal, the

amplitude of the terminal voltage fluctuations are reduced from 5 – 10 kV_{p-p} to about 1 kV_{p-p}. However, the finite drift time of the ions between the corona needles and dome enables only low frequency (< 20 Hz) oscillations to be reduced, since this drift time causes a phase shift such that signals above ~20 Hz cannot be corrected [Ver78].

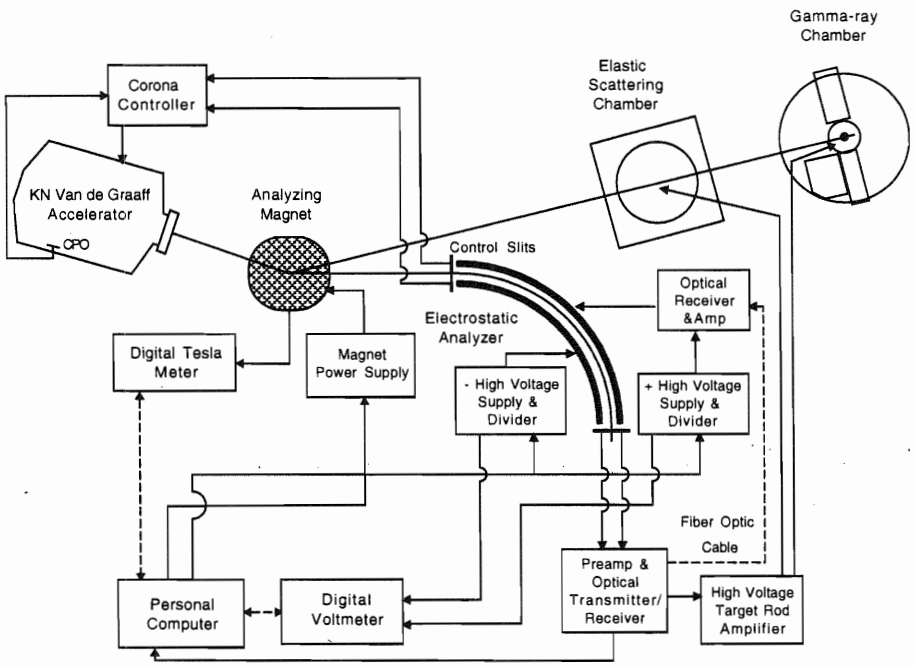

Figure 3.1. Feedback loops used in the High Resolution Laboratory.

After striking the corona control slits at the entrance to the ESA, the molecular beam radially accelerates between a pair of parallel 90° curved stainless steel plates, which are separated by 4.57 mm and biased at equal and opposite voltages. The geometry of the ESA is such that a beam of a given energy will be steered through the analyzer to a pair of exit (image) slits by a bias potential equal to the beam energy divided by 111.37. Changes in the terminal voltage produce corresponding changes in the beam position across the image slits. A slit difference signal is generated and amplified to give a real time measure of these fluctuations up to a maximum of ± 1.7 keV at 1 kHz. This signal is then fed back to the outer analyzer plate to maintain the molecular beam at the center of the analyzer plates. The slit difference signal is also amplified by 111.37 and applied to the target rod ladder

within the gamma-ray chamber to reduce the energy fluctuations of the incoming proton beam before it collides with the target. In addition, the DC component of this signal is used by the analyzing magnet control system to monitor incremental steps in beam energy (see Sect. 3.2.1).

3.2 Computer Control System

Control of the field produced by the analyzing magnet and the energy of the proton beam has been upgraded from an analog feedback system [Wes87] to a digital, computer-interfaced system [Wes95]. The new system centers around a PC 486 computer which utilizes the National Instruments graphical programming language LabView [Joh94]. LabView forms the basis of two separate digital feedback systems, which establish online monitoring and control of the analyzing magnet and ESA. These digital control systems thus provide high-resolution automated control for excitation function and gamma-ray decay data.

3.2.1 Analyzing Magnet Control System

Precise control of the analyzing magnet allows the molecular beam to be steered into the ESA, thus producing the corona error signal, and also allows reproducible, incremental changes of the beam energy. The control system for the analyzing magnet is shown in Fig. 3.2. A magnetic field is produced when a 16-bit word is output from the PC-DIO-24 I/O interface of the PC into a DAC circuit, which ramps a programmable power supply to the appropriate current to set the desired magnetic field. This field is then measured by a digital teslameter that is linked to a serial port of the PC as shown in Fig. 3.2. This system may be operated in two feedback modes: manual or slit mode.

Manual mode is normally used for initial tuning of the molecular beam into the ESA and throughout acquisition of gamma-ray decay data. Here, the desired magnetic field is set manually and then maintained at this field setting via a negative feedback loop created by a LabView PID (Proportional Integral Derivative) process controller. The difference between the current field setting and the desired value forms an error signal, which is used to generate an appropriate PID controller output to the PCD-IO-24 board. The PID

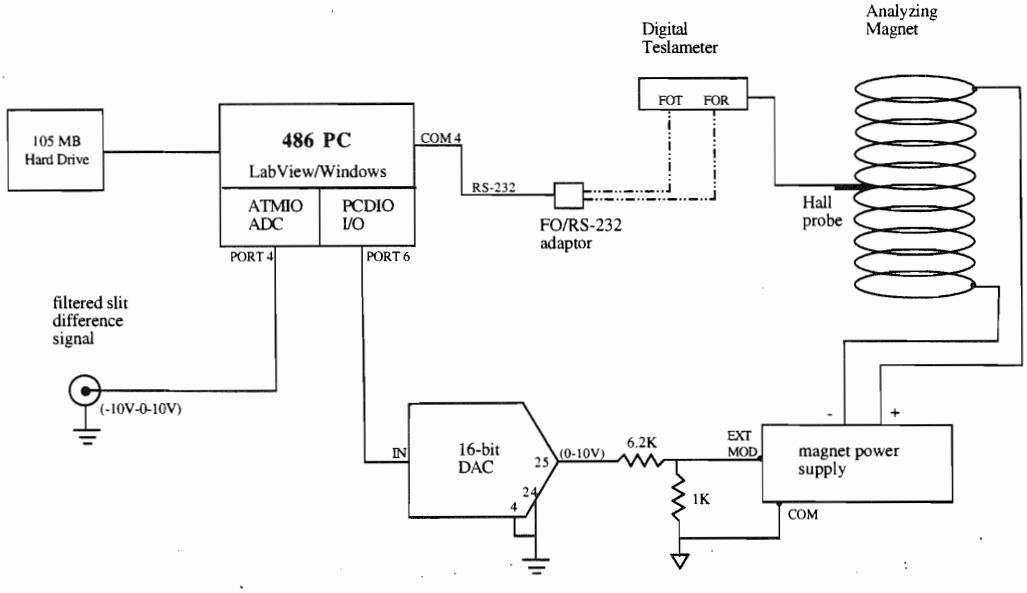

Figure 3.2. Analyzing magnet control system.

has been "tuned" [Cor90] to adjust the DAC output to a level that minimizes both the undershoot and overshoot from the desired field, so that the field will settle to the desired value as quickly as possible. The control loop executes every 1.5 seconds with an updated field value. This system will maintain a fixed field setting to within $\sim$ 0.004 %, allowing precise tuning of the molecular beam into the ESA as well as maintaining this beam at the center of the analyzer plates.

Slit mode is usually used when acquiring excitation function data, which requires multiple incremental steps over a large ($\sim$ MeV) energy range. Here, the proton beam energy is stepped to a new value E_p by setting a new ESA voltage equal to $E_p/111.37$ (see Sect. 3.2.2). This change in energy shifts the molecular beam between the analyzer plates off center and thus produces a non-zero filtered slit difference signal. This signal is then digitized by an AT-MIO-16X board ADC and input into a PID controller every 1.5 seconds. The PID signal is then input into a 16-bit DAC, which produces an appropriate output

that changes the magnetic field to shift the beam back to the center of the analyzer image slits. This new value of magnetic field also causes an imbalance in the current striking the corona control slits. The corona circuit corrects for this by adjusting the corona current to change the terminal voltage so that the slit currents are once again balanced. Thus, the terminal potential automatically tracks changes in the magnetic field.

3.2.2 ESA Control System

The ESA control system allows the experimenter to make highly accurate readings and settings of the beam energy. As shown in Fig. 3.3, a desired beam energy is sent as a character string via a serial line from a MicroVax 3200 (VAX) to the PC. This energy is then converted to a 32-bit word within a LabView program and sent to two 16-bit DAC's on the AT-MIO-16X board. Only the first 12 bits of the (HI)DAC are used due to the $\pm$ 4LSB resolution of the DAC's. The two DAC outputs are then summed to give 28-bit resolution and scaled to the 0 to -5 V range appropriate for input to two programmable analyzer plate power supplies. The voltage on the analyzer plates is thus ramped to a value corresponding to the desired beam energy. The resulting plate voltage is read by a $6-1/2$ digit resolution, programmable Digital Multimeter (DMM) as a voltage derived from the division of this plate voltage by precision resistor stacks. Therefore, DMM readings in the $0-4.4$ V range correspond to beam energies of $E_p = 0-4.4$ MeV.

The LabView control program uses a PID controller to compare the desired beam energy sent from the Vax to the actual beam energy read by the DMM and adjusts the PID controller output to the two DAC's accordingly. The PC continuously reads the serial line to the VAX for a new energy setting as well as reading the DMM every 400 ms to complete the feedback loop. In this manner, the molecular beam is kept centered between the analyzer plates. In addition, a tolerance of $\pm$ 31 eV is set on the beam energy, so that data acquisition is inhibited if the ESA voltage is outside this range.

The system described above gives better resolution than the previous design, but suffers from one shortcoming. Tests of this system using the 1.8841 and 1.8894 MeV resonances [Wim74] in ^{44}Ca(p,p) yielded a beam energy resolution of ~ 220 eV with an energy drift of

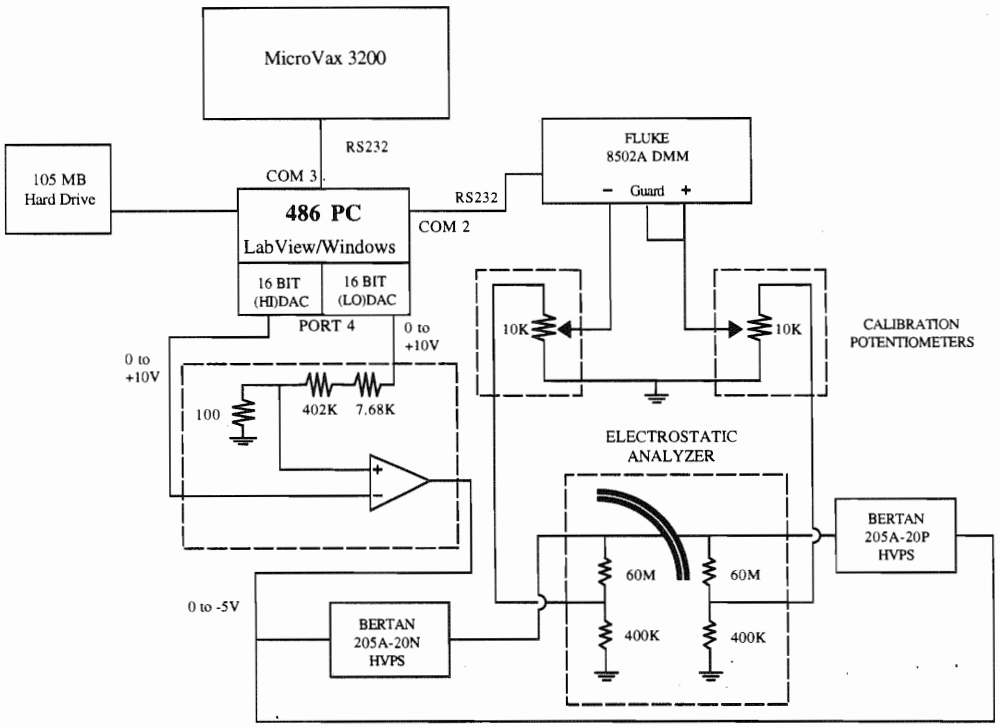

Figure 3.3. ESA control system.

$\sim$6 eV/hr. The beam energy resolution is dependent on the voltage of each analyzer plate in the ESA. With the single DMM used in this system, only the total potential difference between the plates is measured, which assumes that both power supplies have the same linearity over their entire range. If this assumption is not correct, then the electric field at the center of the plates would be non-zero and the resulting tangential acceleration of the beam would degrade the energy resolution. A solution to this problem is possible with the new multi-channel DMM's now commercially available. This new type of DMM would allow sampling of the voltages of each plate at the required sample rate and resolution to ensure both plate power supplies are tracking each other properly.

3.3 Scattering Chambers and Detectors

Two separate detector configurations were used for the experiments described in this dissertation. Excitation function data were acquired following the configuration of Frankle [Fra91]. Gamma-ray decay data were acquired using the new spectrometer system described in detail by Drake [Dra94]. A brief description of each configuration is given below.

3.3.1 Excitation Function Data Setup

A top view of the arrangement for the measurement of the (p,γ) excitation function is shown in Fig. 3.4. The same beam line and gamma-ray chamber of the Compton Suppression System (CSS) system (as shown in Fig. 3.5) were used for this measurement. The scattered photons were detected with two lead shielded, 7.62 cm $\times$ 7.62 cm NaI(Tl) detectors mounted on a circular stand surrounding the target chamber. Both detectors were oriented at laboratory angles of 55° and subtended solid angles of 1.16 and 1.82 sr. A silicon surface barrier (SSB) detector at 165° detected the scattered protons. The SSB detector subtended an angle of 1.32 msr with a resolution of 14 keV and an active area of 50 mm^2. A 300 μm depletion depth allowed detection of protons in the $(1-2$ MeV) energy range of the experiments. The target was oriented at 90° to give each detector a full view of the beam spot on the target. A turbo-molecular pump mounted below the chamber maintained a vacuum of $\sim 2\times10^{-6}$ Torr. This pump replaced the oil diffusion pump used in the previous chamber design and greatly reduced contamination of the target from oil vapors.

3.3.2 Gamma-ray Decay Data Setup

A diagram of the Compton-Suppressed Spectrometer (CSS) system is shown in Fig. 3.5. As indicated in the figure, the proton beam enters from the top of the figure and collides with a target at the center of the gamma-ray chamber. The target rod is biased at +3 kV and is capable of holding up to five targets and a tuning ring. The beam is collected at the end of the beamline by a Faraday cup equipped with secondary electron

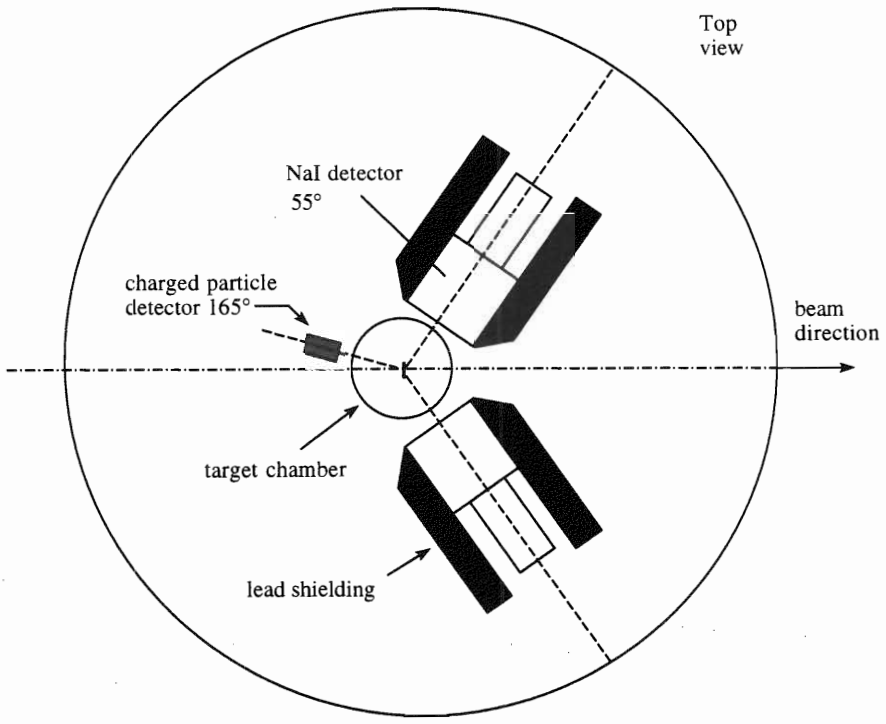

Figure 3.4. Excitation function data detector configuration.

suppression to ensure accurate charge collection. A semicircular table supports a shielded NaI(Tl) detector oriented at 140°, which is used to locate a given (p,γ) resonance. A 165° SSB detector attached to the gamma-ray chamber monitors the (p,p) reaction.

The two 60 % efficient High Purity Germanium (HPGe) detectors and an anti-coincidence Bismuth Germanate (BGO) suppression shield are the heart of the CSS system. The HPGe detectors have a measured energy resolution of ~ 1.9 keV at 1332 keV using a standard ^{60}Co calibration source. This is much better than the typical NaI(Tl) detector resolution of ~ 100 keV. Both HPGe detectors are equipped with LN_2 dewars, which maintain a constant 77 K temperature within the detectors to reduce leakage currents to tolerable levels. The BGO detector shown in Fig. 3.6 surrounds one of the HPGe detectors to detect the majority of those photons that deposit only a fraction of their full energy within the HPGe detector. These events are due to pair production and Compton scattering within

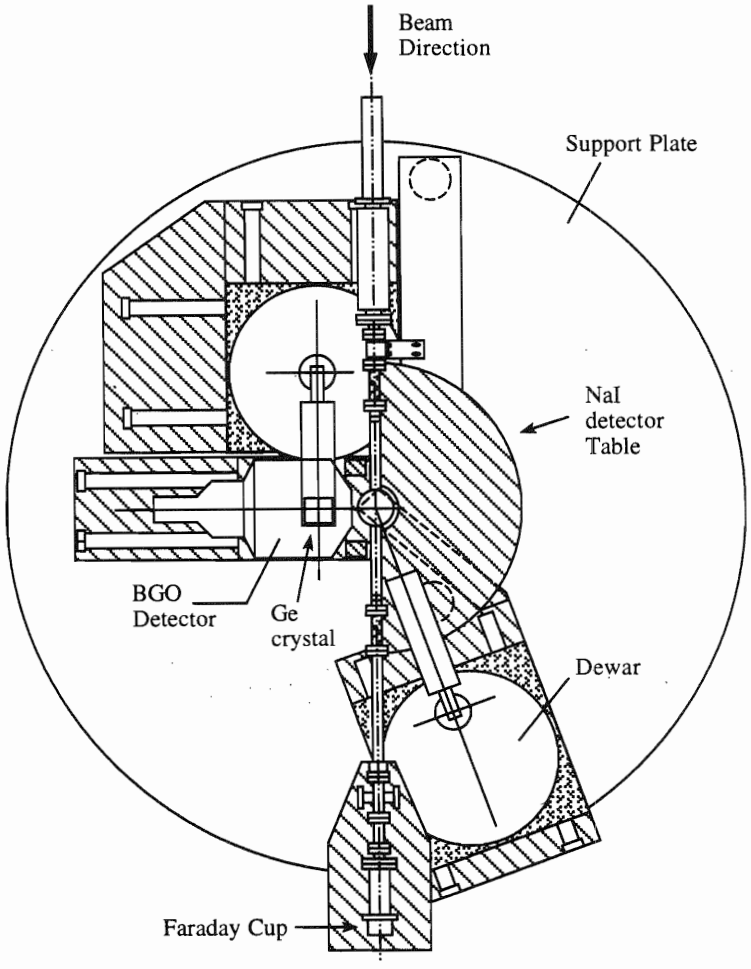

Figure 3.5. Top view of the CSS system used for gamma-ray decay experiments.

the detector, which cause spurious (escape) peaks and regions of high background within the gamma-ray spectra. The suppression of these processes takes place in the data acquisition hardware (see Sect. 3.4) by a veto of any events that produce simultaneous pulses in the BGO and HPGe detectors. The $Bi_4Ge_3O_{12}$ material was chosen since it has the highest photon detection efficiency of any commercial scintillator [Kno89]. The BGO detector is shaped so that a large fraction of its volume is in the direction of forward scattering, the peak of the Compton scattering distribution [Kra88]. The 55° taper on the front edge of the BGO allows an angular range from 55° to 125°.

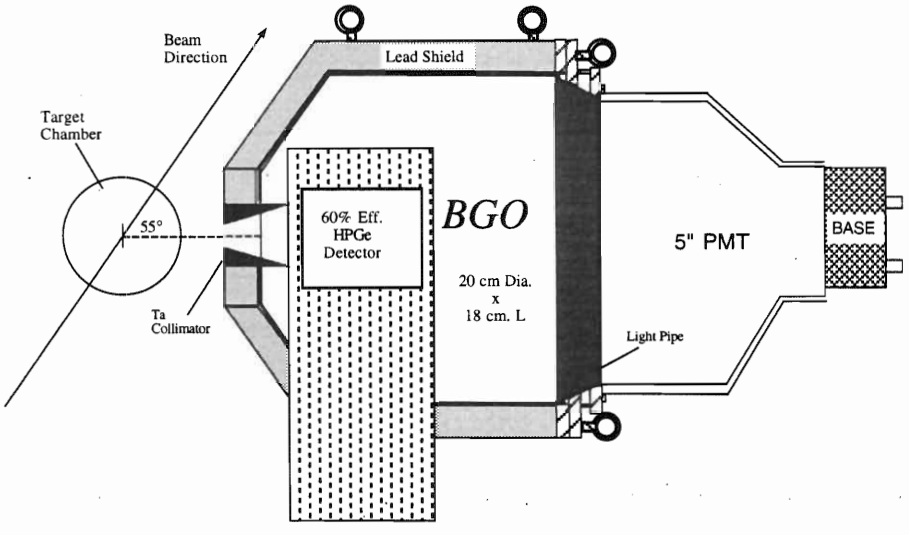

Figure 3.6. Top cross-sectional view of the suppressed HPGe within the BGO detector.

3.4 Data Acquisition

The implementation of the CSS system at TUNL-HRL required the addition of new hardware and software to the existing data acquisition system. This new system was designed to produce high-resolution gamma-ray decay data and also retain all of the capabilities of the older version described by Bull [Bul89]. The new system is therefore capable of generating an excitation function to locate a resonance, and then to collect gamma-ray

decay data at the resonance energy. The portion of the new system retained from the older version is described in Sect. 3.4.1. The discussion of the data acquisition used to acquire gamma-ray decay data in Sect. 3.4.2 completes the description of the new system.

3.4.1 Excitation Function Data Acquisition

The data used to generate an excitation function were produced by a SSB detector and two NaI(Tl) detectors. A block diagram of the data acquisition electronics configuration is given in Fig. 3.7. The output signals from each detector are sent to a preamplifier and then to a linear amplifier where they are further shaped and integrated. The amplifier produces a unipolar and a bipolar signal for each detector event. The energy of the proton or photon is carried in the unipolar pulse, which is delayed by 900 ns and sent to an eight input multiplexer module.

The bipolar signal is used to reject any signals from protons elastically scattered from the ^{12}C target foils (see Sect. 3.5). These signals cause pileup and an increased dead time of the system. The bipolar signal is routed to the gated SCA (Single Channel Analyzer) and also to the TSCA (Timing Single Channel Analyzer). For the SSB output, a window is set in the TSCA to a width that encloses the ^{12}C signals. However, for the output from the NaI detectors, the TSCA windows are set to zero width. The TSCA only outputs signals that fall within its window, which are then sent to the inhibit input of the gated SCA. This results in the SCA only outputting non-carbon scattering events, which are then sent as gate signals to the multiplexer.

The multiplexer routes the unipolar signals from all three detectors to a single Northern ADC, operated in coincidence mode. The multiplexer also outputs routing signals, which indicate the particular detector associated with each of the unipolar output pulses. These routing signals are converted by the buffer interface module to a gate pulse necessary for the ADC to digitize the unipolar multiplexer output. The ADC output and its associated routing signal are then stored in one of two 256 word blocks within a CAMAC buffer module. The buffer signals the Microprogrammable Branch Driver (MBD) to transfer the data to the VAX when one of these blocks becomes full. At the same time, the other section

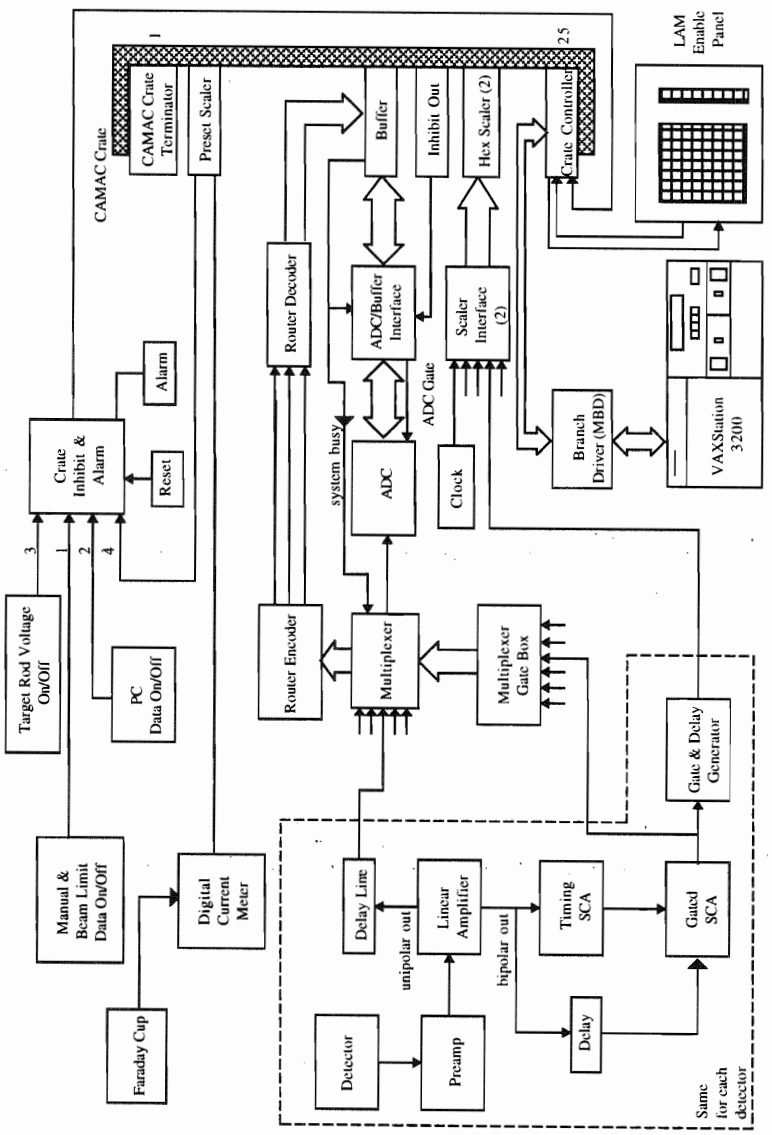

Figure 3.7. Electronics configuration used for the acquisition of excitation function data.

of the buffer's memory is being filled, which allows for continuous data processing. The XSYS data acquisition software package [Sod87] then directs the sorting of these data into the appropriate sections of VAX memory (called data areas). The SSB and NaI data are then displayed in 512 channel spectra using an XSYS graphics program.

Hardware scalers are used for monitoring of dead times and control of the intervals during which data are accumulated. The output of the gated SCA is also routed to a gate and delay generator (G&D) module. This module produces TTL logic pulses that are counted by a CAMAC scaler. A comparison of these detector counts and the counts sorted into a given Vax spectrum allows computation of the dead time for each detector. A second counter, the CAMAC preset scaler, ensures that each data point in the excitation function represents a collection of the same amount of beam current on the Faraday cup at the end of the gamma-ray chamber. A Digital Current Integrator (DCI) outputs pulses that decrement the scaler from a preset value until zero is reached. Data acquisition is then inhibited, various experimental parameters updated, data for that run dumped to disk, and data acquisition is begun once again.

3.4.2 Gamma-ray Decay Data Acquisition

The configuration used to acquire gamma-ray decay data using the CSS system is shown in Fig. 3.8. The data acquisition configuration used for the SSB and NaI detector signals is identical to that described in Sect. 3.4.1. The data acquisition system for the two HPGe detectors is more complicated, since it requires information about both the energy and the timing of the photon interactions within the detector. This information is collected in the form of a charge pulse that is input into a preamplifier located inside each detector. The preamplifier then produces both an energy and a timing output signal.

The energy signal is sent to a spectroscopy amplifier for each detector, which integrates and shapes this pulse. Both spectroscopy amplifiers are equipped with pulse pileup rejection (PUR) and ballistic deficit correction (BDC) circuitry. Pileup occurs when nearly simultaneous events occur inside the detector and are shaped into a single charge pulse. The amplitude of the amplifier input signal is then not representative of the true photon

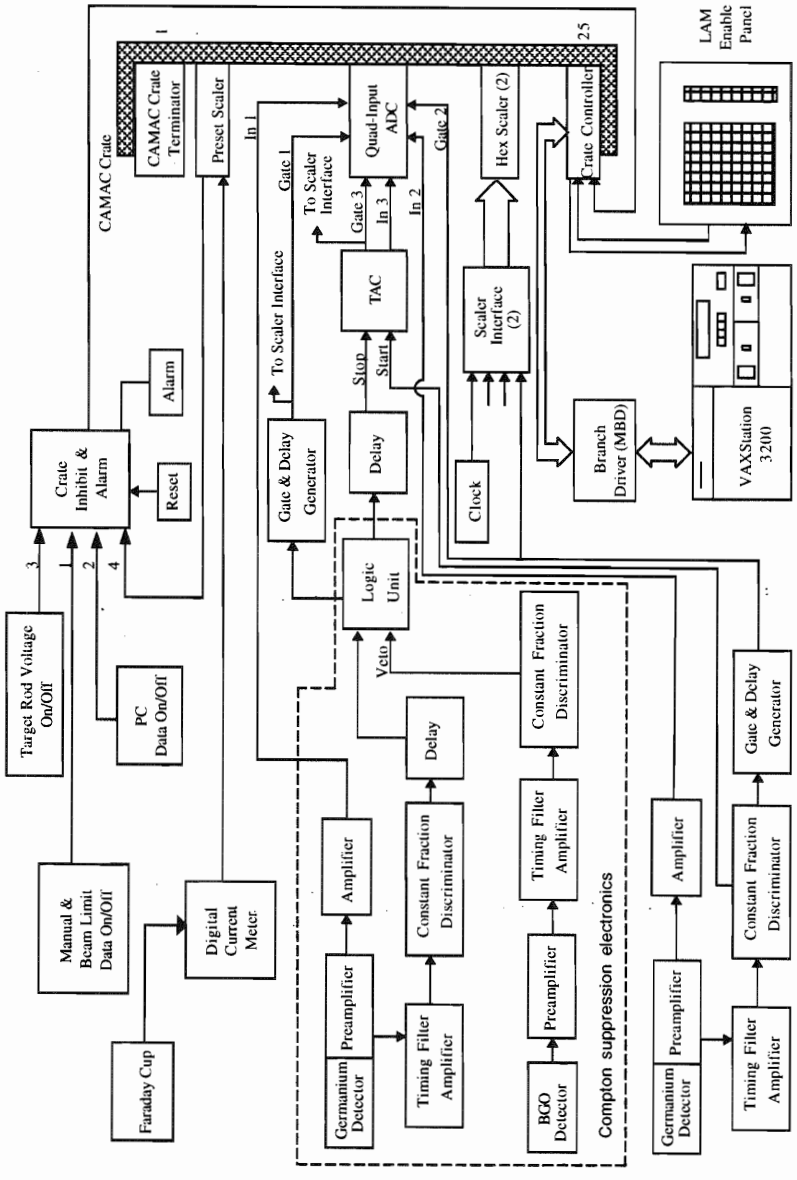

Figure 3.8. Electronics configuration used for the acquisition of gamma-ray decay data.

energy of any of these events. Ballistic deficit occurs when an incomplete charge collection occurs within the shaping time of the amplifier. The resulting depressed amplitudes of these signals degrade the overall energy resolution of the detector. The amplifiers for both detectors were always operated in PUR and BDC modes during experiments.

The timing signals from the BGO and suppressed HPGe (CSGe) detector are used to reject signals arising from Compton scattering and pair production events inside the detector. The timing outputs from both detectors are each sent to a Timing Filter Amplifier (TFA), which amplifies and shapes the signal. The TFA output is then sent to a Constant Fraction Discriminator (CFD) module to determine the exact time the photon interacted with the detector crystal. This is accomplished by the CFD producing a pulse a certain time after the leading edge of the input pulse has attained a constant fraction of its amplitude. The 500 ns wide output of the CFD for the BGO detector is sent to the veto input of a Logic Unit. The 50 ns wide CFD output for the CSGe detector is delayed by 127 ns to ensure that this signal arrives at the Logic Unit after the BGO veto signal. If the Logic Unit receives CFD signals from both detectors in coincidence (ie. within 500 ns), then the full energy of the photon was not deposited in the detector, and this CSGe signal is rejected.

All non-coincident timing signals arising from "good" events within the CSGe are sent to a G&D module, which produces the necessary gate signal required for digitization by a CAMAC quad ADC. The other, unsuppressed HPGe (USGe) detector timing signals are sent through a parallel path in the data acquisition system, except their CFD outputs are sent directly to the gate and delay generator. The outputs from the G&D module are also routed to a CAMAC scaler, which is used to compute dead times as discussed in Sect. 3.4.1. The ADC digitizes its input signals and directly transfers the data to the MBD and then to appropriate XSYS data area within the VAX memory, which are then displayed as 8192 channel spectra.

A great strength of this system is its capability to acquire several different types of data with a single detector geometric configuration. For example, the recording of γ-γ coincidences between the two HPGe detectors is possible using the Time-to-Amplitude

Converter (TAC) module. The time interval between two "good" events that constitute a coincidence is set by start and stop signals input into the TAC. The output of the G&D module for the USGe detector defines the start of this interval. If the 31.5 ns delayed output of the Logic Unit for the CSGe detector (the stop signal) is received by the TAC within 500 ns, a coincident event has occurred. The TAC output is then sent to a third channel of the ADC, where it is digitized and stored in a third data area within the Vax memory.

3.5 Targets

The experiments described in this thesis used thin film ^{27}Al and ^{29}Si targets. The aluminum targets were used to perform energy and efficiency calibrations of the HPGe detectors using the ^{27}Al(p,γ) reaction. A detailed procedure for the fabrication of these targets is given by Drake [Dra94]. The methods used in producing the silicon targets are discussed in detail by Wallace [Wal96].

The fabrication process for ^{27}Al consisted of using a high current evaporator to evaporate monoisotopic aluminum onto ~ 5.0 μg/cm^2 carbon foils. The isotope was held in a 0.005 in. thick open tantalum boat and evaporated until thicknesses of ~ 20 μg/cm^2 were achieved. A Maxtek Thickness Monitor determined the total amount of material deposited on the foils. The thickness of ^{27}Al and the identification of contaminants were obtained from a charged particle spectrum (as shown in Fig. 3.9). The very large carbon peak has been partially gated out of the spectrum electronically, as described in Sect. 3.4.1.

The fabrication of ^{29}Si thin film targets also used the vapor deposition method. SiO_2 enriched to 95.7 % in ^{29}Si was reduced using Ta powder in the ratio of 8 parts ^{181}Ta to 1 part ^{29}Si. Both thin targets, (thickness ~ 1.5 μg/cm^2) and thicker targets (~ 3.0 μg/cm^2) were used for the experiments. Silicon target thicknesses and identification of contaminants were again determined from a charged particle spectrum (as shown in Fig. 3.10). A choice of which thickness target to use was made based on the width of the resonance being studied and the proximity of other resonances in the surrounding energy region.

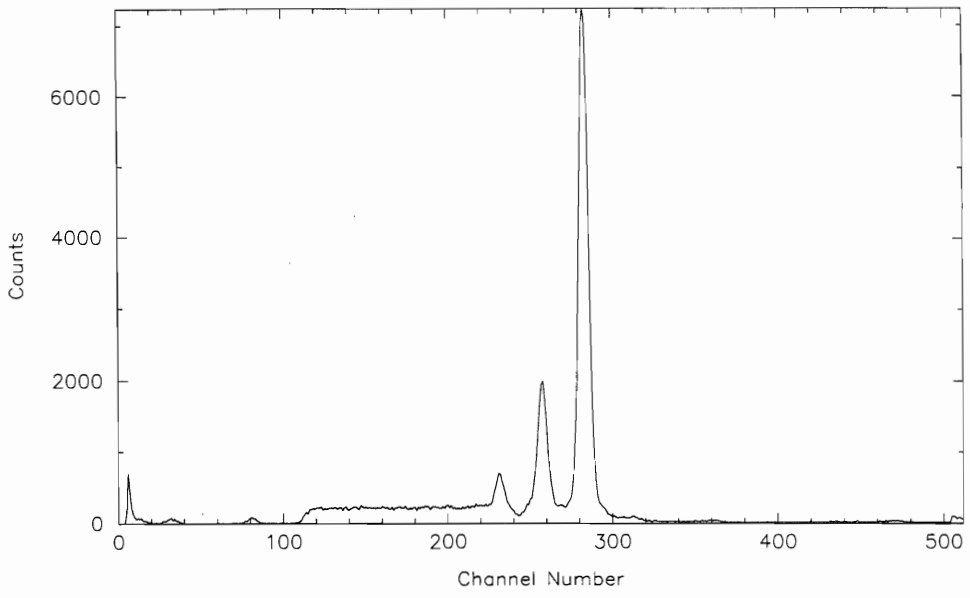

Figure 3.9. p + ^{27}Al particle spectrum at $E_p = 0.990$ MeV.

3.6 Procedures

3.6.1 Excitation Function Data

The purpose of the excitation function experiments was to perform a detailed search for any possible new ^{29}Si(p,γ) resonances in the proton energy interval of 1.0 to 2.0 MeV. The yield curve generated by these measurements added to resonance data taken by Frankle et al. [Fra92] from $E_p = 2.0$ to 3.0 MeV. In addition, yield curves for the (p,p) and (p,p$_1\gamma$) reactions were also generated. Data were taken in steps of 400 eV with an integrated charge of 400 μC per data point. Energy steps of 100 to 200 eV were taken over narrow resonances and in their immediate vicinity.

The spectra from the three detectors and their associated yield curves were displayed online during data acquisition. The data acquisition program calculated the net counts (after background subtraction) within the ^{29}Si(p,p) gate (as shown in Fig. 3.10) in order to generate an online (p,p) yield curve. An energy calibration and kinematics program was used to automatically shift this gate with the elastic peak as the proton energy was incremented. A typical spectrum for a NaI(Tl) detector is shown in Fig. 3.11. The sum of

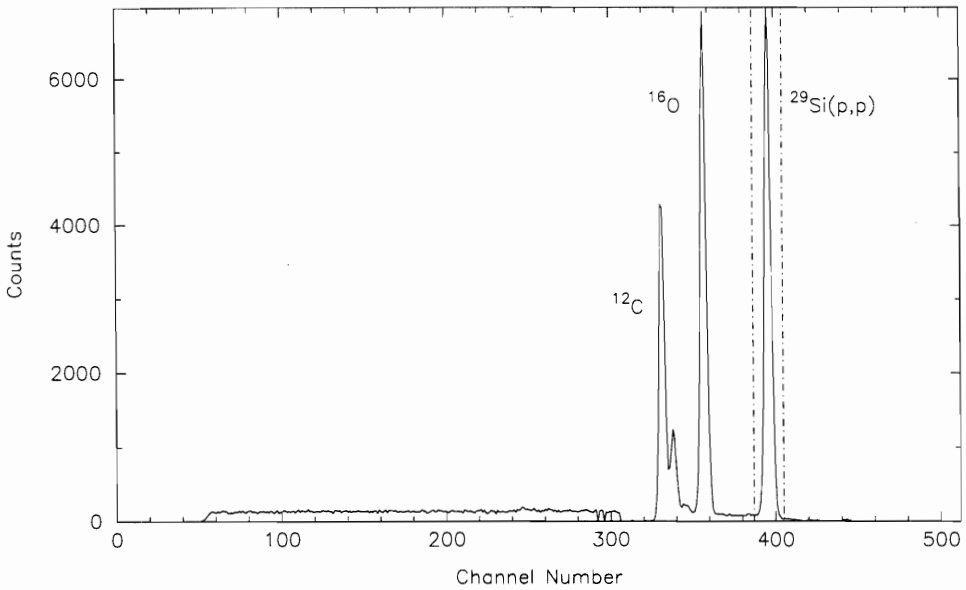

Figure 3.10. p + ^{29}Si particle spectrum at $E_p = 1.9689$ MeV. The dashed lines indicate the gate set about the ^{29}Si peak.

the counts within the gate set about the 1.273 MeV γ-ray peak were used to generate the (p,p$_1\gamma$) yield curve for each detector. The yield curve for the capture reaction was generated by summing the counts within the gate set from $E_p = 2.6 - 9.0$ MeV. No background subtraction was used in generating the γ-ray yield curves. An energy calibration of the γ-ray spectra was performed using both ^{22}Na and ^{60}Co radioactive sources.

As discussed in Sect. 3.5, two target thicknesses were used during these experiments. Normally, targets were used until they had severely degraded or were broken. Possible problems with targets were determined by observation of any abrupt changes in the (p,p) yield curve, monitoring of the SSB amplifier signal, or as a last resort, visual inspection. The yield curve was repeated for an energy range of several keV after a target or its position relative to the beam was changed to allow normalization of the yield in the later data analysis. The retuning of beam through the ESA or to the target also often required repeating a portion of the yield curve. This overlap was especially crucial when these circumstances occurred near to or at the resonance energy.

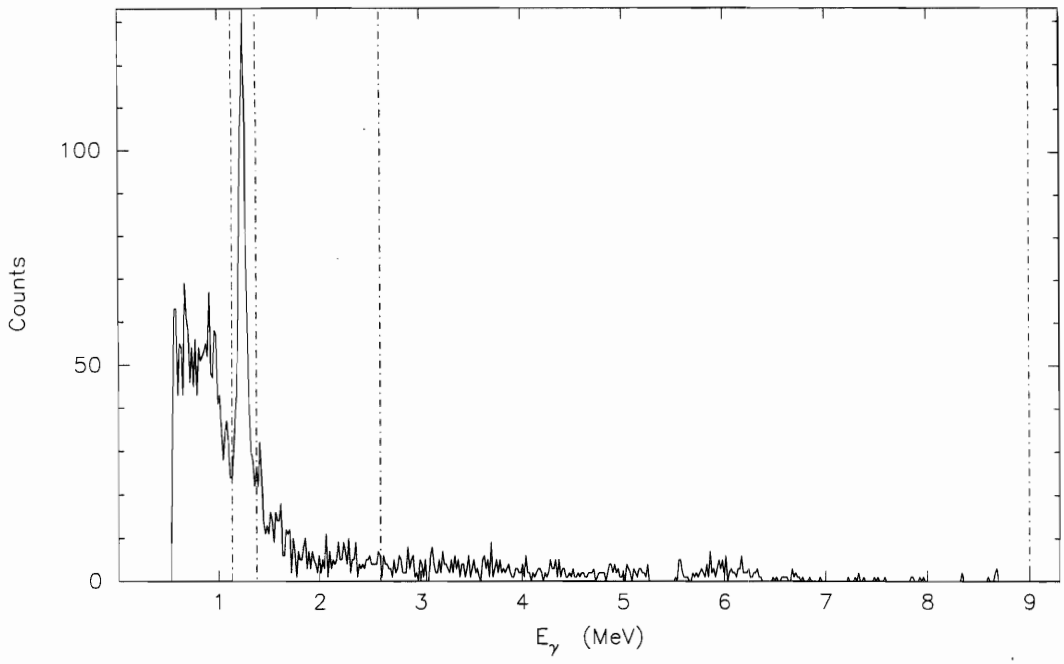

Figure 3.11. p + ^{29}Si NaI spectrum at $E_p = 1.9689$ MeV. Dashed lines indicate gates set about the 1.273 MeV peak and the 2.6 – 9.0 MeV region.

3.6.2 Gamma-ray Decay Data

The procedure for acquiring the gamma-ray decay data for a given resonance consisted of three main steps: calibrating the HPGe detectors, generating a yield curve in the surrounding energy region, and then collecting gamma-ray decay data for that resonance. Extensive calibration data were accumulated to enable accurate determination of the energy and relative strengths of the gamma-rays in the later data analysis. These data were accumulated using gamma-rays from a 10 μCi ^{152}Eu source and from the extensively studied 991.86 keV resonance [End90b] in the ^{27}Al(p,γ) reaction. The ^{152}Eu source produces well known gamma-rays from 121 to 1408 keV and the capture reaction produces ^{28}Si gamma-rays from 1522 keV to 10,762 keV. A short yield curve was measured in the vicinity of a resonance to determine its energy, or "on-resonance" location, as well as to select an appropriate energy at which to acquire data at an "off-resonance" location. Gamma-ray spectra were accumulated from room background radiation as well as on and off resonance to enable the identification of those gamma-rays originating from the ^{30}P resonance itself.

A ^{60}Co source was used to match the gains of the two HPGe amplifiers at a level that allowed $\sim$90 keV to 8000 keV γ-rays within the 8192 channel spectra. Energy calibration data were accumulated at the resonance energy with both detectors at 90° to eliminate Doppler shifts of the energies of the gamma-rays. Sufficient statistics were usually obtained after data was accumulated for 25,000 μC on target. An approximate, third-order energy calibration was performed online using the ^{28}Si gamma-ray peaks. This calibration was used throughout the experiment to aid in identifying important gamma-rays in the spectra.

The efficiency calibration was required because the efficiency of the HPGe detectors in detecting gamma-rays is dependent on γ-ray energy. The same geometric configuration used for the ^{30}P data (the USGe detector at 90°, CSGe detector at 55° and a target rod angle of 30°) was chosen to ensure an accurate calibration. For the Eu data, the source was attached to a target ring on the target rod holder to mimic the configuration used for the Al and Si targets. Energy and efficiency data were simultaneously accumulated using the Eu source for typically 2.5 hours. Usually sufficient statistics were achieved for the ^{27}Al(p,γ) data after 100,000 μC was collected on the Faraday cup.

Typical spectra produced using the CSGe detector and USGe detectors are shown in Fig. 3.12 and Fig. 3.13. Note the much lower background present in the CSGe spectrum as a result of the suppression of the Compton scattering events. This suppression was frequently monitored during an experiment. A data run consisted of acquiring data at either an on- or off-resonance energy (for 40,000 μC usually) and then storing the data on disk. Spectra were typically accumulated for a minimum of 200,000 μC on and off resonance, with more data collected for weak resonances. The resonance energy was remeasured prior to the start of each on-resonance run in order to adjust for any experimental shifts in the resonance energy. Data for a given run were accepted only if the beam energy was stable throughout the entire run.

The experiments performed to identify the "contaminant" resonances employed the same setup and procedure as described above for the ^{30}P gamma-ray decay experiments. For well isolated resonances, the spectra were monitored for the presence of the characteristic ^{30}P gamma-rays while accumulating data on-resonance. For those resonances very

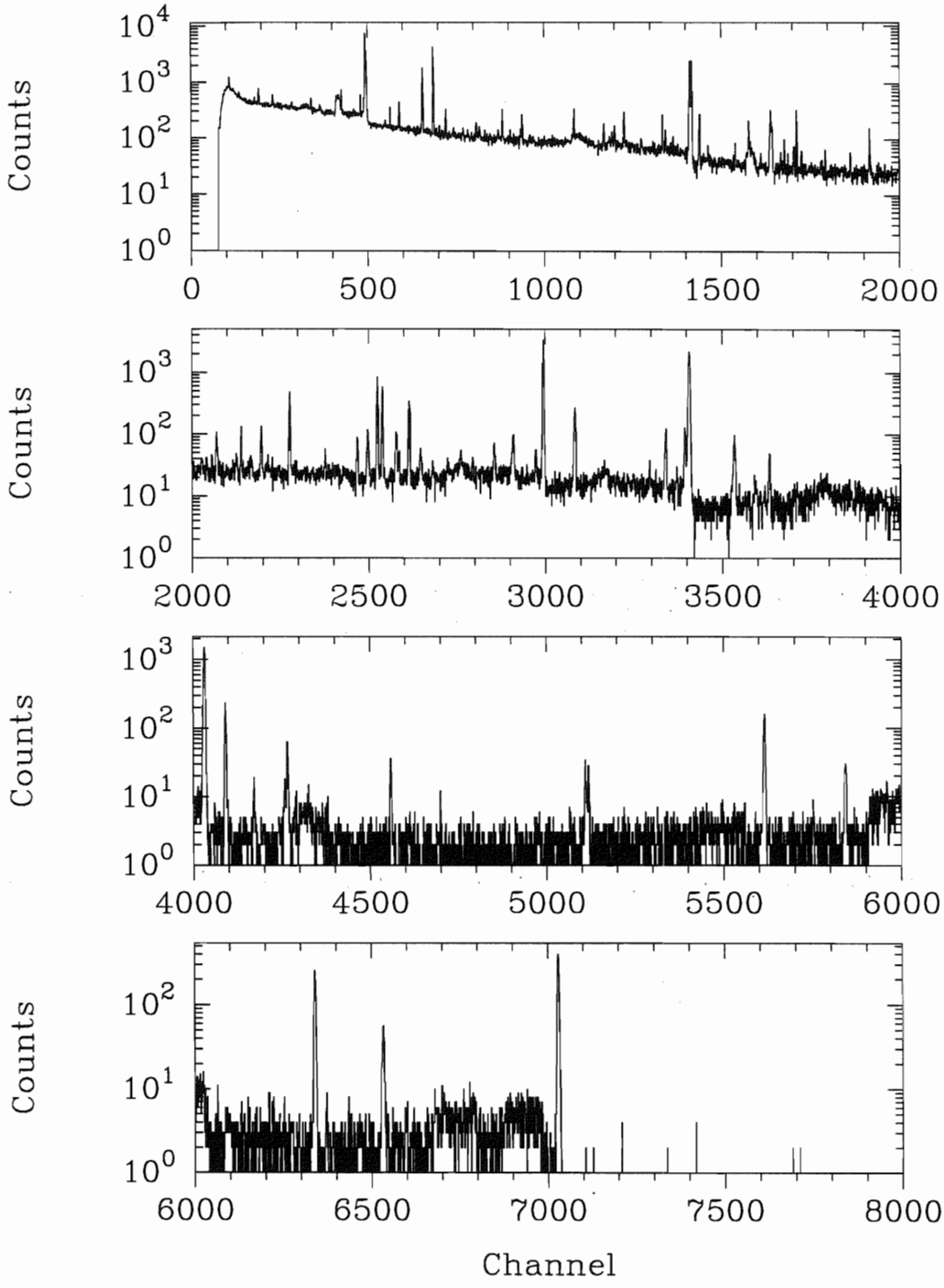

Figure 3.12. CSGe spectrum for the $E_p = 1.6844$ MeV resonance.

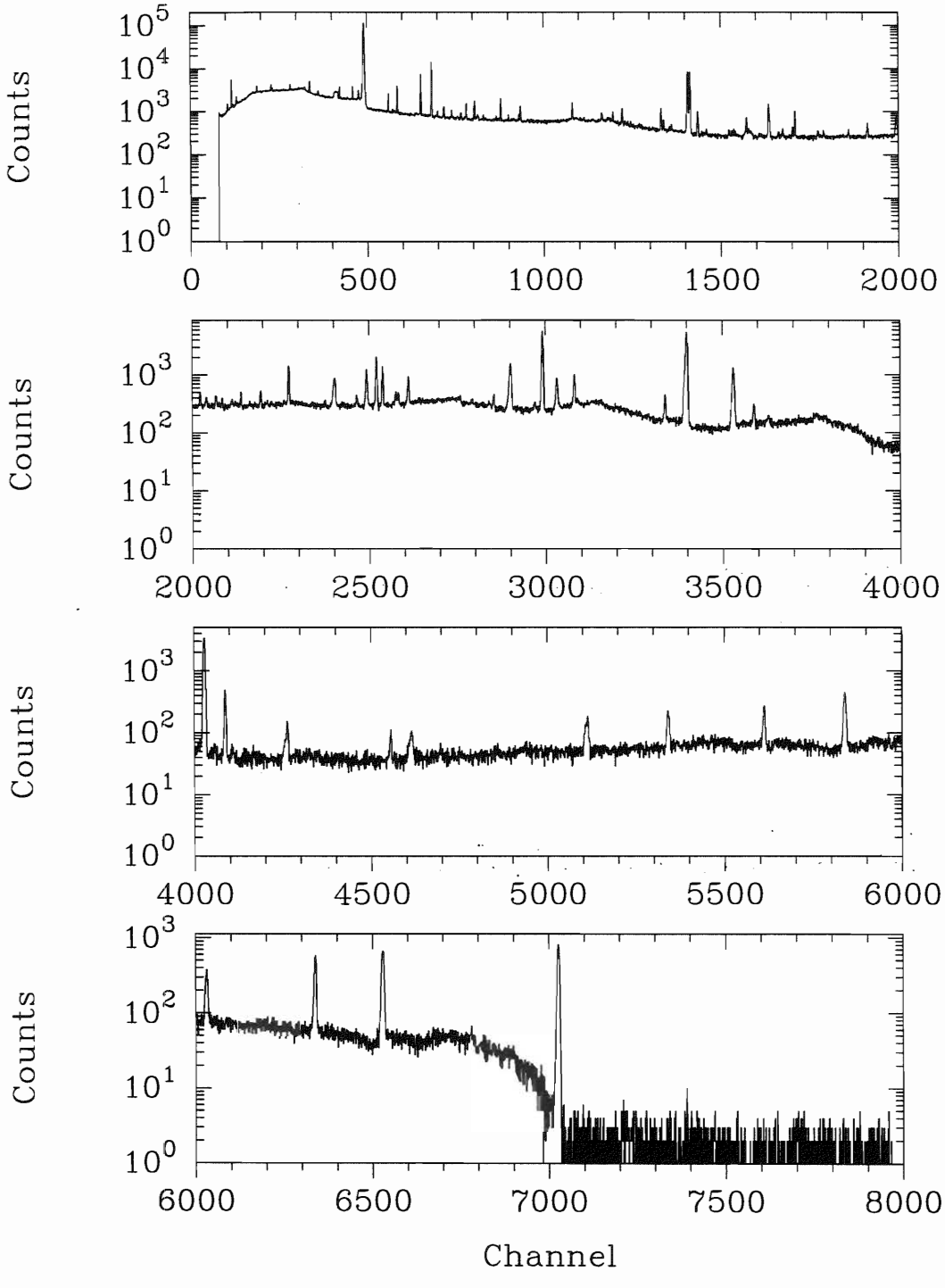

Figure 3.13. USGe spectrum for the $E_p = 1.6844$ MeV resonance.

near to or overlapping with ^{30}P resonances, data were accumulated at on- and off-resonance energies until the gamma-rays from either resonance could be differentiated from one another. If a resonance was determined to have no characteristic ^{30}P resonant gamma-rays, it was not assigned to ^{30}P.

Chapter 4

Excitation Function Analysis and Results

As discussed in Chap. 3, ^{29}Si(p,γ)^{30}P, ^{29}Si(p,p$_1\gamma$)^{29}Si, and ^{29}Si(p,p)^{29}Si excitation function data were measured for $E_p = 1.0 - 2.0$ MeV in a search for new ^{30}P resonances. This study overlapped the elastic scattering measurements of Nelson [Nel83b] and Frankle [Fra91] as well as the capture measurements of Reinecke et al. [Rei85]. A total of 37 (p,γ) resonances were located; eighteen of which were previously known. New resonances at 1.0380, 1.4333, and 1.5787 MeV were identified as originating from the ^{29}Si(p,γ) reaction. The additional 16 (p,γ) resonances were determined by analyses of their gamma-ray spectra (see Chap. 5) to originate from various contaminants in the targets. A functional form was fit to the gamma-ray yields in order to calculate the areas under all of the peaks. No additional analysis was performed for the elastic yield. The areas of the ^{29}Si(p,γ) excitation functions were converted into absolute resonance strengths using the results of Reinecke et al. [Rei85].

4.1 Preparation of Yield Curves

Yield curves were generated in a manner similar to that used online during the experiment as described in Sect. 3.6.1. The one exception was that the data acquisition system

that produced the online yield curve was replaced in the subsequent offline analysis by a program XSTRIPFD, which initially read the spectra stored on disk into three separate XSYS data areas. The program XSTRIPFD then summed the counts within the appropriate gates (see Fig. 3.10 and 3.11) in the spectra. A linear background was subtracted for the elastic spectrum. The areas under the peaks were corrected for dead time and the results stored in the appropriate VAX data area. The program then read the set of spectra for the next energy into memory and repeated the process. All excitation functions were normalized by simple multiplicative factors that matched the levels of adjacent background regions to each other.

4.2 Fitting Procedure

The resonances in the gamma-ray yields were fit with combinations of Gaussian and Lorentzian functions [Fra91]. A particular resonance was divided at its peak into a low energy and high energy section, each of which was fit to a particular function. The resulting fit consisted of either a low energy Gaussian and a high energy Lorentzian (GL) or both a high and low energy Lorentzian (LL). A Gaussian function centered at E_{res} of full width at half-maximum (FWHM) $\Gamma_G = 2.354\sigma$ and amplitude A is given by

$$P_G = A \exp\left[-\frac{1}{2}\left(\frac{E_p - E_{res}}{\sigma}\right)^2\right]. \tag{4.1}$$

A Lorentzian function with a FWHM of Γ_L and the same amplitude A is given by

$$P_L = \frac{b\,A}{\pi}\frac{(\Gamma_L/2)}{(E_p - E_{res})^2 + (\Gamma_L/2)^2}, \tag{4.2}$$

with $b = \pi\Gamma_L/2$ as a normalization constant.

Due to the effects of finite energy resolution and target thickness on the "true" shape of a resonance, both functions are needed to describe the shapes of these resonances. The $\sim$220-eV resolution of the experimental system forms a lower limit on the widths, Γ_{exp}, observed in the laboratory. For resonances with natural total widths less than Γ_{exp}, the low energy side of the resonance is governed by the energy spread of the incident protons, which is well described by a Gaussian. In addition, the finite thickness of the target causes

straggling to occur, which produces a Lorentzian shape on the high energy side of the resonance. When the natural width is comparable to or larger than the energy loss in the target, a low energy Lorentzian describes the shape well [Fow48]. For example, at 1.5 MeV, the energy loss [Mar68] through the 1.5 μg/cm^2 ^{29}Si targets was $\sim$350 eV, and $\sim$700 eV for the 3.0 μg/cm^2 targets. Therefore, for resonances with small natural widths, the thinner 1.5 μg/cm^2 targets produced a GL resonance shape and the thicker targets produced an LL shape. For the $\sim$20 % of resonances with natural widths larger than Γ_{exp}, an LL shape was always used. Fig. 4.1 shows an example of a GL fit and Fig. 4.2 shows an example of a LL fit. A linear least squares fit to the background was used in all of the fits.

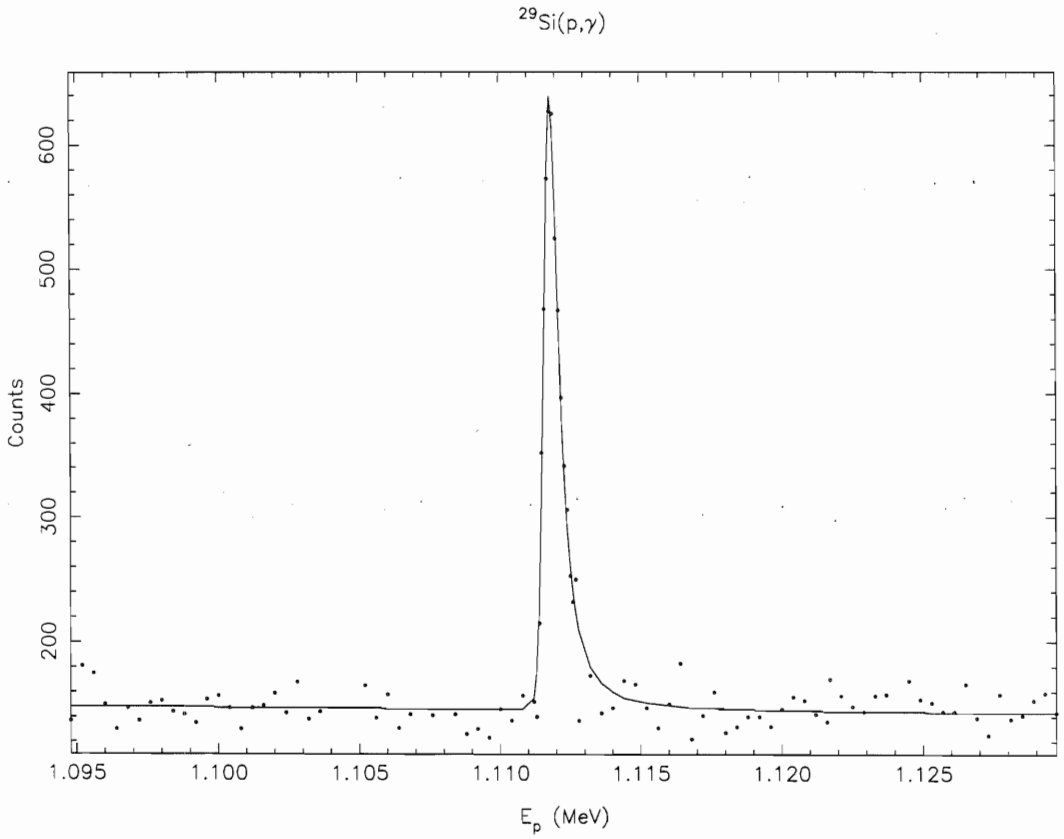

Figure 4.1. Gaussian-Lorentzian fit for the 1.111 MeV resonance.

Initially, the resonances were fit by manually adjusting several parameters of the fitting functions and inspecting the resulting fit to the data. The resonance energy, the FWHM of

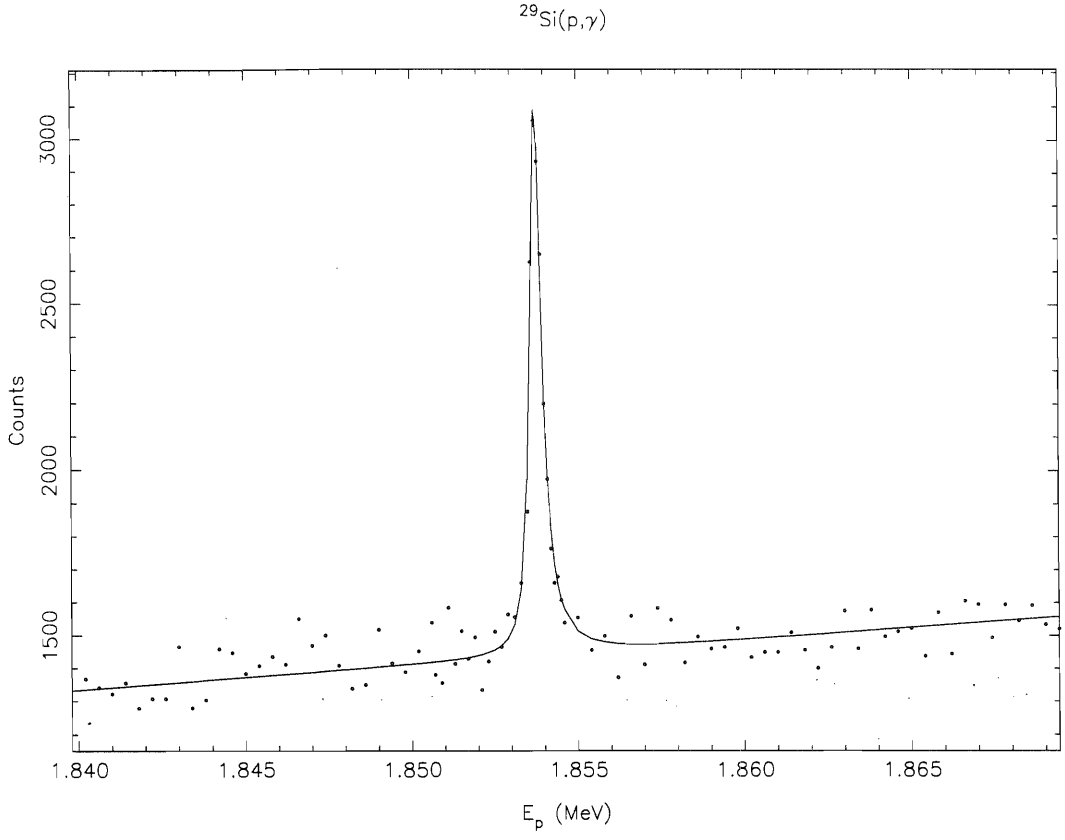

Figure 4.2. Lorentzian-Lorentzian fit for the 1.853 MeV resonance.

each function, the amplitude, and the slope and intercept of the line fit to the background were the six adjustable parameters that determined the fit to a given resonance. Once a reasonable fit was obtained, the data and parameter files were input into a control program. Within this program, the set of i fitting parameters were input as an array $X(i)$ to a subroutine NL2SNO, obtained from Argonne National Laboratory. A separate subroutine CALCR calculated the residual, $R(j)$, which is the difference between the data and fit for n data points. NL2SNO then varied $X(i)$ until the sum of the squares of $R(j)$ was minimized. The resulting final set of parameters was then used to calculate the best fit to the data for each of the n data points.

Several resonances could be fit simultaneously using these fitting codes, with the ability to hold certain resonance parameters fixed and to vary others. This was very useful in the

$E_p = 1.6 - 1.7$ MeV region, where three wide (p,γ) resonances overlap three narrow (p,γ) resonances. Here, the 15-keV broad 1.6393 MeV resonance, the 4.5-keV wide 1.6844 MeV resonance, and a 62 ($\pm$4)-keV wide 1.689 MeV ^{12}C(p,γ) resonance [Ajz91] overlap the narrow 1.6639, 1.6675, and 1.6685 MeV resonances. The best fit to the yield was obtained by first fitting the broad resonances; this fit resulted in $\Gamma_{exp} = 58$ keV for the contaminant ^{12}C resonance. The parameters for this fit were then held fixed as the fitting parameters for the narrow resonances were varied to obtain the best overall fit for this region. Fig. 4.3 – 4.6 illustrate the data and fits for the three reactions studied in these experiments.

4.3 Area Calculations and Uncertainties

In addition to producing the fits to the data, the fitting parameters also were used to calculate the area under each peak in the yield curve. The widths of both functions obtained from a particular fit and the amplitude were used to analytically calculate the area. Table 4.1 provides a summary of the fitting parameters and the gamma-ray yield for each resonance. The experimental width Γ_{exp} was calculated as the average of the FWHM of the two functions that defined the fit. All 21 of the ^{30}P resonances listed in this table were observed in both the (p,γ) and (p,p$_1\gamma$) reactions. However, three contaminant resonances were observed only in the (p,p$_1\gamma$) reaction and seven other contaminant resonances were present only in the (p,γ) reaction.

The major source of uncertainty in these area calculations arose from the quality of the data itself. The method used to estimate these area uncertainties followed the procedure adopted by Frankle [Fra91]. Since both the amplitude and experimental width are interrelated, a quantity Y was defined as the ratio of the amplitude to Γ_{exp}. The uncertainty of the area under each peak was estimated based on its Y value. Table 4.2 lists the value of the experimental width, Γ_{exp}, and the area and its error for each ^{30}P resonance.

The particular values of Y for which a 10, 35, or 100 % error on the area were assigned are shown in Table 4.3. Strong, isolated peaks were assigned the smallest errors, since these errors were mainly due to the variation in target thicknesses from an average value. A 35 % error was estimated for strongly overlapping resonances and for those resonances

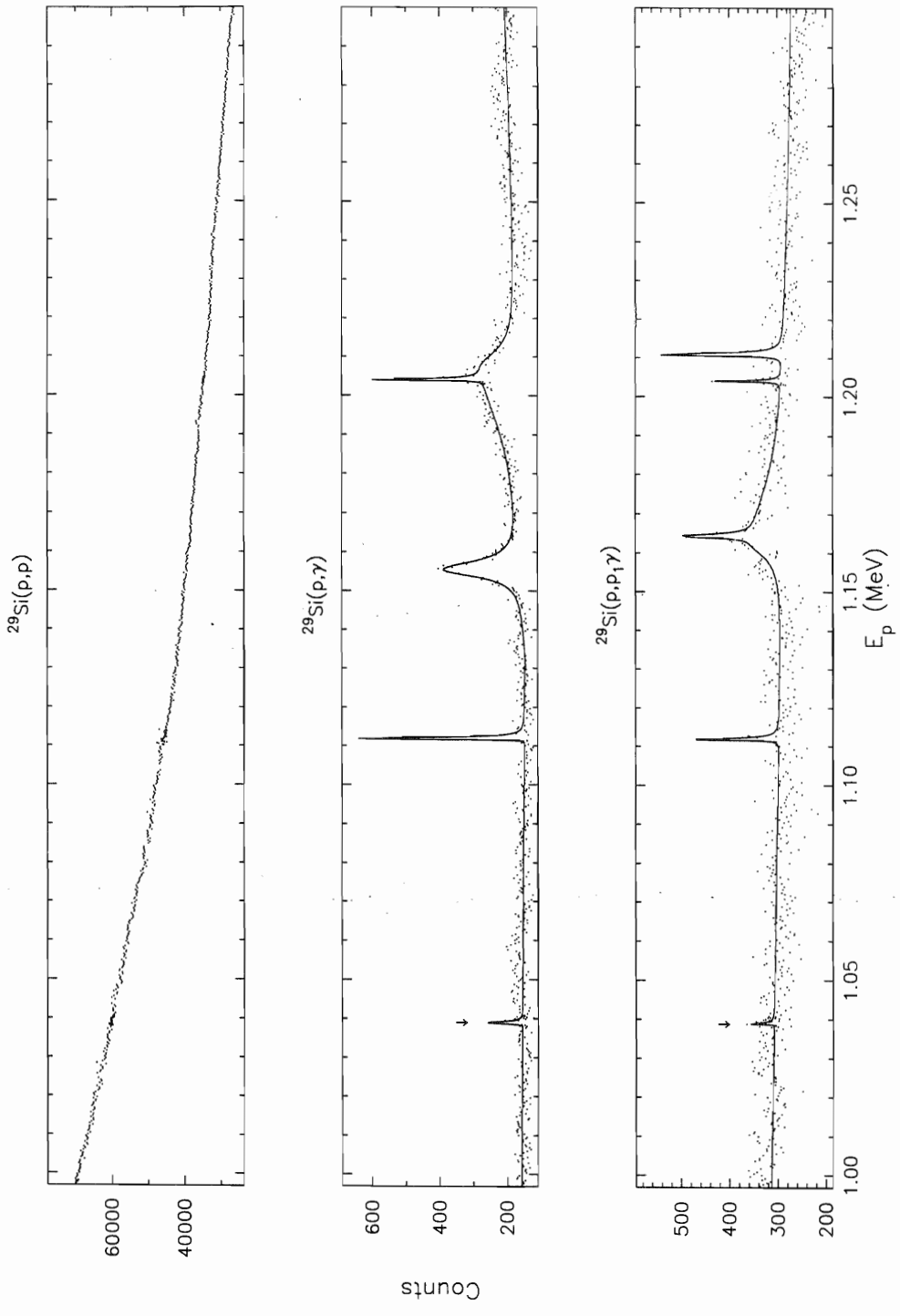

Figure 4.3. Data and fits for laboratory energies $E_p = 0.997 - 1.30$ MeV. The 1.038-MeV resonance is indicated by an arrow.

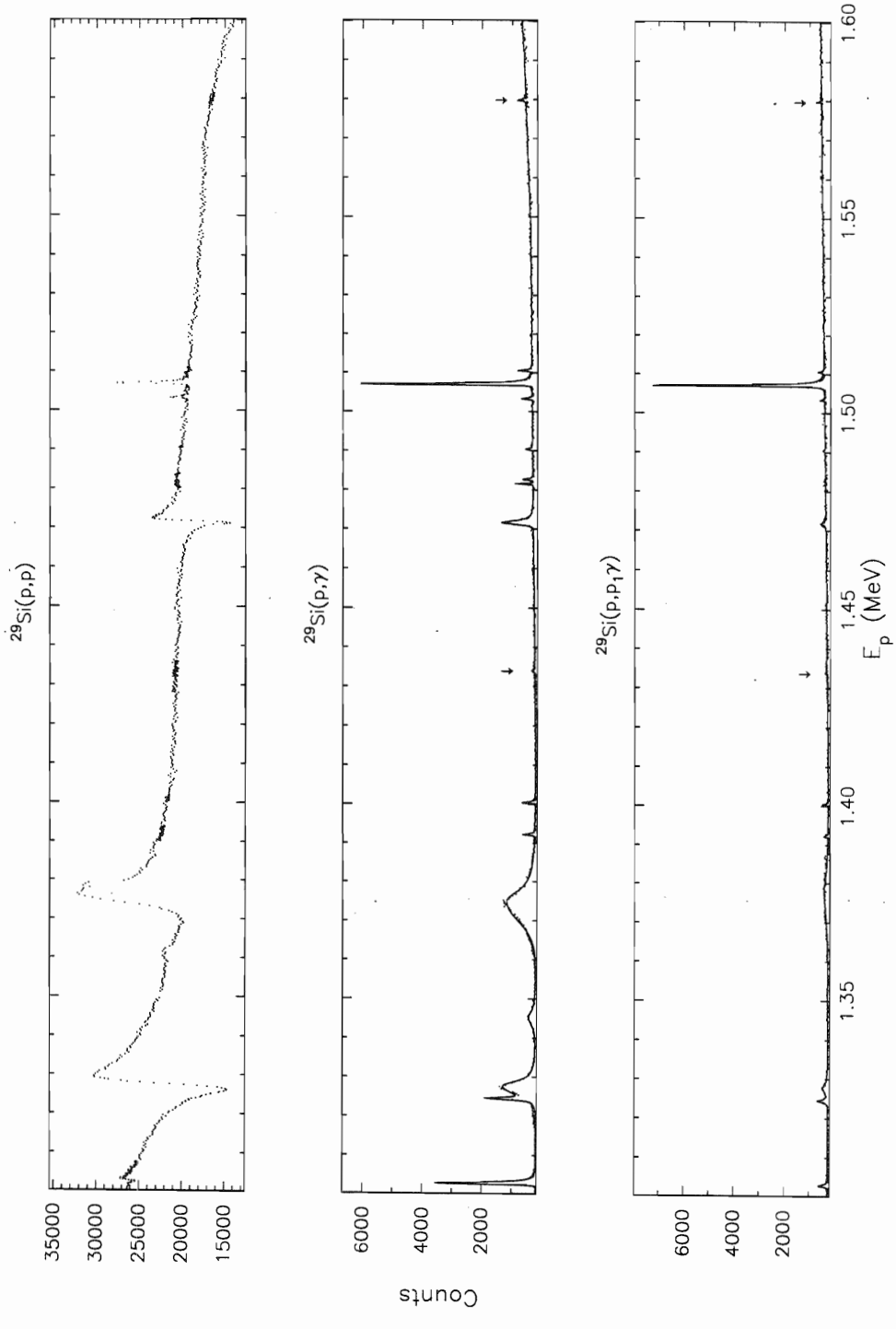

Figure 4.4. Data and fits for laboratory energies $E_p = 1.30 - 1.60$ MeV. The 1.4333- and 1.5787-MeV resonances are indicated by arrows.

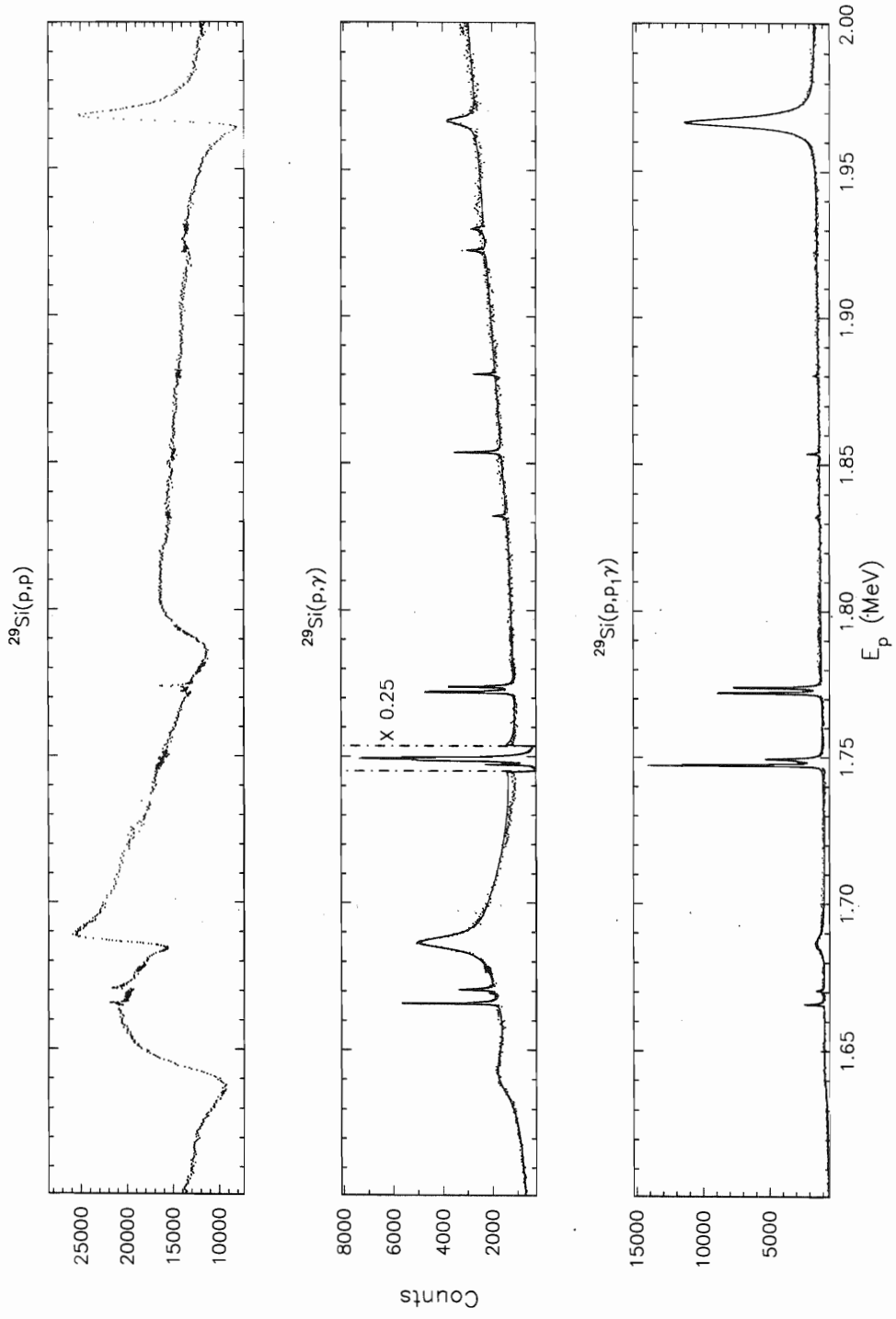

Figure 4.5. Data and fits for laboratory energies $E_p = 1.60 - 2.00$ MeV. The region between the dashed lines in ^{29}Si(p,γ) has been multiplied by 0.25.

Table 4.1. Fitting parameters for the $^{29}Si(p,\gamma)^{30}P$ and $^{29}Si(p,p_1\gamma)^{29}Si$ reactions.

	$^{29}Si(p,\gamma)^{30}P$			$^{29}Si(p,p_1\gamma)^{29}Si$		
E_p	Γ_{exp}	Amplitude	Area	Γ_{exp}	Amplitude	Area
(MeV)	(eV)	(cts)	(MeV cts)	(eV)	(cts)	(MeV cts)
1.0380†	700	100	0.09	530	45	0.04
1.1110†	630	490	0.42	760	170	0.18
1.1544	4800	230	1.7			
1.1621				240	62	2.6
1.1636				220	160	0.30
1.2021	550	330	0.29	420	140	0.09
1.2031	27000	120	4.9			
1.2097				750	270	0.31
1.3020†	630	3400	2.9	650	360	0.31
1.3238†	640	1300	1.0	680	420	0.44
1.3268†	4000	1100	5.4	2800	200	0.93
1.3463	4300	220	1.2			
1.3737†	9300	970	11	12000	150	2.7
1.3915	450	390	0.23	390	160	0.10
1.3997	400	460	0.26	260	240	0.10
1.4333†	840	73	0.09	3100	51	0.25
1.4709†	1200	1000	1.7	1200	190	0.30
1.4806	200	580	0.14			
1.4820	430	340	0.19			
1.4897	230	250	0.09	550	86	0.06
1.5020†	370	340	0.17	130	180	0.04
1.5060†	470	5700	3.7	490	6900	4.6
1.5095	370	430	0.22	350	210	0.09
1.5787†	420	290	0.17	180	270	0.07
1.6393†	22000	770	26	50000	190	15
1.6639†	440	3980	2.8	500	1500	1.0
1.6675	300	170	0.08			
1.6685†	550	1500	1.3	500	470	0.30
1.6844†	5100	2800	22	5800	580	5.3
1.7450†	510	7800	5.4	460	13000	8.3
1.7464	1200	19800	31	950	1900	2.2
1.7472†	500	17000	11	520	3400	2.4
1.7698†	510	3700	3.0	460	8000	5.8
1.7715†	440	2600	1.8	430	6700	4.5
1.8340	500	470	0.32	320	280	0.14
1.8530†	420	1900	1.3	270	930	0.39
1.8794	420	890	0.58	340	350	0.19
1.9196	610	780	0.75	180	300	0.08
1.9269	1300	420	0.84			
1.9637†	2800	1200	5.2	3900	9800	61

†$^{29}Si(p,\gamma)$ resonances; bold-face type indicates the new resonances.

Table 4.2. Normalized areas for the $^{29}Si(p,\gamma)^{30}P$ and $^{29}Si(p,p_1\gamma)^{29}Si$ reactions.

	$^{29}Si(p,\gamma)^{30}P$			$^{29}Si(p,p_1\gamma)^{29}Si$		
E_p	Y [a]	Area	Error	Y [a]	Area	Error
(MeV)	(cts/eV)	(MeV cts)	(MeV cts)	(cts/eV)	(MeV cts)	(MeV cts)
1.0380	0.15	0.09	0.09	0.09	0.04	0.04
1.1111	0.78	0.42	0.15	0.23	0.18	0.18
1.3020	5.4	2.9	0.29	0.55	0.31	0.31
1.3238	2.1	1.0	0.36	0.61	0.44	0.44
1.3268	0.28	5.4	1.9	0.08	0.93	0.93
1.3737	0.10	11	11.	0.01	2.7	2.7
1.4333	0.09	0.09	0.09	0.02	0.25	0.25
1.4709	0.86	1.7	0.59	0.16	0.30	0.30
1.5020	0.93	0.17	0.06	1.4	0.04	0.02
1.5060	12	3.7	0.37	14	4.6	0.46
1.5787	0.69	0.17	0.06	1.5	0.07	0.03
1.6393	0.04	26	26.	0.01	15	15.
1.6639	9.0	2.8	0.28	2.9	1.0	0.36
1.6685	2.7	1.3	0.13	0.94	0.30	0.30
1.6844	0.54	22	7.8	0.10	5.3	5.3
1.7450	15	5.4	1.9	29	8.3	2.9
1.7472	34	11	3.9	6.6	2.4	0.85
1.7698	7.3	3.0	1.0	18	5.8	2.0
1.7715	5.9	1.8	0.62	16	4.5	1.6
1.8530	4.6	1.3	0.13	3.4	0.39	0.04
1.9637	0.41	5.2	1.8	2.5	61	21.

[a] $Y \equiv$ Amplitude/Γ_{exp}

with $Y < 1$. The smaller signal-to-noise ratio of resonances with $Y < 1$ enhances the effect of the target thickness uncertainty on their areas. The error for resonances with $Y > 1$ which overlapped with neighboring resonances was increased to a more conservative 35 % estimate. Finally, as shown in Table 4.3, the largest error of 100 % was assigned to resonances with the smallest values of Y, due to the extreme sensitivity of the parameters used in the area calculation to the uncertainty in the background. For these resonances, the best fitting parameters were useful only for providing qualitative information about a given resonance.

Table 4.3. Error regions for the ^{29}Si(p,γ)^{30}P and ^{29}Si(p,p$_1\gamma$)^{29}Si reactions.

σ_{area}	^{29}Si(p,γ)^{30}P Y [a] limits	^{29}Si(p,p$_1\gamma$)^{29}Si Y [a] limits
(.10)(Area)	$Y \geq 1.0$	$Y \geq 3.0$
(.35)(Area)	$0.25 \leq Y < 1.0$	$1.25 \leq Y < 3.0$
(1.0)(Area)	$Y < 0.25$	$Y < 1.25$

[a] $Y \equiv$ Amplitude/Γ_{exp}

4.4 Strength Calculations

The normalized areas for the ^{29}Si(p,γ) resonances were converted to absolute strengths (see definition in Sect. 5.5) using the results of Reinecke et al. [Rei85], who studied this reaction from $E_p = 0.3 - 2.3$ MeV. Reinecke included only $E_\gamma > 2.6$ MeV in his resonant yield. His relative strengths were converted to absolute strengths using the calibration standard of S = 1.04 $\pm$ 0.10 eV for the $E_p = 0.417$ MeV resonance measured by Riihonen et al. [Rii79]. The normalized areas of 17 of the resonances from this work were compared to the absolute strengths of those resonances measured by Reinecke as listed in Table 4.4. The 1.7472-MeV resonance was not included in this analysis due to the presence of the 1.7464-MeV contaminant in the excitation function, which was not observed by Reinecke. A multiplicative conversion factor, F_i, was then defined for each resonance as the ratio of the strength S measured by Reinecke to the normalized area obtained in this measurement, as shown in the Table 4.4. The errors on these conversion factors were calculated by propagating the errors on S and the normalized areas.

A final conversion factor $\overline{F}$ was calculated from this data by computing the weighted average [Bev92] of the ratios F_i,

$$\overline{F} = \sum_{i=1}^{17} \frac{(F_i/\sigma_i^2)}{(1/\sigma_i^2)}, \tag{4.3}$$

where each ratio in the sum is weighted inversely by ${\sigma_i}^2$. The corresponding uncertainty in $\overline{F}$ is given by

$${\sigma_{\overline{F}}}^2 = \sum_{i=1}^{17} \frac{1}{(1/\sigma_i^2)}. \tag{4.4}$$

Table 4.4. Conversion factors for the ^{29}Si(p,γ)^{30}P reaction.

E_p (MeV)	S [a] (eV)	Error (eV)	Area [b] (MeV cts)	Error (MeV cts)	F_i [c] (10^{-6} cts)	σ_{F_i} (10^{-6} cts)
1.1111	0.18	0.04	0.42	0.15	0.43	0.18
1.3020	1.60	0.30	2.9	0.29	0.56	0.12
1.3238	0.70	0.30	1.0	0.36	0.67	0.37
1.3268	2.40	0.90	5.4	1.9	0.44	0.23
1.3737	3.40	0.90	11	11.	0.30	0.31
1.4709	0.90	0.20	1.7	0.59	0.53	0.22
1.5020	0.09	0.03	0.17	0.06	0.54	0.26
1.5060	2.80	0.50	3.7	0.37	0.76	0.16
1.6393	4.00	1.20	26	26.	0.15	0.16
1.6639	0.90	0.20	2.8	0.28	0.33	0.08
1.6685	0.47	0.09	1.3	0.13	0.37	0.08
1.6844	5.50	1.40	22	7.8	0.25	0.11
1.7450	1.90	0.70	5.4	1.9	0.36	0.18
1.7698	0.80	0.30	3.0	1.0	0.27	0.14
1.7715	0.70	0.30	1.8	0.62	0.40	0.22
1.8530	0.38	0.10	1.3	0.13	0.30	0.08
1.9637	1.30	0.30	5.2	1.8	0.25	0.10

[a] From [Rei85]

[b] From Present work

[c] $F_i \equiv$ S / Area ; $\overline{F} = 0.36 \pm 0.03$

An S value was calculated for each of the 21 ^{29}Si(p,γ) resonances using the multiplicative factor $\overline{F} = 0.36 \pm 0.03$ (see Table 4.5). Note that the strengths of the three new resonances are on average about 2.5 times weaker than the smallest of the previously known ^{30}P resonances. There is good general agreement between our strengths and those measured by Reinecke, with only the 1.5060-MeV and 1.6393-MeV resonance strengths significantly different. The strengths of these two resonances are also different from an earlier measurement by Harris et al. [Har69] of S = 7.4 $\pm$ 1.5 eV for the 1.5060-MeV resonance and S = 21 $\pm$ 4 eV for the 1.6393-MeV resonance.

Table 4.5. Normalized strengths for the $^{29}Si(p,\gamma)^{30}P$ reaction.

	Previous work [a]		Present work	
E_p	S	error	S	error
(MeV)	(eV)	(eV)	(eV)	(eV)
1.0380			0.03	0.03
1.1110	0.18	0.04	0.15	0.05
1.3020	1.60	0.30	1.01	0.13
1.3238	0.70	0.30	0.37	0.05
1.3268	2.40	0.90	1.92	0.69
1.3737	3.40	0.90	4.00	4.0
1.4333			0.03	0.03
1.4709	0.90	0.20	0.60	0.22
1.5020	0.09	0.03	0.06	0.02
1.5060	2.80	0.50	1.30	0.17
1.5787			0.06	0.02
1.6393	4.00	1.20	9.24	9.2
1.6639	0.90	0.20	0.98	0.13
1.6685	0.47	0.09	0.46	0.06
1.6844	5.50	1.40	7.97	2.9
1.7450	1.90	0.70	1.91	0.69
1.7472	4.70	1.40	4.02	1.45
1.7698	0.80	0.30	1.05	0.38
1.7715	0.70	0.30	0.63	0.23
1.8530	0.38	0.10	0.46	0.06
1.9637	1.30	0.30	1.86	0.67

[a] From [Rei85]

Chapter 5

Gamma-ray Decay Analysis and Results

This chapter discusses the analysis of the gamma-ray decay data and summarizes the results of this analysis. In general, for a particular ^{29}Si(p,γ) resonance, the analysis consisted of first extracting areas and centroids from gamma-ray peaks in the CSGe and USGe spectra. This information was then used to construct a ^{30}P decay scheme for that resonance. The transition strengths of the primary decays from each of the 17 ^{29}Si(p,γ) resonances studied were used to assign possible spins, parities, and isospins to each level. For the purpose of clarity of presentation, only the analysis of the resonance at $E_x = 6853.9$ keV will be discussed in detail.

The fitting procedure is discussed in Sect. 5.1, and Sect. 5.2 discusses the energy and efficiency calibrations used to precisely determine the energies and relative intensities of the gamma-rays for the 6853.9-keV resonance. Sect. 5.3 details the methods used to identify and place ^{30}P γ-rays within the decay scheme for this resonance. Sect. 5.4 gives the results of the energy level and branching ratio measurements for the 6853.9-keV resonance. The procedure for assigning possible quantum numbers is described in Sect. 5.5. A summary of the current status of the ^{30}P level scheme and the J, π, and T assignments for each of the analyzed ^{30}P levels is given in Sect. 5.6.

5.1 Fitting Procedure

All gamma-ray peaks within the spectra were fit using the gamma-ray analysis program GELIFT, obtained from Argonne National Laboratory. This program is a least-squares fitting routine specifically designed for analysis of gamma-ray spectra produced by germanium detectors [Rad89]. The GELIFT program is capable of simultaneously fitting a section of spectra containing up to 15 gamma-ray peaks on a linear or quadratic background. The shape of the majority of the gamma-ray peaks were consistent with a Gaussian functional form. Occasionally, a Gaussian convoluted with a step function (to increase the background on the low-energy side of the peak) was required.

A sample fit to a section of an energy calibration spectrum used to calibrate the $E_p =$ 6853.9-keV resonance gamma-rays is shown in Fig. 5.1. GELIFT computes the centroid (in channels), the width, the height, the area above the background, and the errors on each of these quantities from the best fit to peaks in a region of a particular spectrum. A .STO file was produced for each set of spectra analyzed, containing the centroid and areas, along with their associated errors, for each fitted peak. This information was then calibrated (as explained in the next section) and used as the basis for all subsequent analysis.

5.2 Calibrations

Since the gamma-rays of interest for this work represent transitions between two energy levels in the ^{30}P nuclide, the energies of these γ-rays ultimately determine the energies of these two levels within the decay scheme of a given resonance. Furthermore, the relative areas of those ^{30}P gamma-rays which represent primary decays from the resonance state to states of lower energy are converted to reduced transition strengths, which in turn are used to limit the J, π, and T possibilities for that resonant level. Therefore, precise calibrations are essential to ensure both accurate energies and intensities of the ^{30}P γ-rays.

The online calibrations discussed in Sect. 3.6.2 were used only as an aid in monitoring the data during an experiment and were not of sufficient quality to be used in the subsequent data analysis. Therefore, offline energy calibrations were performed that related

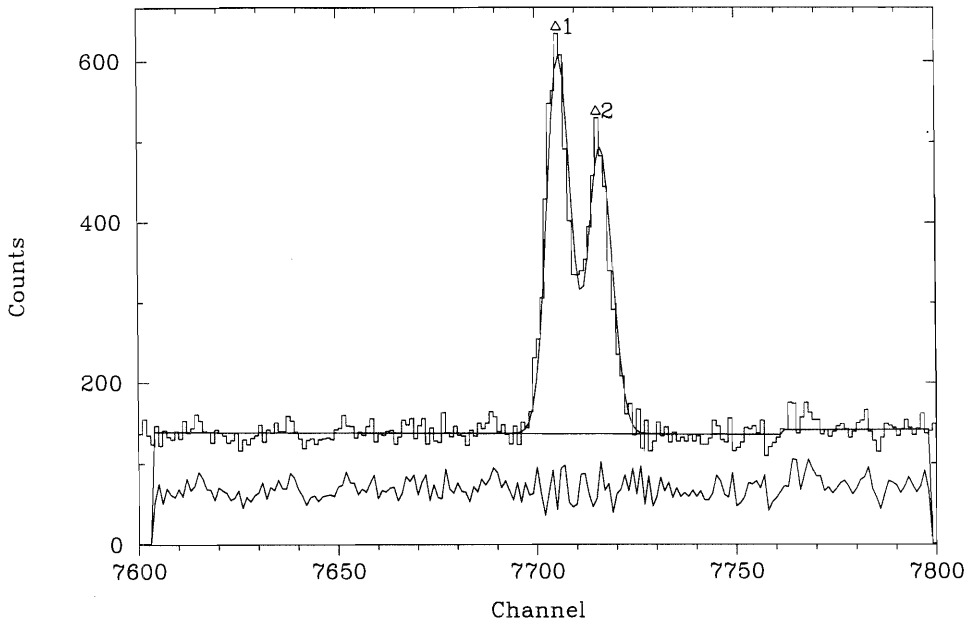

Figure 5.1. Data and fit to the 7923 ($\triangle$1) and 7933 ($\triangle$2) keV gamma-ray peaks from the ^{27}Al(p,γ) reaction. The smooth line is the best fit to the two peaks and the background. The jagged line below the background is the deviation of the fit from the data at each channel in this plot.

the energies of well known (calibration) source γ-rays to the channel numbers of their corresponding peaks in the gamma-ray spectra. In addition, since the photopeak response of a germanium detector changes with γ-ray energy, this effect must be corrected in order to accurately measure the relative intensities of the gamma-rays over their entire energy range. Therefore, efficiency calibrations also were performed that related the relative intensities of certain source gamma-rays to the areas of the corresponding peaks in the spectra.

5.2.1 Energy Calibrations

As discussed in Sect. 3.6.2, gamma-rays from ^{152}Eu (listed in Table 5.1) and from the ^{27}Al(p,γ) reaction (listed in Table 5.2) were used to perform energy calibrations of the gamma-ray spectra of both detectors. The energy calibration for the unsuppressed HPGe (USGe) detector was used to determine ^{30}P γ-ray energies, since the placement at 90° prevented Doppler shifts of the peaks in the USGe spectrum. In addition, although the

Table 5.1. ^{152}Eu source γ-rays [a].

E_γ (keV)	E_γ Error (keV)	I_γ (Relative)	I_γ Error (Relative)
244.692	0.002	3590	60
295.939	0.008	211	5
344.276	0.004	12750	90
367.789	0.005	405	8
411.115	0.005	1070	10
488.661	0.039	195	2
688.678	0.006	400	8
778.903	0.006	6190	80
867.388	0.008	1990	40
964.131	0.009	6920	90
1212.950	0.012	670	8
1299.124	0.012	780	10
1408.011	0.014	10000	30

[a]From [Led78].

background present in the USGe spectrum is higher than in the suppressed HPGe (CSGe) spectrum, this had a minimal effect on the position of the centroids of the γ-ray peaks. Fig. 5.2 shows the source gamma-ray peaks from 245 to 1408 keV used for the low-energy (< 1523 keV) calibration of the gamma-ray peaks in the USGe spectrum. Fig. 5.3 shows the source gamma-ray peaks from 1523 to 7933 keV used for the high-energy calibration of the USGe peaks.

These source gamma-ray peaks were fit using the GELIFT program and the results stored in a .STO file. The program SOURCE was used to produce a source intensity .SIN file that contained the energy of each of the source gamma-rays and its corresponding channel number within a particular spectrum. A program ENCAL was then used on the .SIN file to perform a least squares fit to the data with an order n (≤ 5) polynomial. The gamma-ray energy $E_\gamma(x)$ is then given by

$$E_\gamma(x) = \sum_{i=0}^{n} c_i x^i, \tag{5.1}$$

where c_i are the fitting coefficients and x is the channel of the centroid of a gamma-ray peak in the spectrum. The fitting coefficients listed in Table 5.3 are used to relate the

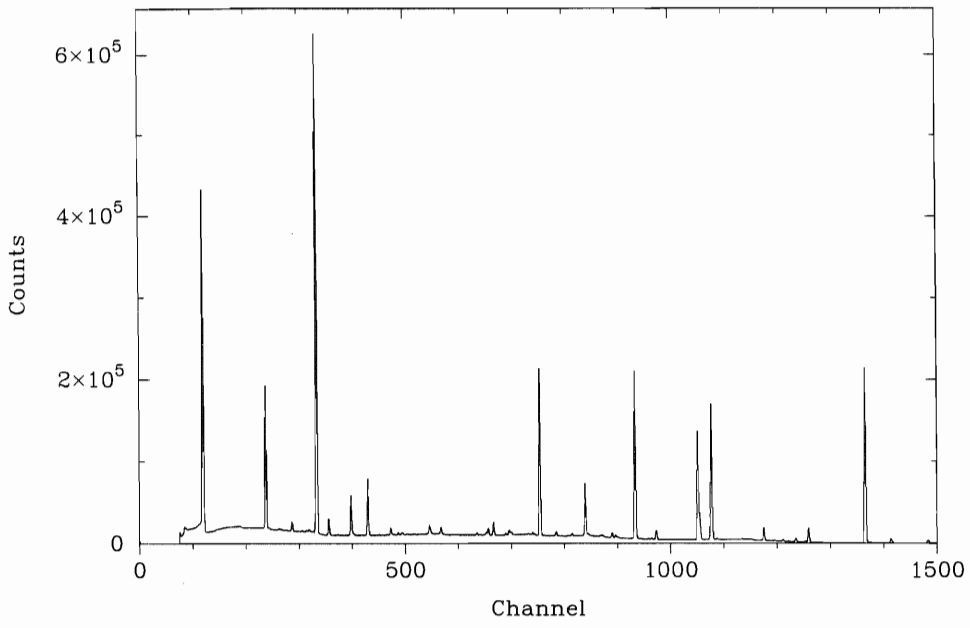

Figure 5.2. A portion of the USGe spectrum ($E_\gamma = 0 - 1523$ keV) showing the ^{152}Eu gamma-rays used for the low-energy energy calibration.

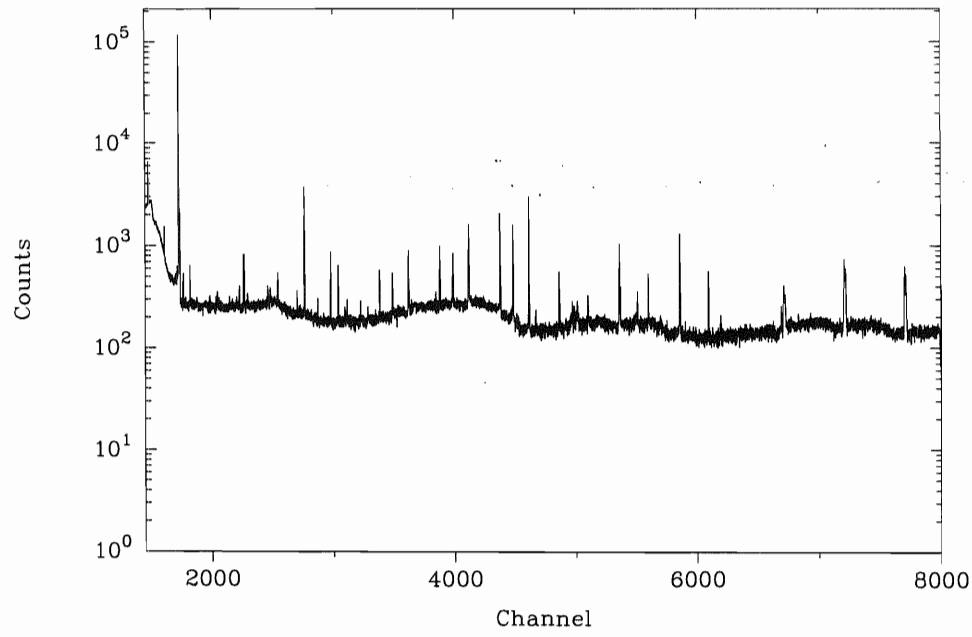

Figure 5.3. A portion of the USGe spectrum ($E_\gamma = 1523 - 8000$ keV) showing the ^{28}Si gamma-rays used for the high-energy energy calibration.

Table 5.2. ^{28}Si source γ-rays[a].

E_γ (keV)	E_γ Error (keV)	I_γ (Relative)	I_γ Error (Relative)
1522.81	0.02	2787	94
1658.34	0.02	610	16
1779.03	0.02	94766	4
1873.26	0.02	288	9
2838.83	0.03	5598	4
3061.82	0.03	1110	40
3124.14	0.03	790	30
4497.17	0.05	4563	26
4607.86	0.05	3960	120
4742.30	0.05	8500	300
4799.31	0.05	287	11
5662.52	0.06	700	20
6019.98	0.06	5634	94
6265.11	0.06	2150	70
6878.79	0.07	498	8
7923.45	0.08	4090	120
7933.45	0.08	3309	60

[a]From [End90b].

Table 5.3. USGe energy calibration parameters.

Order [a] (i)	Low-Energy (< 1523 keV)	High-Energy (≥ 1523 keV)
0	$-.3485 \times 10^{1}$	0.5578×10^{1}
1	0.1059×10^{1}	0.1030×10^{1}
2	$-.6274 \times 10^{-4}$	$-.2690 \times 10^{-5}$
3	0.7834×10^{-7}	0.7345×10^{-9}
4	$-.4933 \times 10^{-10}$	$-.8618 \times 10^{-13}$
5	0.1171×10^{-13}	0.3924×10^{-17}

[a] Fit order, i, is from Equation 5.1.

centroid of a particular peak to the appropriate gamma-ray energy.

The particular polynomial that best reflects the calibration data was chosen by calculation of the mean square deviation $\langle \Delta^2 \rangle^{1/2}$ of this polynomial for N calibration γ-rays of energy E_j,

$$\langle \Delta^2 \rangle^{1/2} = \sqrt{\sum_{j=1}^{N} [E_j - E_\gamma(x_j)]^2} \ . \tag{5.2}$$

The fitting function that yielded the smallest mean square deviation was chosen as the best fit to the calibration data. The best fit to the low-energy calibration ^{152}Eu data is shown in Fig. 5.4. The lower figure in this plot shows the difference between the known energy of each source γ-ray and the energy obtained from the fitting coefficients. The corresponding plot for the high-energy calibration data is shown in Fig. 5.5.

Gamma-rays from the two calibration regions listed in Tables 5.1 and 5.2 do not exist for $E_\gamma = 1408 - 1523$ keV. It is therefore unclear which calibration polynomial is appropriate for γ-rays with energies within this energy region. This issue was resolved by adding the 1523-keV ^{28}Si source gamma-ray to the ^{152}Eu calibration source data set contained in the .SIN file. This addition to the ^{152}Eu data set ensured that the fitting polynomials from the low- and high-energy calibrations smoothly approached each other at 1523 keV. The low-energy calibration was then repeated with this new data set.

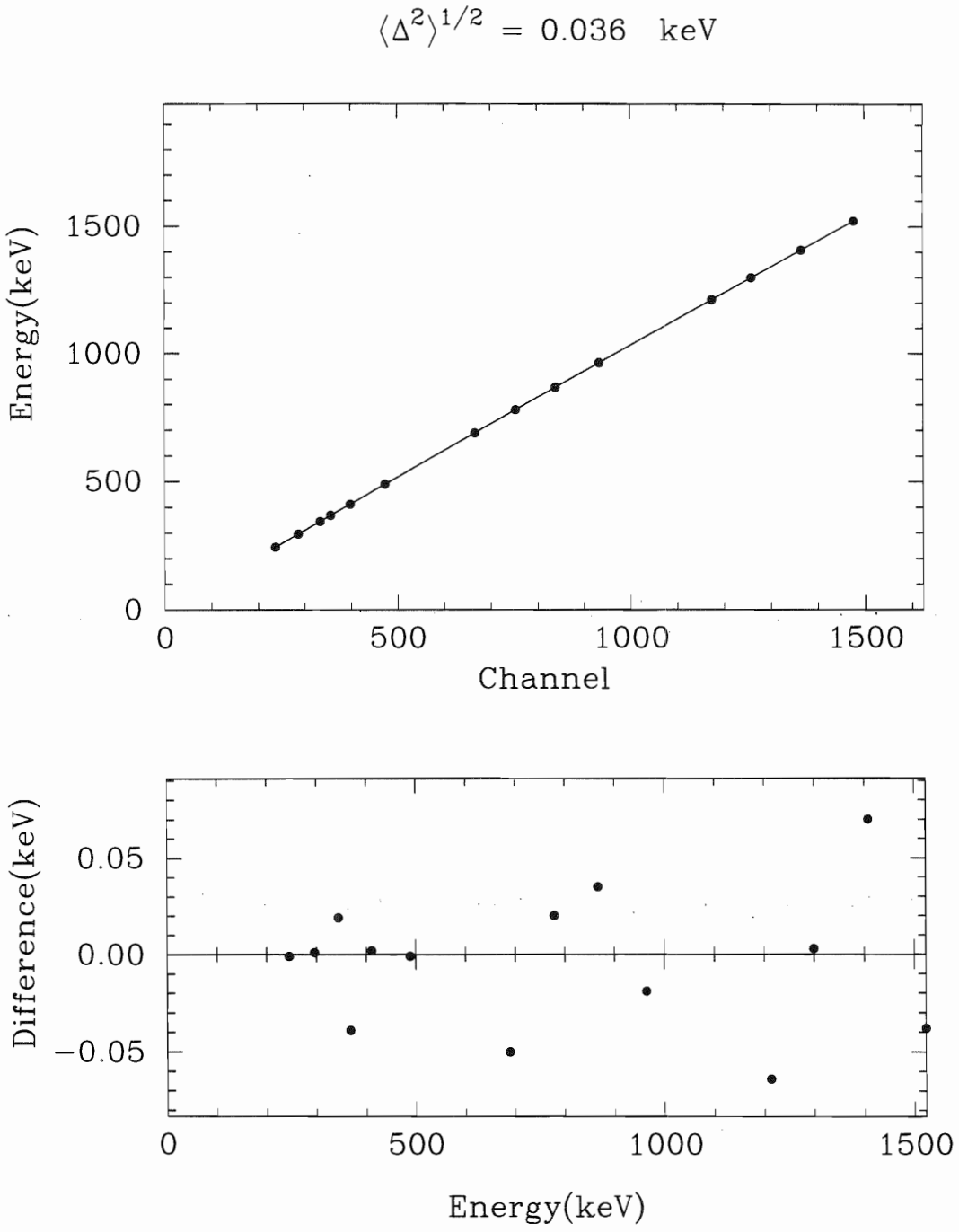

Figure 5.4. USGe detector low-energy calibration using ^{152}Eu source. The data points and 5^{th}-order polynomial fit are shown in the upper graph. The difference between the data points and this fit are shown in the bottom graph.

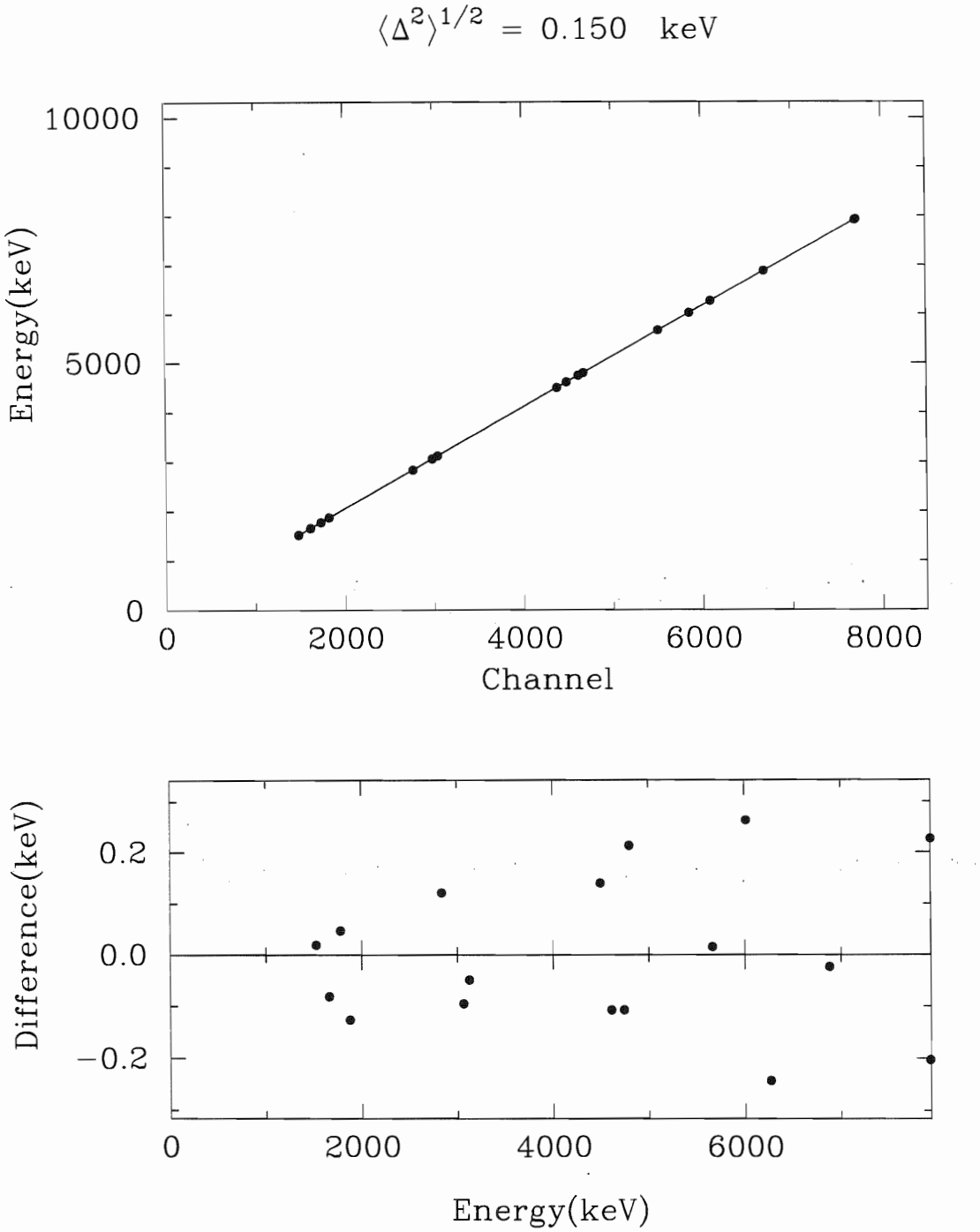

Figure 5.5. USGe detector high-energy calibration using ^{28}Si γ-rays. The data points and 5^{th}-order polynomial fit are shown in the upper graph. The difference between the data points and this fit are shown in the bottom graph.

5.2.2 Efficiency Calibrations

The efficiency calibration data were accumulated with the identical geometrical detector configuration as used to accumulate gamma-ray spectra for the ^{30}P resonances. Any difference in the configuration of the detectors between the calibration data and the resonance data severely degrades the accuracy of the efficiency calibration. Although efficiency calibrations were performed on spectra from both detectors, only the calibration for the CSGe detector was used to ultimately determine the relative intensities of the ^{30}P γ-rays. The lower background under the peaks in the CSGe spectrum compared to the USGe spectrum reduced the relative errors on the areas of the peaks of interest in the spectra. The same sources of gamma-rays (listed in Tables 5.1 and 5.2) used for the energy calibrations were also used for the efficiency calibrations.

The two .SIN files used in the low- and high-energy calibrations were also used as input to the program EFFIT to perform the efficiency calibrations. The areas of the ^{152}Eu source gamma-ray peaks were combined with the areas of the ^{28}Si peaks into a single input data set. The EFFIT program used a seven parameter function, which empirically describes the variation of the photopeak efficiency ϵ [Rad89] as a function of γ-ray energy E_γ (keV) according to

$$\epsilon = \exp\left[\left\{[A + Bu + Cu^2]^{-G} + [D + Ev + Fv^2]^{-G}\right\}^{\frac{-1}{G}}\right], \qquad (5.3)$$

where $u = \ln\left(\frac{E_\gamma}{100}\right)$, $v = \ln\left(\frac{E_\gamma}{1000}\right)$. A normalization factor was used for the ^{28}Si source gamma-rays to align their intensities with the ^{152}Eu intensities according to this calibration curve, since only relative efficiencies are of interest.

A least squares fit of this function to the gamma-ray data set determined the values of the parameters A through G listed in Table 5.4. As with the energy calibration, the best fit to the data was chosen by selecting the fit with the minimum mean square deviation $\langle\Delta^2\rangle^{1/2}$. However, here the mean square deviation of the data from the fit was expressed as a percentage instead of as an energy. Fig. 5.6 shows the CSGe calibration data and best fit used for the 6853.9-keV ^{30}P resonance data. The difference between this calibration data and the fit is shown on the bottom graph.

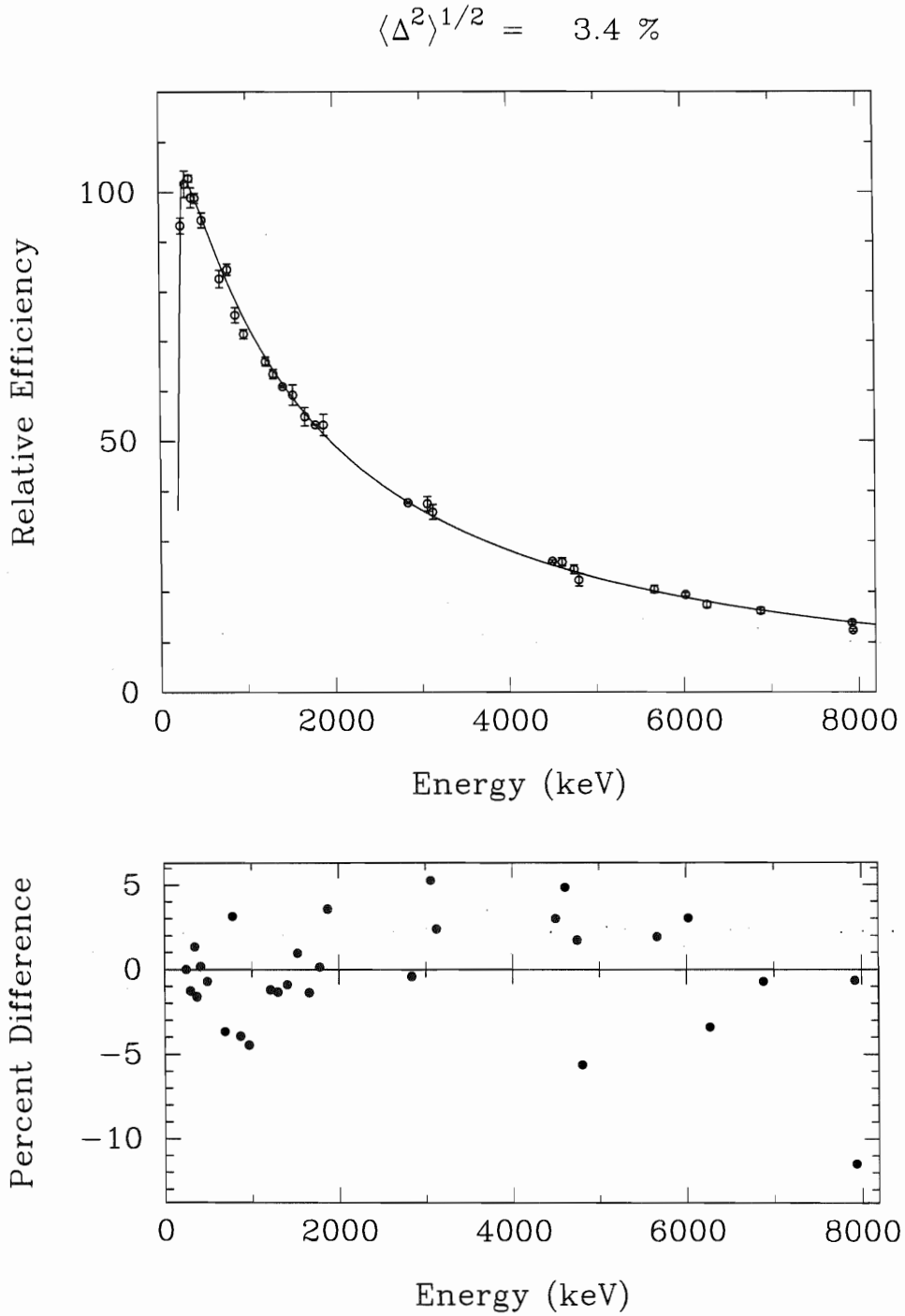

Figure 5.6. Data and fit of CSGe detector efficiency calibration. The data points and 5^{th}-order polynomial fit are shown in the upper graph. The difference between the data points and the fit are shown in the bottom graph.

Table 5.4. Efficiency calibration parameters.

Parameter [a]	CSGe detector [b]	USGe detector [c]
A	0.315	4.089
B	4.881	2.456
C	0.000	0.000
D	4.298	5.326
E	-0.472	-0.608
F	-0.159	-0.158
G	24.885	10.00

[a] From [Rad89].

[b] $\langle\Delta^2\rangle^{1/2} = 3.4\%$ as shown in Fig. 5.6.

[c] $\langle\Delta^2\rangle^{1/2} = 3.5\%$.

5.3 Gamma-ray Assignments

The primary analysis of the γ-ray spectra from both detectors proceeded after the calibrations were completed. As discussed in Sect. 3.6.2, a measurement of the background radiation within the HRL was performed before each gamma-ray decay experiment. The background spectra from this measurement performed before the 6853.9-keV resonance experiment are shown in Fig. 5.7 and 5.8. A spectrum accumulated for 200,000 μC at $E_p = 1.302$ MeV (on resonance) for the CSGe detector is shown in Fig. 5.9. An off-resonance spectrum (shown in Fig. 5.10) was also accumulated at $E_p = 1.310$ MeV for the same amount of collected charge as the on-resonance spectrum. The energy and intensity of the γ-ray peaks in the CSGe spectrum were extracted from fits to these peaks using the GELIFT program. Since the peaks of smallest intensity are observed in the CSGe spectrum, only the corresponding peaks present in the USGe spectrum were fit. This information was used to identify the ^{30}P γ-rays and thus build a decay scheme for the 6853.9-keV resonance.

Each gamma-ray peak in the on-resonance CSGe spectrum was assigned as a contaminant, as an escape peak, as a ^{30}P γ-ray, or as unknown (unassigned). Contaminant gamma-rays were those peaks in the on-resonance spectrum also present (with the expected intensity) in the room background or the off-resonance spectrum. In addition, a γ-ray was

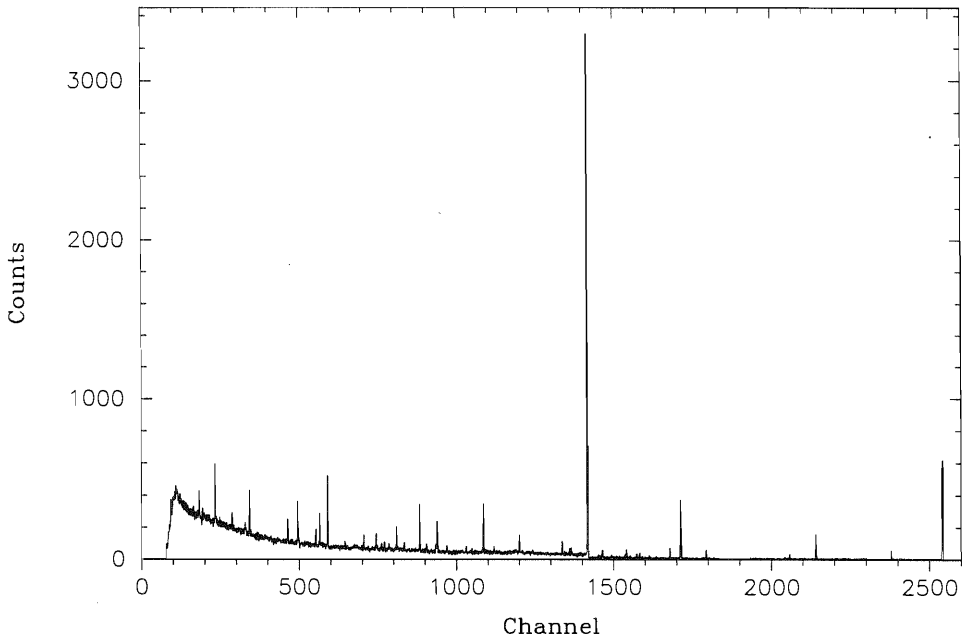

Figure 5.7. Background spectrum for the CSGe detector from $E_\gamma = 0 - 2700$ keV. No peaks with $E_\gamma > 2620$ keV were observed in room background.

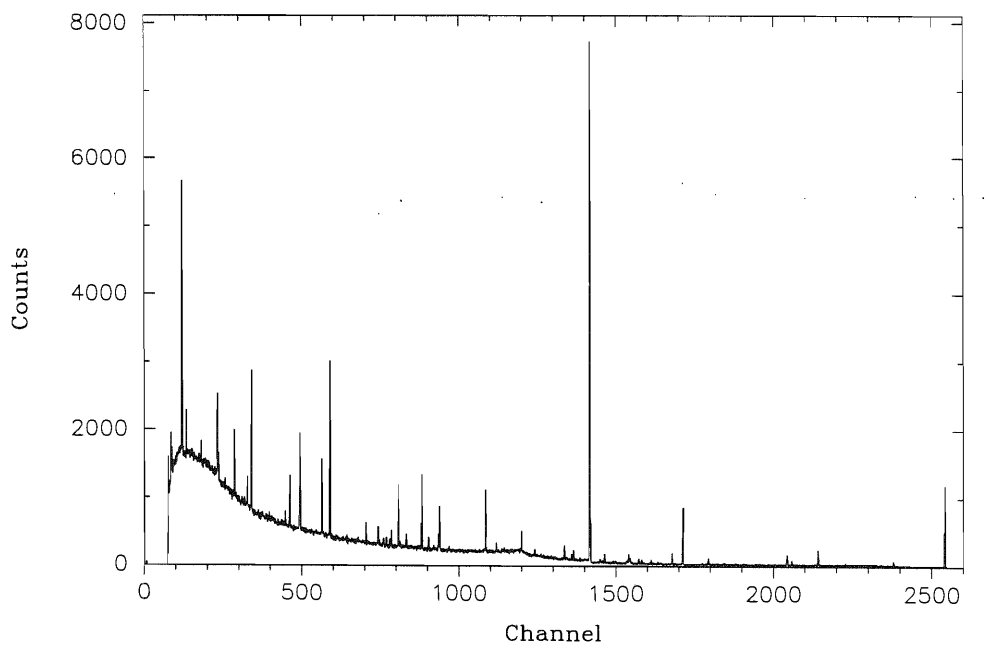

Figure 5.8. Background spectrum for the USGe detector.

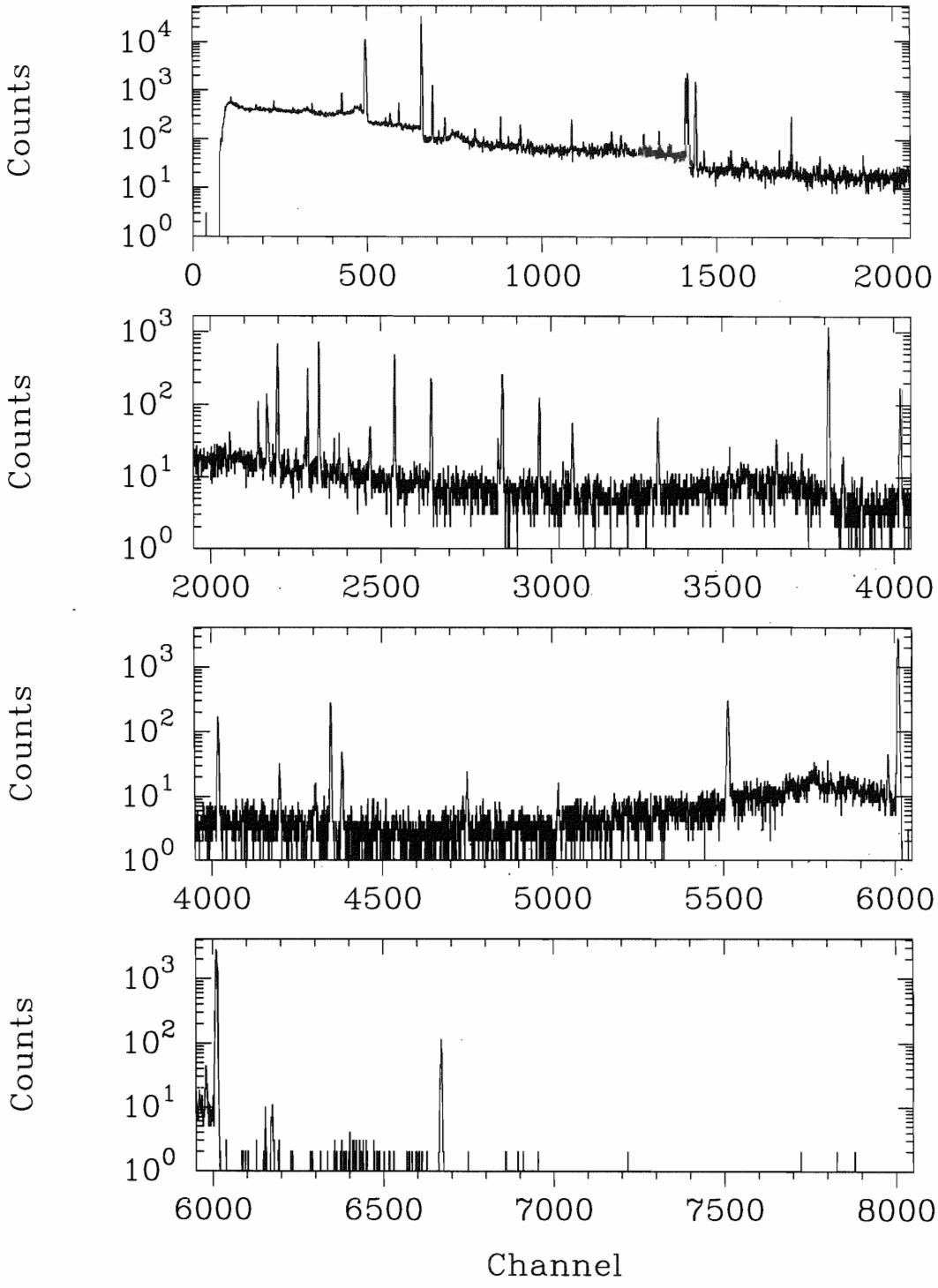

Figure 5.9. CSGe on-resonance spectrum for the $E_x = 6853.9$ keV resonance.

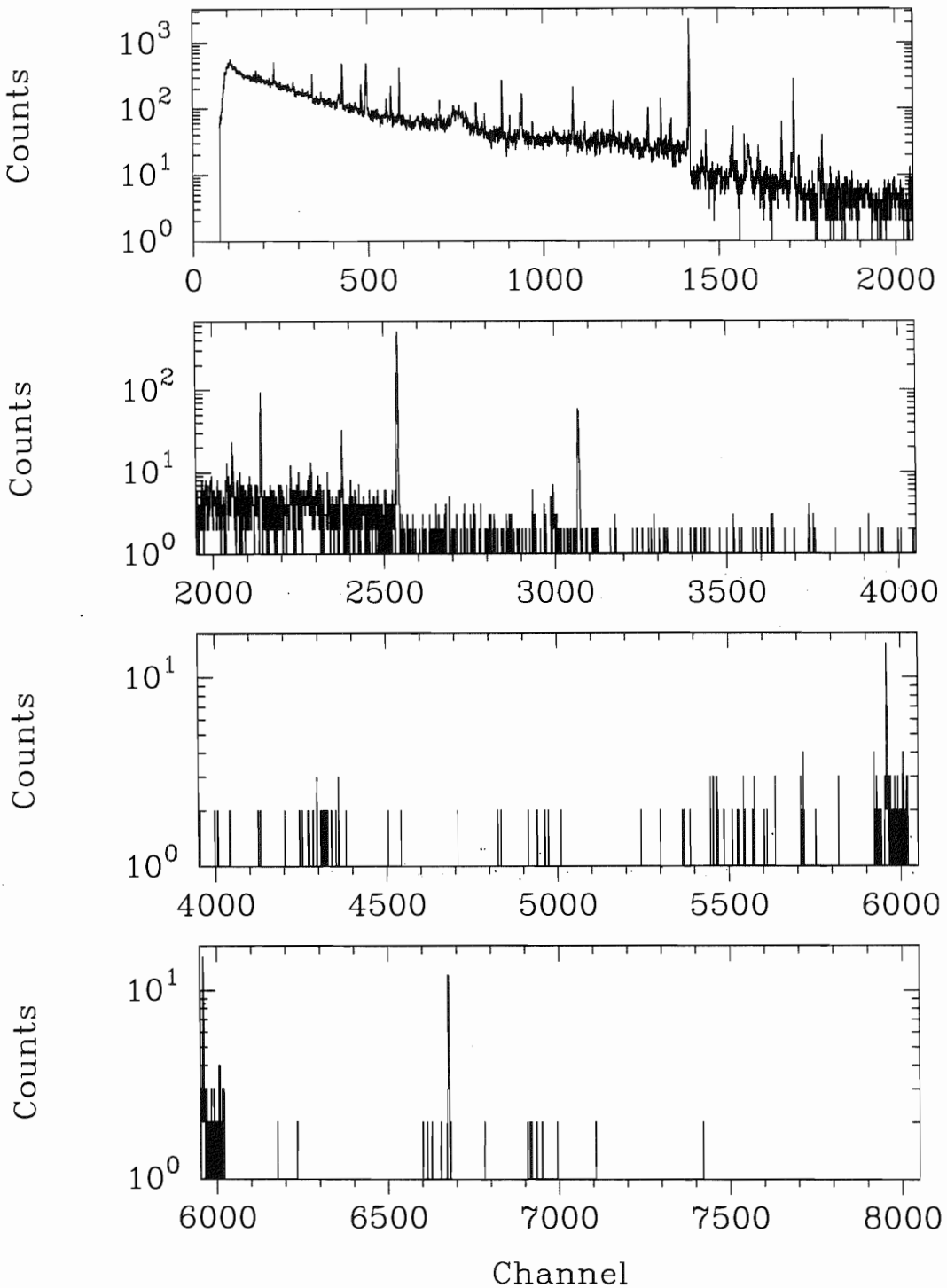

Figure 5.10. CSGe off-resonance spectrum for the $E_x = 6853.9$ keV resonance.

assigned as an escape peak by computing a "suppression factor"; the ratio of the area of the photopeak to the area of the suspected escape peak in the CSGe spectrum normalized to the ratio for the corresponding peaks in the USGe spectra. For suspected single escape peaks, the presence of an escape peak at the expected energy and with a suppression factor of about 7 resulted in an assignment of the γ-ray as an escape peak.

The program COMBINE was used to correct the areas of the γ-ray peaks for efficiency and output the energies (from the USGe spectrum) and the corrected intensities (from the CSGe spectrum) in a format suitable for input to the analysis program, GRAY. Based on the results of the energy calibration, the gamma-ray energies were assigned a 0.2-keV error for $E_\gamma < 1523$ keV and 0.4-keV error for $E_\gamma \geq 1523$ keV. Occasionally, a larger error was assigned for ^{30}P peaks observed only in the CSGe spectrum. Here, the CSGe energy of this γ-ray was converted to an (unshifted) USGe energy by matching the percentage of Doppler shift observed between neighboring ^{30}P gamma-rays. The relative efficiencies of all γ-rays were assigned an uncertainty based on the value of the $\langle\Delta^2\rangle^{1/2}$ calculated from the efficiency calibration curve. For the 6853.9-keV resonance, the efficiency calibration results gave a 4 % efficiency error which was assigned to the relative intensities of all the γ-rays in the CSGe spectrum.

The program GRAY was used to search a database for possible sources of the contaminant γ-rays. This database represents all the identified sources of contaminant γ-rays observed in similar experimental work [Dra94][Byb95][Wal96]. The energies, intensities and their associated errors, and the sources of the 139 gamma-rays observed in the decay of the 6853.9-keV resonance are summarized in Table 5.5. Those listed as room background are various members of the decay chains of ^{40}K, ^{232}Th, and ^{238}U. Also listed are several gamma-rays from ^{19}F and ^{23}Na nuclei arising from impurities within the carbon backing foils of the target. The ^{56}Fe γ-rays are probably a result of the outer edge of the proton beam striking the stainless steel target holders during an experiment. The relative intensities and their errors of the γ-ray peaks listed in Table 5.5 were computed by scaling the GELIFT areas and their errors to the strongest gamma-ray at $E_\gamma = 677$ keV.

Table 5.5. γ-rays from the $E_x = 6853.9$ keV resonance.

E_γ [a] (keV)	I_γ (keV)	σ_{I_γ} (keV)	E_i (keV)	E_f (keV)	Assigned (keV)
110.5	26.7	3.7	109.9	0.	^{19}F
117.9 [d,f]	4.0	2.0			
122.0 [b]	4.9	1.7			
126.9 [b]	4.1	1.5			
172.4 [c]	0.47	0.36			
186.3	1.25	0.24	186.18	0.	^{226}Ra
197.8	0.49	0.15	197.1	0.	^{19}F
208.4 [b]	0.36	0.12			
227.7 [b]	0.080	0.058			
233.8 [d,f]	0.083	0.050			
238.5	0.567	0.067	238.63	0.	^{212}Pb
241.4	0.163	0.048	240.981	0.	^{220}Rn
248.3 [b]	0.089	0.044			
295.1	0.193	0.090	295.21	0.	^{214}Pb
338.1	0.259	0.046	396.1	57.8	^{228}Th
341.3 [b]	0.147	0.043			
347.0 [b]	0.050	0.040			
351.7	0.437	0.055	351.92	0.	^{214}Pb
425.7 [c]	0.171	0.050			
432.6 [c]	0.176	0.048			
439.7	1.77	0.087	440.0	0.	^{23}Na
477.4	0.535	0.070	875.0	0.	^{228}Ac
482.9 [c]	0.379	0.069			
487.3 [b]	0.440	0.073			
491.2 [f]	0.236	0.070			
495.0 [c]	0.569	0.074			
510.7	52.7	0.35	3708.5	3197.7	^{208}Tl
566.1 [d]	0.062	0.031			
569.8	0.176	0.046	569.7	0.	^{208}Pb
583.0	0.435	0.059	3197.7	2614.6	^{208}Tl
586.8 [c]	0.152	0.050			
609.0	1.026	0.069	609.31	0.	^{214}Bi
677.0	100	0.48	677.29	0.	^{30}P
708.7	3.76	0.080	709.02	0.	^{30}P
726.9	0.190	0.035	727.3	0.	^{212}Bi
742.6 [d]	0.089	0.039			

Table 5.5. (continued.)

E_γ [a] (keV)	I_γ (keV)	σ_{I_γ} (keV)	E_i (keV)	E_f (keV)	Assigned (keV)
745.3	0.570	0.055	1454.67	709.02	^{30}P
763.7 [c]	0.102	0.040			
768.0	0.221	0.044	1377.68	609.31	^{214}Bi
771.3 [c]	0.151	0.040			
779.8 [c]	0.155	0.040			
786.1	0.151	0.043	2447.72	1661.28	^{214}Bi
794.8	0.116	0.034	1122.8	328.0	^{228}Ac
806.0 [d]	0.068	0.030			
810.5	0.063	0.030	3121.4	2311.4	^{56}Fe
813.6 [d,f]	0.089	0.031			
824.5 [d,f]	0.039	0.028			
834.7	0.337	0.045	1022.4	186.9	^{228}Ac
838.9 [d]	0.082	0.033			
840.9 [c]	0.074	0.029			
850.2 [b]	0.036	0.028			
860.4	0.136	0.035	3475.0	2614.6	^{208}Tl
862.8 [d]	0.041	0.029			
867.3	0.050	0.026	1168.5	328.0	^{228}Ac
869.9 [b]	0.089	0.030			
911.0	0.749	0.057	968.8	57.8	^{228}Ac
933.8	0.143	0.041	1543.37	609.31	^{214}Bi
964.4	0.152	0.033	2937.87	1973.62	^{30}P
968.8	0.504	0.049	968.8	0.	^{228}Ac
990.2 [d]	0.055	0.035			
992.0	0.217	0.031	3928.9	2937.87	^{30}P
999.8 [b]	0.093	0.043			
1001.6 [b]	0.089	0.043			
1033.3 [d]	0.080	0.036			
1062.8 [b]	0.124	0.049			
1120.0	0.829	0.063	1729.21	609.31	^{214}Bi
1155.2	0.108	0.035	1764.51	609.31	^{214}Bi
1173.5 [b]	0.156	0.046			
1237.8	0.398	0.054	1847.44	609.31	^{214}Bi
1264.9	0.442	0.057	1973.62	709.02	^{30}P
1276.5 [b]	0.176	0.046			
1281.0	0.122	0.045	1890.28	609.31	^{214}Bi

Table 5.5. (continued.)

E_γ [a] (keV)	I_γ (keV)	σ_{I_γ} (keV)	E_i (keV)	E_f (keV)	Assigned (keV)
1328.3 [b]	0.098	0.033			
1330.0 [d]	0.384	0.044			
1377.3	0.516	0.049	1377.6	0.	^{56}Fe
1401.0	0.109	0.030	2010.82	609.31	^{214}Bi
1407.7	0.186	0.034	2017.3	609.31	^{214}Bi
1454.3	9.99	0.16	1454.67	0.	^{30}P
1460.6	12.0	0.18	1460.81	0.	^{40}K
1483.1	8.87	0.15	2937.87	1454.67	^{30}P
1496.1	0.062	0.026	1683.3	186.9	^{228}Ac
1508.9	0.246	0.041	2118.55	609.31	^{214}Bi
1537.8	0.095	0.029	2147.8	609.3	^{214}Bi
1582.9 [d]	0.114	0.030			
1588.2	0.236	0.039	1643.1	57.8	^{228}Ac
1592.6 [d]	0.043	0.028			
1620.0	0.181	0.039	1620.6	0.	^{212}Bi
1630.9 [b]	0.156	0.041			
1638.4	0.122	0.035	1638.2	0.	^{214}Bi
1661.5	0.065	0.057	1661.28	0.	^{214}Bi
1684.4 [b]	0.060	0.024			
1691.4 [d,f]	0.049	0.024			
1729.5	0.263	0.043	1729.61	0.	^{214}Bi
1750.2 [e]	0.048	0.023	2937.87	677.29	^{30}P
1757.8	0.073	0.025	1757.6	0.	^{56}Fe
1764.5	1.53	0.082	1764.51	0.	^{214}Bi
1847.2	0.205	0.043	1847.44	0.	^{214}Bi
1973.9	0.203	0.041	1973.62	0.	^{30}P
2103.6	0.121	0.034	2614.6	0.	^{208}Tl
2118.0	0.222	0.044	2118.55	0.	^{214}Bi
2204.3	0.627	0.053	2204.09	0.	^{214}Bi
2210.5 [d]	0.077	0.026			
2229.1	0.972	0.069	2937.87	709.02	^{30}P
2233.6 [d]	0.376	0.048			
2260.8	6.57	0.18	2937.87	677.29	^{30}P
2342.4	0.206	0.034	3019.39	677.29	^{30}P
2350.6	2.51	0.11	6853.9	4502.32	^{30}P
2384.6	5.97	0.17	6853.9	4468.33	^{30}P

Table 5.5. (continued.)

E_γ [a] (keV)	I_γ (keV)	σ_{I_γ} (keV)	E_i (keV)	E_f (keV)	Assigned (keV)
2431.8	0.188	0.038	6853.9	4422.4	^{30}P
2448.2	0.170	0.034	2447.72	0.	^{214}Bi
2475.8	0.162	0.046	3928.9	1454.67	^{30}P
2538.9	0.511	0.062	2539.03	0.	^{30}P
2614.8	4.37	0.15	2614.6	0.	^{208}Tl
2724.2	2.97	0.13	2723.96	0.	^{30}P
2924.8	0.304	0.049	6853.9	3928.9	^{30}P
2938.2	3.58	0.15	2937.87	0.	^{30}P
3048.2	1.325	0.092	4502.32	1454.67	^{30}P
3119.3 [d]	0.114	0.031			
3143.6 [c]	0.800	0.077			
3387.3 [d,f]	0.074	0.030			
3404.3 [e]	0.923	0.083	6853.9	2937.87	^{30}P
3760.0	0.388	0.058	4468.33	709.02	^{30}P
3794.8	0.165	0.041	4502.32	709.02	^{30}P
3833.4	0.183	0.041	6853.9	3019.39	^{30}P
3915.5	19.6	0.37	6853.9	2937.87	^{30}P
3958.0 [e]	0.295	0.060	4468.33	0.0	^{30}P
4129.7	2.72	0.15	6853.9	2723.96	^{30}P
4315.2	0.482	0.069	6853.9	2539.03	^{30}P
4422.7	0.261	0.062	4422.4	0.	^{30}P
4469.1	5.97	0.22	4468.33	0.	^{30}P
4504.3	0.86	0.13	4502.32	0.	^{30}P
4873.2 [d,f]	0.131	0.036			
4880.1	0.407	0.068	6853.9	1973.62	^{30}P
5154.2 [e]	0.259	0.060	6853.9	677.29	^{30}P
5665.6 [e]	9.63	0.32	6853.9	677.29	^{30}P
6145.9	1.03	0.13	6853.9	709.02	^{30}P
6176.6	90.6	0.99	6853.9	677.29	^{30}P
6342.8 [e,g]	0.396	0.075	6853.9	0.0	^{30}P
6853.9	3.60	0.21	6853.9	0.	^{30}P

[a] Error on E_γ:
0.2 keV for $E_\gamma < 1523$ keV, 0.4 keV for $E_\gamma \geq 1523$ keV

[b] Present in room background.

[c] Present off resonance.

[d] Present on resonance.

[e] Escape Peak.

[f] Present only in CSGe spectrum.

[g] 0.6 keV error assigned to this peak, energy obtained from correcting for Doppler shift of CSGe E_γ.

Table 5.6. Feeding/decay balance for the $E_x = 6853.9$ keV resonance.

E_x (keV)	Relative Intensity In	Error	Relative Intensity Out	Error
0.0	132	0.65	0.0	
677.29	97.4	1.0	100	0.48
709.02	3.57	0.18	3.76	0.08
1454.67	10.4	0.18	10.6	0.17
1973.62	0.559	0.08	0.645	0.07
2539.03	0.482	0.07	0.511	0.06
2723.96	2.72	0.15	2.97	0.13
2937.87	19.8	0.37	20.1	0.29
3019.39	0.183	0.04	0.206	0.03
3928.9	0.304	0.05	0.379	0.05
4422.4	0.188	0.04	0.26	0.06
4468.33	5.97	0.17	6.36	0.23
4502.32	2.51	0.11	2.35	0.16
6853.9	0.0		127	1.1

With the contaminant γ-rays identified, the GRAY program was also used to compare the energy of each unassigned γ-ray to previously known ^{30}P gamma-ray decay information. GRAY suggests the specific transitions that might correspond to unassigned gamma-rays that fall within $\pm$ 3 keV of a known ^{30}P γ-ray. The presence of other feeding and decaying gamma-rays to and from the relevant levels of a suggested transition was also checked. Furthermore, the sum of the intensities of all gamma-rays feeding into and decaying from both of the ^{30}P levels involved in a transition should be equal. A gamma-ray that resulted in an intensity imbalance for either transition level is probably not from ^{30}P. The 34 γ-rays assigned as ^{30}P in the 6853.9-keV resonance resulted in a well-balanced decay scheme as shown in Table 5.6.

The assignment of gamma-rays as transitions from certain ^{30}P levels were also based on the branching ratios that describe the decay from those levels. The branching ratio for a particular transition is defined as the ratio of the intensity of that particular transition from a certain level to the sum of the intensities of all transitions from that same level. The intensity of a new ^{30}P transition from a given level should be consistent with the known

branching ratios for that level. The GRAY program lists the intensities of ^{30}P gamma-rays for comparison with the expected intensities computed from the branching ratios measured by previous researchers. Table 5.7 shows this comparison for the resonance at $E_x = 6853.9$ keV. The intensities observed in this work agree very well with that of previous research.

Two additional techniques were used to identify γ-rays as originating from ^{30}P. Gamma-rays which represented transitions from various levels with larger than ± 3 keV energy uncertainties [End90a] were also investigated. Since no branching ratio information was usually available for these levels, all possible combinations of decay paths to the ground state were considered in assigning γ-rays as possible transitions from these levels. This method had previously been used in locating two new unbound states in ^{30}P [Byb95][Wal96]. A second technique exploited the Doppler shifting of the energies of the ^{30}P peaks in the CSGe spectrum relative to their energies in the USGe spectrum of approximately 1 keV per 1000 keV of γ-ray energy. Contaminant γ-rays are produced from different reaction kinematics than ^{30}P γ-rays and thus have different Doppler shifts. Therefore, a comparison of the energy shift of a given peak between the CSGe and USGe spectrum often aided in the assignment of the source of an unassigned γ-ray.

5.3.1 Overlapping Resonances

As previously discussed, it was essential to properly assign all ^{30}P gamma-rays, especially primary decays, as originating from the decay of the particular resonance under study. However, this identification process becomes complicated when a resonance overlaps with a neighboring resonance (or resonances). This overlap occurs when the energy spacing between adjacent resonances is comparable to their experimental widths. The ^{29}Si(p,γ) excitation function shows broad resonances at $E_p = 1.3268$ MeV, $E_p = 1.6393$ MeV, and $E_p = 1.6844$ MeV, which overlap nearby resonances. Gamma-rays from the broad resonance appear in the decay scheme of the narrower resonance.

For γ-rays occurring in both decay schemes, a particular γ-ray from the broad resonance will contribute a portion of its intensity to the intensity of the narrower resonance. The amount of this contribution depends on the Breit-Wigner cross section of the broad

Table 5.7. ^{30}P $\gamma-$ray intensities for the $E_x = 6853.9$ keV resonance.

E_γ (keV)	Observed I_γ (Relative)	Expected I_γ^a (Relative)	E_i (keV)	E_f (keV)
31.7	0.0	0.0	709.02	677.29
565.4	0.0	0.0	2539.03	1973.62
677.3	78.4	76.1	677.29	0.0
709.0	2.95	2.81	709.02	0.0
745.7	0.45	0.35	1454.67	709.02
964.3	0.12	0.09	2937.87	1973.62
991.0	0.17	0.19	3928.9	2937.87
1264.6	0.35	0.23	1973.62	709.02
1454.7	7.83	7.59	1454.67	0.0
1483.2	6.95	6.78	2937.87	1454.67
1830.0	0.0	0.01	2539.03	709.02
1973.6	0.16	0.19	1973.62	0.0
2014.9	0.00	0.06	2723.96	709.02
2228.9	0.76	0.90	2937.87	709.02
2260.6	5.15	4.92	2937.87	677.29
2342.1	0.16	0.14	3019.39	677.29
2351.6	1.97	2.00	6853.9	4502.32
2385.6	4.68	4.70	6853.9	4468.33
2431.5	0.15	0.15	6853.9	4422.4
2474.2	0.13	0.05	3928.9	1454.67
2539.0	0.40	0.37	2539.03	0.0
2724.0	2.33	2.04	2723.96	0.0
2925.0	0.24	0.24	6853.9	3928.9
2937.9	2.81	2.79	2937.87	0.0
3047.6	1.04	1.10	4502.32	1454.67
3713.4	0.0	0.01	4422.4	709.02
3759.3	0.30	0.39	4468.33	709.02
3793.3	0.13	0.08	4502.32	709.02
3834.5	0.14	0.14	6853.9	3019.39
3916.0	15.3	15.3	6853.9	2937.87
4129.9	2.13	2.10	6853.9	2723.96
4314.9	0.38	0.38	6853.9	2539.03
4422.4	0.20	0.14	4422.4	0.0
4468.3	4.68	4.31	4468.33	0.0
4502.3	0.67	0.82	4502.32	0.0
4880.3	0.32	0.32	6853.9	1973.62
6144.9	0.81	0.80	6853.9	709.02
6176.6	71.0	71.0	6853.9	677.29
6853.9	2.82	2.80	6853.9	0.0

[a] For primary transitions, calculated from branching ratios of this work.
For transitions from all other levels, calculated from branching ratios of [Rei85].

resonance at the on-resonance energy of the narrower overlapped resonance. For a single, isolated resonance located at an energy E_r, the Breit-Wigner capture cross section [Bla91] can be expressed as

$$\sigma_{cap} \propto \frac{\Gamma_p \Gamma_\gamma}{[(E_p - E_r)^2 + \frac{\Gamma^2}{4}]}, \tag{5.4}$$

where the total width of the resonance Γ is the sum of the proton width Γ_p and the gamma width Γ_γ.

Since different targets were often used in accumulating the broad resonance and overlapped resonance data, a direct comparison of the intensities for a given gamma-ray in both decay schemes would not yield accurate information regarding the contribution of the broad resonance to the overlapped resonance. Instead, the off-resonance intensity of a particular γ-ray of the overlapped resonance was used to indicate the contribution of the broad resonance to the intensity of that same gamma-ray at the on-resonance energy of the overlapped resonance. Specifically, the ratio of the denominator terms in Equation 5.4 give the relative change of the cross section of the broad resonance from the on-resonance to off-resonance energies of the overlapped resonance. This ratio then was used to correct the intensity of that γ-ray observed at the off-resonance energy to its value at the on-resonance energy. This corrected intensity was then subtracted from the on-resonance intensity to give the contribution from the overlapped resonance itself. The error on this new intensity was calculated using standard error propagation techniques.

Gamma-rays unique to the decay scheme of the broad resonance would often appear in the decay scheme of the overlapped resonance. If the corrected off-resonance intensity of a gamma-ray of the overlapped resonance accounted for all of its on-resonance intensity, then that particular gamma-ray was identified as originating entirely from the broad resonance. In addition, comparison of the ratio of a known ^{30}P gamma-ray unique to the overlapped resonance to a gamma-ray suspected to originate from the broad resonance at the on- and off-resonance energies were made. A difference in these ratios then meant that the suspected gamma-ray was from the broad resonance.

The contaminants at E_p = 1.5095, 1.6675, and 1.7464 MeV shown in Fig. 4.4 and Fig. 4.5 are located at energies overlapped by ^{30}P resonances. In these cases, gamma-

rays from the ^{30}P nuclide were observed in the gamma-ray decay of these contaminant resonances. Off-resonance data were used as described above to determine the source of these observed ^{30}P gamma-rays. For single isolated contaminant resonances, the energies of the on-resonance gamma-rays were simply compared to known ^{30}P gamma-rays. If no matches were found, the contaminant was labelled as not ^{30}P.

5.4 Energy Level and Branching Ratio Measurements

Once the assignments of ^{30}P gamma-rays were complete, their energies were used to calculate the energy of the resonant state as well as the energies of the states populated by the decay of a particular resonance. As shown in Fig. 5.11, each of the 12 states populated in the decay of the $E_x = 6853.9$ keV resonance provide several possible unique paths to the ground state. The energy of each level was calculated as the weighted average of these possible paths to $E_x = 0.0$. The errors on these energies were determined by standard error propagation of the errors on the energies used in the calculation of the weighted average. Table 5.8 lists the energy levels obtained from this work; these energies compare favorably with the energies listed by Endt [End90a]. An energy of $E_x = 6853.9 \pm 0.14$ keV was calculated from the weighted average of these various paths to ground.

The GRAY program was also used to compute the branching ratios for the primary decays from the resonance level. Table 5.9 lists the 12 primary decays from the $E_x = 6853.9$ keV level, four of which were previously not observed [Rei85]. The observation of 6 branching ratios below 1 % demonstrates the high sensitivity of our detector system. The statistical errors on these branching ratios were obtained by standard error propagation of the intensity uncertainties (as listed in Table 5.5) used in a particular branching ratio measurement. The 4 % error in the efficiency also contributed to these errors, since the relative intensities were initially corrected for detector efficiency. Therefore, the total error on an individual branching ratio was computed as this 4 % efficiency error summed in quadrature with the statistical error.

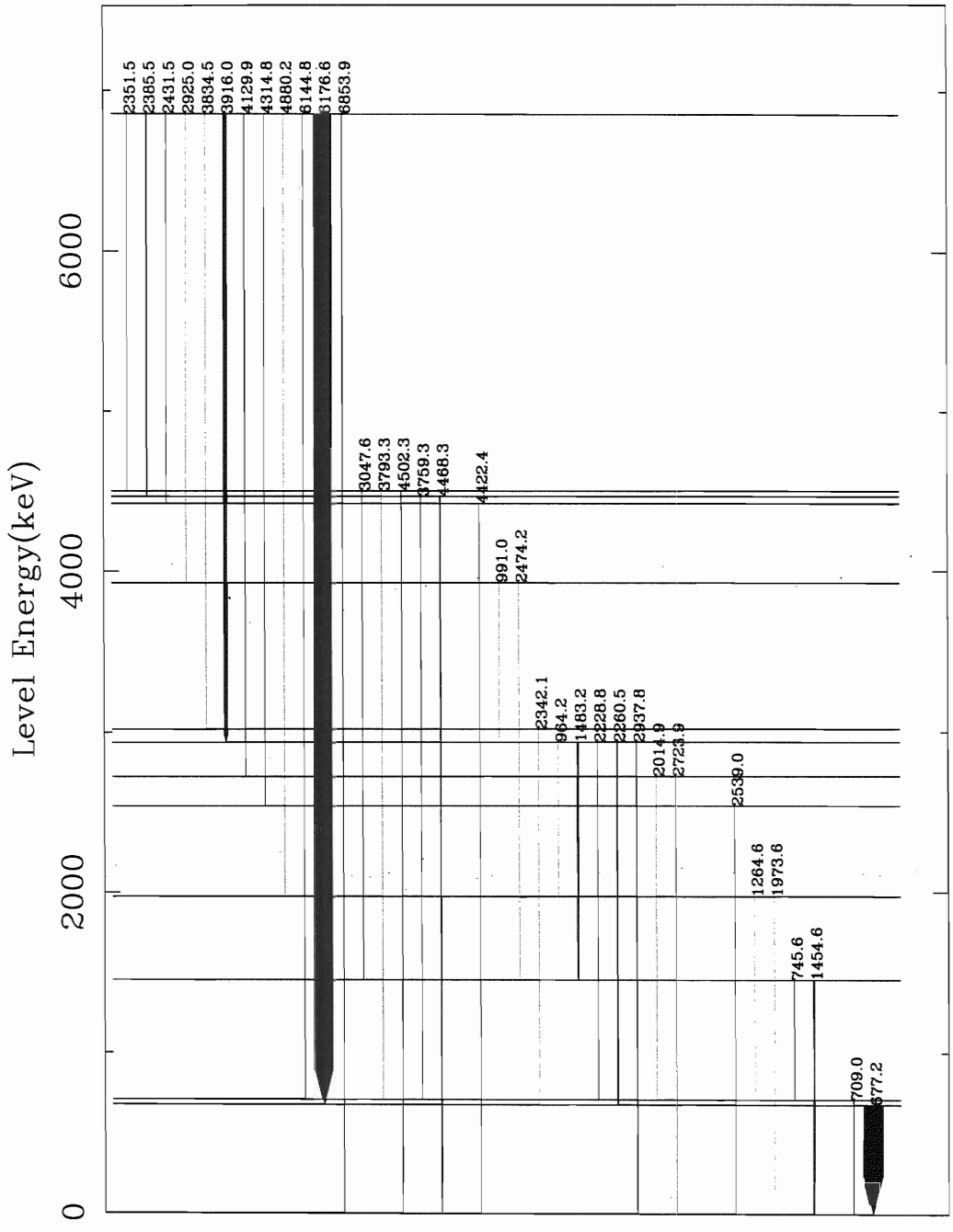

Figure 5.11. Decay scheme for the $E_x = 6853.9$ keV resonance. The width of the arrow indicates the relative strength of the particular transition.

Table 5.8. Energies [a] of levels fed by the $E_x = 6853.9$ keV resonance.

Present Work		Previous Work [b]	
Energy	Error	Energy	Error
0.0		0.0	
677.0	0.2	677.29	0.07
708.7	0.2	709.02	0.06
1454.2	0.2	1454.67	0.07
1973.7	0.2	1973.62	0.11
2538.9	0.4	2539.03	0.11
2724.2	0.4	2723.96	0.10
2937.8	0.2	2937.87	0.06
3019.4	0.5	3019.39	0.11
3929.8	0.2	3928.9	0.3
4422.7	0.4	4422.4	0.3
4468.9	0.3	4468.33	0.07
4503.4	0.3	4502.32	0.12
6853.9	0.1	6853.3 [c]	0.16

[a] Energies and their errors are expressed in keV.

[b] From [End90a].

[c] Based on $S_p = 5594.5 \pm 0.4$ keV from [Aud93].

Table 5.9. Branching ratios for the $E_x = 6853.9$ keV resonance.

	Present Work	Previous Work [a]
E_f (keV)	BR (%)	BR (%)
0.0	2.8 ± 0.2	3.2
677.29	71 ± 3	70
709.02	0.8 ± 0.1	2.3
1973.62	0.32 ± 0.05	–
2539.03	0.38 ± 0.06	0.4
2723.96	2.1 ± 0.1	2.1
2937.87	15.3 ± 0.7	15
3019.39	0.14 ± 0.03	–
3928.9	0.24 ± 0.04	–
4422.4	0.15 ± 0.03	–
4468.33	4.7 ± 0.2	4.9
4502.32	2.0 ± 0.1	2.1

[a] From [Rei85].

5.5 Spin, Parity, and Isospin Assignments

The analysis described in this section contributed to the establishment of a pure level scheme for ^{30}P by determining the possible J, π, and T values for the 17 resonances studied in this work. Selection rules for EM transitions as discussed in Sect. 2.3 were used to restrict the possible J^π values of a particular resonant level. The gamma-ray intensities expressed in Weisskopf units (see Sect. 2.4) of primary transitions were compared to the *recommended upper limits* (RUL's) [End93] to further restrict the possible $J^\pi; T$ values of a particular level. This section discusses the results of these analyses for the 6853.9-keV level.

The first restrictions on possible assignments to the resonant level were obtained using the selection rules. Since the probability for a specific multipolarity to occur markedly decreases with the order L of the EM radiation, only E1, M1, E2, M2, or E3 radiation were considered in this analysis. The primary transitions from the 6853.9-keV level feed to final states of $J^\pi = 0^+, 1^+, 2^+$, or 3^+. Application of the selection rules to these decays for various transition multipolarities limited the possibilities to $J^\pi = 1^+, 1^-, 2^+, 2^-$, or 3^- for this level.

The strength of these primary transitions must first be calculated in Weisskopf units (W.u.) [Wei51] to further restrict the possible assignment of the resonant level. As discussed in the last section, the sum of the gamma-ray intensities from a resonant level are divided among the various decays to lower levels according to the branching ratios for each transition. The intensity of the i^{th} transition is conveniently expressed as a partial width, Γ_γ^i, given by the branching ratio multiplied by the total gamma-ray width of the resonance, Γ_γ. For a specific transition type, 1 W.u. corresponds to a width Γ_W (in eV) of

$$\begin{aligned}
\Gamma_W(\mathrm{M1}) &= 2.072 \times 10^{-2} E_\gamma^3 \\
\Gamma_W(\mathrm{M2}) &= 1.471 \times 10^{-8} A^{2/3} E_\gamma^5 \\
\Gamma_W(\mathrm{E1}) &= 6.474 \times 10^{-2} A^{2/3} E_\gamma^3 \\
\Gamma_W(\mathrm{E2}) &= 4.791 \times 10^{-8} A^{4/3} E_\gamma^5 \\
\Gamma_W(\mathrm{E3}) &= 2.232 \times 10^{-14} A^2 E_\gamma^7.
\end{aligned} \tag{5.5}$$

These widths Γ_W depend on the mass number of the nucleus and the γ-ray energy for a

specific transition (E_γ), with the energy in MeV. The reduced transition strength B (as discussed in Sect. 2.4) in W.u. is then the partial width of a particular transition divided by Γ_W.

If the gamma-ray width, Γ_γ, is unknown (this occurs for four of the resonances studied), then only limits on the reduced transition strengths B were calculated. However, values of the ^{29}Si(p,γ) resonance strength S have been measured (see Table 4.4) for these resonances at $E_p = 1.1111$, 1.0380, 1.4333, and 1.5787 MeV. By convention, the resonance strength S is defined by

$$S = (2J+1)\frac{\Gamma_p\Gamma_\gamma}{\Gamma} \tag{5.6}$$

for resonances with partial widths Γ_p and Γ_γ, total width Γ, and spin J. In addition, if $\Gamma = \Gamma_p + \Gamma_\gamma$, the proton width can be expressed as

$$\Gamma_p = \frac{S\Gamma_\gamma}{(2J+1)\Gamma_\gamma - S}. \tag{5.7}$$

The denominator term in eqn. 5.7 thus determines the lower limit on the γ-ray width as

$$\Gamma_\gamma > \frac{S}{2J+1}. \tag{5.8}$$

This lower limit on the γ-ray width was then used to determine corresponding lower limits on the reduced transition strengths of particular primary transitions for these four resonances.

Endt has compiled [End93] an extensive amount of data on the strengths of γ-ray transitions in light nuclei. The types of transitions in his review were differentiated by their transition character, which classified them according to their EM radiation type and as either isoscalar (IS) or isovector (IV) (i.e., E1 IV, M2 IS, etc.) transitions. A Gaussian distribution of logarithmic reduced transition strengths x was assumed for each type of transition character. The RUL's for each transition character were defined such that the probability of an x exceeding its particular RUL was 0.001 [End88b]. Table 5.10 lists the RUL's for the various transition characters considered in this work. For this analysis, a resonance decayed through a particular transition character as determined by an *assumed* $J^\pi;T$ of the initial resonant state and the known $J^\pi;T$ of the final state. Following the

Table 5.10. Recommended upper limits[a] on B for $A = 21 - 44$ nuclei.

Transition type	RUL (W.u.)
E1 IS	0.002
E1 IV	0.1
E2 IS	100
E2 IV	5
E3 IS	50
M1 IS	0.05
M1 IV	5
M2 IS	0.2
M2 IV	5

[a] From [End93].

recommendation of Endt, a transition of a specific character was extremely unlikely if its reduced transition strength B exceeded twice that of its RUL. Therefore, an assumed $J^\pi; T$ possibility for a resonance was eliminated provided the B of one of the primary decays of the various transition characters associated with this assumption exceeded twice its RUL.

Transitions composed of a mixture of two different types of EM radiation, M(L) and E($L+1$), were also considered in this analysis. For these mixed transitions, mixing ratios are defined (with the phase convention of Rose and Brink [Ros67]) as

$$\delta_{E2/M1} \equiv \sqrt{\frac{\Gamma_{E2}}{\Gamma_{M1}}} \tag{5.9}$$

and

$$\delta_{E3/M2} \equiv \sqrt{\frac{\Gamma_{E3}}{\Gamma_{M2}}}. \tag{5.10}$$

If the mixing ratio is known, the partial width of a transition is divided into its two components and a B for each component calculated. The specific values of the reduced transition strengths for each component were then used to compare to their respective RUL's.

However, for an unknown mixing ratio, only limits on the reduced transition strengths can be determined. In these cases, a maximum value of B was calculated for each component by assuming that each was a pure transition. This assumption established an upper limit on the reduced transition strengths, since the mixing of components reduces

the value of B. This limit was then used to calculate the possible values of the mixing ratio that would allow a transition to occur. For example, assume that the 6853.9 keV level is $1^+;0$. Then it possibly decays to the $E_x = 2938$ keV $(2^+;1)$ level through a M1/E2 mixed transition with $\delta_{E2/M1}$ unknown. If the transition is assumed as pure M1, B(M1)= 0.066, which is less than twice the M1 IV RUL. But, if the same transition is assumed as pure E2, B(E2)= 20.1, which exceeds twice the E2 IV RUL. The pure E2 assumption, therefore, gives $|\delta_{E2/M1}| \leq 0.996$ for the transition to be allowed. Knowledge of the mixing ratio for this transition would then aid in assigning the $1^+;0$ assignment as possible or not.

As discussed above, five J^π possibilities were considered for the 6853.9-keV level, which gave 10 possibilities for possible $J^\pi;T$ assignments to this level. The 12 primary decays give 120 different transitions that were considered in restricting these 10 possibilities. Table 5.11 summarizes the results of the RUL analysis for transitions whose reduced transition strengths exceeded twice their associated RULs and thus were eliminated. As discussed above, for mixed transitions with unknown mixing ratios, both of the B's computed by assuming a *pure* transition are listed in this table. The results of this RUL analysis gave $1^+;0$, $1^+;1$, and $2^+;1$ as remaining possibilities for the 6853.9-keV level. Nelson [Nel83a] assigned positive parity, based on an $\ell = 0$ measurement for this level. In addition, Endt [End90a] agrees with Nelson's assignment of $J = 0$ or $J = 1$ for this level. This previous research combined with the results of this work then give a final assignment of 1^+ for this level. An upper limit of 0.651 on the mixing ratio of the primary decay to the $E_x = 4502$ keV $(1^+;1)$ level might help eliminate the $1^+;1$ possibility. This result and the mixing ratio limit of the transition to the 2938-keV level discussed above suggest that the isospin of this level could be determined by an angular distribution study of the primary transitions to the 2938-keV and 4502-keV levels.

5.6 Summary of Results

There are currently 159 known ^{30}P energy levels from the ground state to $E_x = 8820$ keV. Fig. 5.12 shows for each level with excitation energy E_x, the number of levels lower in energy N(E). As expected, the level density is a monotonically increasing function of

Table 5.11. Summary of RUL analysis for the $E_x = 6853.9$ keV resonance.

$J^\pi;T$ Assignment	E_f (keV)	$J^\pi;T$ (Final)	Transition Type	B (W.u.)	RUL (W.u.)
$1^-;0$ §	2539	$3^+;0$	M2/E3 IS	9.66/3670	0.2/50
	3929	$3^+;0$	M2/E3 IS	42.6/35,200	0.2/50
$1^-;1$	3929	$3^+;0$	M2/E3 IV	42.6/35,200	5/‡
$2^+;0$	4468	$0^+;1$	E2 IV	44.1	5
$2^-;0$	677	$0^+;1$	M2 IV	180	5
	4468	$0^+;1$	M2 IV	1390	5
$2^-;1$	677	$0^+;1$	M2 IS	180	0.2
	4468	$0^+;1$	M2 IS	1390	0.2
$3^-;0$ §	677	$0^+;1$	E3 IV	23,800	‡
	4468	$0^+;1$	E3 IV	†	‡
$3^-;1$ §	677	$0^+;1$	E3 IS	23,800	50
	4468	$0^+;1$	E3 IS	†	50

§ B of more than two transitions exceed twice their associated RUL.

† $B > 10^7$ W.u..

‡ No RUL given in [End93], but $B \doteq 100$ E3 IV upper limit used in this work.

energy. The general shape and behavior of this level density plot suggests that most of the existing energy levels in this energy range are known. Therefore, the goal of a complete level scheme probably has been accomplished.

A summary of the current status of the $J^\pi;T$ assignments for each resonant level studied in this work is given below. The summary for the $E_x = 6853.9$-keV level is excluded here, since Sect. 5.5 gives a complete summary for that level. For each resonant level, Table 5.12 compares the $J^\pi;T$ assignments from previous research and from this work. A detailed listing of the previous experimental work on the ^{30}P nucleus is given by Frankle [Fra91]. All energies in this summary are expressed in keV; the proton resonance energies, E_p, are obtained from Frankle et al. [Fra92].

As discussed in Sect. 5.5, the $J^\pi;T$ assignments to a particular level resulted from two separate restrictions. The first restriction consisted of limiting the primary transitions to 5 EM transition types, E1, M1, E2, M2, and E3 and invoking the selection rules for those transitions. The RUL analysis then compared the strengths of these remaining transitions

to their respective RUL's to further restrict these possibilities. These possibilities were then compared with the results of previous researchers to make a final J^{π};T assignment to a particular level.

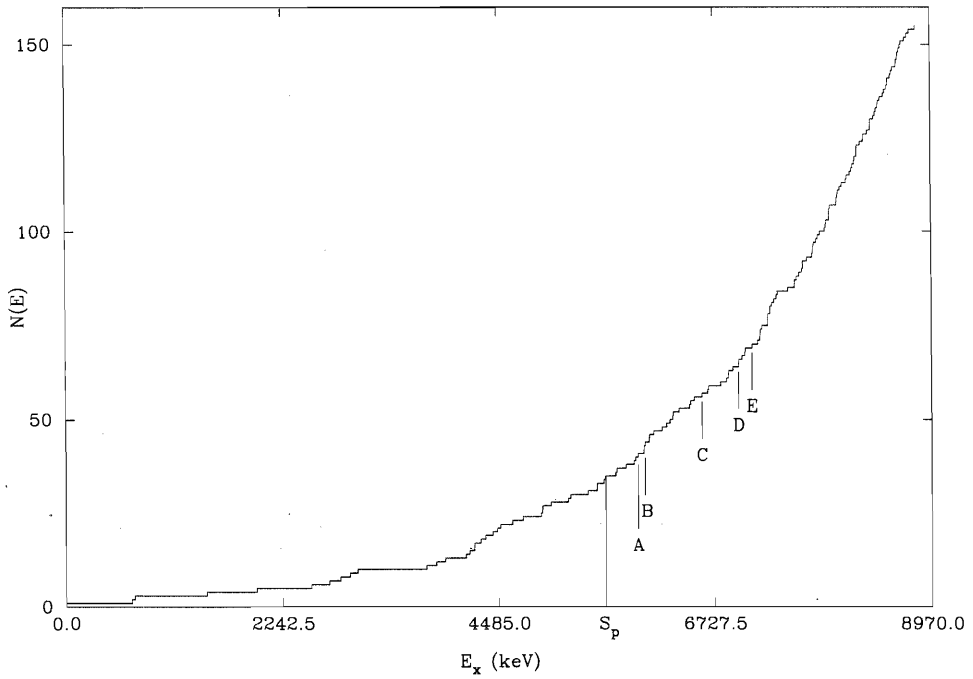

Figure 5.12. Plot of the number of ^{30}P levels N(E) below a given energy as a function of excitation energy E_x. The new levels (located near the proton separation energy S_p = 5594.5 keV) of Bybee [Byb95] and Wallace [Wal96] are denoted A and B, respectively. The levels corresponding to the three new resonances found in this work are denoted by C, D, and E.

5.6.1 $E_p = 1038.0$ $E_x = 6597.7$

As discussed in Chap. 4, this new resonance was identified as originating from the ^{29}Si(p,γ) reaction. The decay scheme of this new level is shown in Fig. 5.13. Limiting the primary transitions to E1, M1, E2, M2, and E3 gave $(2-5^{+})$ J^{π} possibilities. The RUL analysis limited this set to $(3-5^{+})$. S was measured to be 0.03 eV (see Sect. 4.4) for this resonance, but the gamma-ray width, Γ_{γ}, and the proton width, Γ_p, are unknown.

Table 5.12. Summary of results.

E_x (keV)	Previous Work	Present Work	Final Assignment
6597.7 ± 0.2	–	$(3-5^+)$ [a]	$(3-5^+)$
6667.8 ± 0.1	$(2^-, 3^+)$	$(2^-, 3^+)$	$(2^-, 3^+)$
6853.9 ± 0.1	$(0,1)^+$	1^+ $2^+;1$	1^+
6873.4 ± 0.1	3^+	$(2^-, 3)$	3^+
6876.5 ± 0.2	2^-	$(1^+, 2, 3^+)$	2^-
6921.0 ± 0.2	$1^-;0$	$1;0$	$1^-;0$
6978.3 ± 0.2	–	$(3^+, 4^+)$ $(3^-, 4^-);1$	$(3^+, 4^+)$ $(3^-, 4^-);1$
7014.9 ± 0.1	$2^-;0$	$2;0$ $(2^+, 3^+);1$	$2^-;0$
7045.0 ± 0.2	$(2-4)^-$	$(2-4^-);0$ $(3, 4^-);1$	$(2-4)^-;0$ $(3,4)^-;1$
7049.4 ± 0.2	$4^-;1$	$(3,4);1$	$4^-;1$
7119.1 ± 0.2	–	$(1^+, 2, 3)$ $1^-;1$	$(1^+, 2, 3)$ $1^-;1$
7177 ± 2	1^-	$(1, 2^+)$	1^-
7203.0 ± 0.2	$2(1)^+$	$(1^+, 2^+)$ $2^-;0$ $3^-;1$	$2(1)^+$
7207.5 ± 0.2	$(0,1)^+;1$	$(2, 3^+);0$ $(0-2);1$	$(0,1)^+;1$
7223.3 ± 0.2	$2^-;1$	$(2, 3^+);1$	$2^-;1$
7282.0 ± 0.2	$3^-;0$	$(1^+, 2^+, 3)$ $2^-;0$ $4^+;1$	3
7283.4 ± 0.1	$2^+;1$	$2^+;1$	$2^+;1$

[a] $J^\pi;T$ listed according to the following convention:

$(3-5^+)$ J^π=$3^\pm, 4^\pm, 5^+$

$0^+;1$ definite spin, parity and isospin.

$1(0)^+$ definite parity, preferred spin outside the parentheses.

Values with isospin not shown explicitly have both $T=0$ and $T=1$ possibilities.

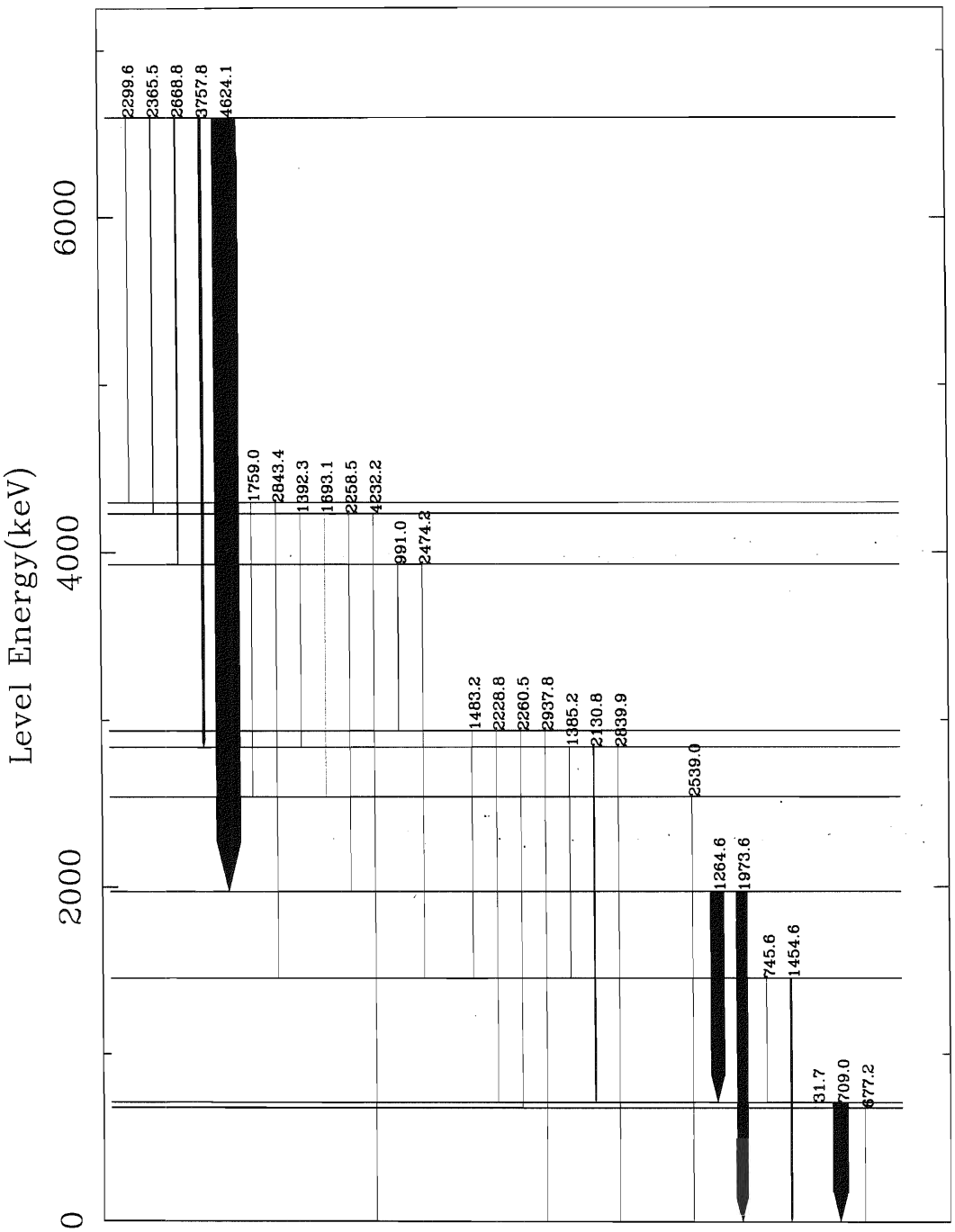

Figure 5.13. Decay scheme for the $E_x = 6597.7$ keV resonance.

5.6.2 $E_p = 1111.1$ $E_x = 6667.8$

The gamma-ray width of this level is not known, but $S = 0.18$ eV. Limiting the transitions to E1, M1, E2, M2, and E3 gave $(1^+ - 4^-)$ J^π possibilities. The RUL analysis further restricted these possibilities to $(2^-, 3^+)$. This RUL analysis result agrees with the decay studies of Reinecke et al. [Rei85] on this level. Final assignment is $(2^-, 3^+)$ for this level.

5.6.3 $E_p = 1323.8$ $E_x = 6873.4$

Limiting the transitions to E1, M1, E2, M2, and E3 gave $(1^+ - 4^-)$ J^π possibilities for this level. The RUL analysis restricted this set to $(2^-, 3)$. Frankle based a 3^+ assignment on an $\ell = 4$ measurement of Ramstein et al. [Ram81] for either this level or the level at $E_x = 6876.5$ keV (Ramstein et al. [Ram81] could not resolve the two levels). Since the J^π of the 6876.5 level is well established as 2^-, Ramstein et al. [Ram81] then actually measured this level at $E_x = 6873.4$ keV as $\ell = 4$, which restricts J^π to 3^+. This assignment is consistent with the present work; therefore 3^+ is assigned to this level.

5.6.4 $E_p = 1326.8$ $E_x = 6876.5$

Limiting the transitions to E1, M1, E2, M2, and E3 gave $(0^- - 4^-)$ J^π possibilities for this level. The RUL analysis further limited these possibilities to $(1^+, 2, 3^+)$. The results of this RUL analysis are identical with that of Bybee [Byb95]. Since an assignment of 2^- is well established by previous researchers, 2^- is assigned for this level.

5.6.5 $E_p = 1373.7$ $E_x = 6921.0$

Limiting the transitions to E1, M1, E2, M2, and E3 gave $(1 - 3^-)$ J^π for this resonance. The RUL analysis further restricted these possibilities to $1;0$. Previous researchers are in agreement with a 1^- assignment for this level. $T = 1$ is eliminated as a possibility for this level based on the strength of the isoscalar decay to the $0^+;1$ level at $E_x = 4468$ keV. Therefore $1^-;0$ is assigned to this level.

5.6.6 $E_p = 1433.3$ $E_x = 6978.3$

As discussed in Chap. 4, this new resonance was identified as originating from the ^{29}Si(p,γ) reaction. The decay scheme of this new level is shown in Fig. 5.14. The γ-ray width and proton width are not known, but $S = 0.03$ eV. Limiting the primary transitions to E1, M1, E2, M2, and E3 gave $(2^- - 5^-)$ J^π-values. The RUL analysis restricted these values to $(3^+, 4^+)$ and $(3^-, 4^-)$; 1. Ramstein et al. [Ram81] measured $\ell = 6$ for a level at 6981 ± 5 keV, which may be this level or a separate level. The $\ell = 6$ measurement restricts J^π to $(5 - 7)^+$, which is inconsistent with the RUL analysis of this work. Assuming $\ell = 6$ is correct, this inconsistency in the resulting possible J^π values for both levels suggests that these two levels at $E_x = 6978$ and $E_x = 6981$ keV are different.

5.6.7 $E_p = 1470.9$ $E_x = 7014.9$

Limiting the transitions to E1, M1, E2, M2, and E3 gave $(1 - 4^-)$ J^π possibilities for this level. The RUL analysis restricted these possibilities to 2; 0 and $(2^+, 3^+)$; 1. Since 2^- is well established from previous research, 2^-; 0 is assigned to this level.

5.6.8 $E_p = 1502.3$ $E_x = 7045.0$

Limiting the transitions to E1, M1, E2, M2, and E3 gave $(1 - 5^+)$ J^π possibilities for this level. The RUL analysis restricted these possibilities to $(2 - 4^-)$; 0 and $(3, 4^-)$; 1. The 4-;1 is unlikely, but possible due to a strength of $B = 0.094$ for the M1 IS transition to the 3^-; 1 level at $E_x = 6095$ keV. This strength is less than a factor of 2 greater than the RUL = 0.05 for this transition. For the 3^-; 1 possibility, an assumption of either a pure E2 or a pure M1 primary transition to the 6095-keV level, causes both B(E2) and B(M1) to exceed their respective RUL's by more than a factor of 2. However, the 3^-; 1 is not eliminated due to the possibility $0.40 \leq \delta_{E2/M1} \leq 0.71$ for this mixed M1/E2 transition to the 6095-keV level, which causes both B(M1) and B(E2) not to exceed their respective RUL's by a factor of 2. Nelson established $(2 - 4)^-$ for this level, so the final assignment is $(2 - 4)^-$; 0 and $(3, 4)^-$; 1. An angular distribution study of the transition to the $E_x = 6095$ keV level may further restrict the remaining possible assignments.

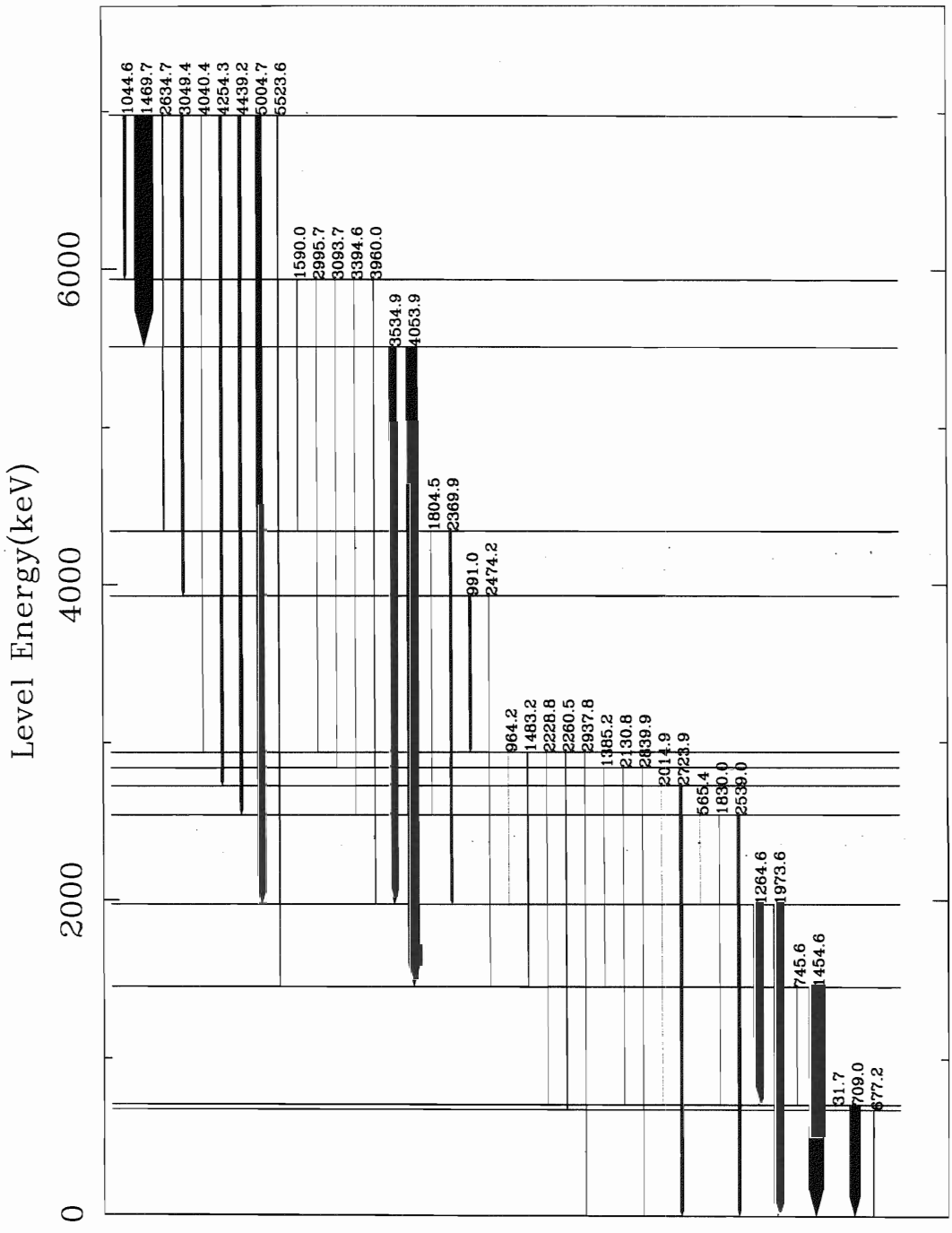

Figure 5.14. Decay scheme for the $E_x = 6978.3$ keV resonance.

5.6.9 $E_p = 1506.0$ $E_x = 7049.4$

Limiting the transitions to E1, M1, E2, M2, and E3 gave $(1^+ - 5^-)$ J^π possibilities for this level. The RUL analysis restricted these possibilities to $(3, 4)$; 1. 4^- is well established by previous research. $T = 1$ is established from the isoscalar primary decays to the $E_x = 4232$ keV $(4^-; 0)$ and $E_x = 4926$ keV $(3^-; 0)$ levels and from this state being the analog of the corresponding state in ^{30}Si [End90a]. Therefore $4^-; 1$ is assigned to this level.

5.6.10 $E_p = 1.5787$ $E_x = 7119.1$

As discussed in Chap. 4, this new resonance was identified as originating from the ^{29}Si(p,γ) reaction. Ramstein et al. [Ram81] also listed a level at 7119 $\pm$ 5 keV, which is probably this level. The decay scheme for this level is shown in Fig. 5.15. The gamma-ray and proton widths are not known, but $S = 0.06$ eV. Limiting the transitions to E1, M1, E2, M2, and E3 gave $(1 - 4^-)$ J^π possibilities for this level. The RUL analysis further restricted these possibilities to $(1^+, 2, 3)$ and $1^-; 1$.

5.6.11 $E_p = 1639.3$ $E_x = 7177$

Limiting the transitions to E1, M1, E2, M2, and E3 gave $(1 - 3^-)$ J^π possibilities for this level. The RUL analysis further restricted this set to $(1, 2^+)$. 1^- is well established by previous research. The $T = 0$ possibilities are unlikely, but still possible, since the $B = 0.0037$ strength of the E1 IS decay to the $1^+; 0$ level at $E_x = 709$ keV, does not quite exceed the RUL $= 0.002$ by a factor of 2. The final assignment is thus 1^- for this level.

5.6.12 $E_p = 1663.9$ $E_x = 7203.0$

Limiting the transitions to E1, M1, E2, M2, and E3 gave $(1 - 3^-)$ J^π possibilities for this level. The RUL analysis further restricted these possibilities to $(1^+, 2^+)$, $2^-; 0$ and $3^-; 1$. Nelson [Nel83b] and Frankle [Fra91] assigned $2(1)^+$ for this level, so the $2^+; 0$ or $2^+; 1$ assignment are the most likely possibilities. The final assignment assignment for this level is $2(1)^+$. An angular distribution study of the primary decay to the $2^+; 1$ level at

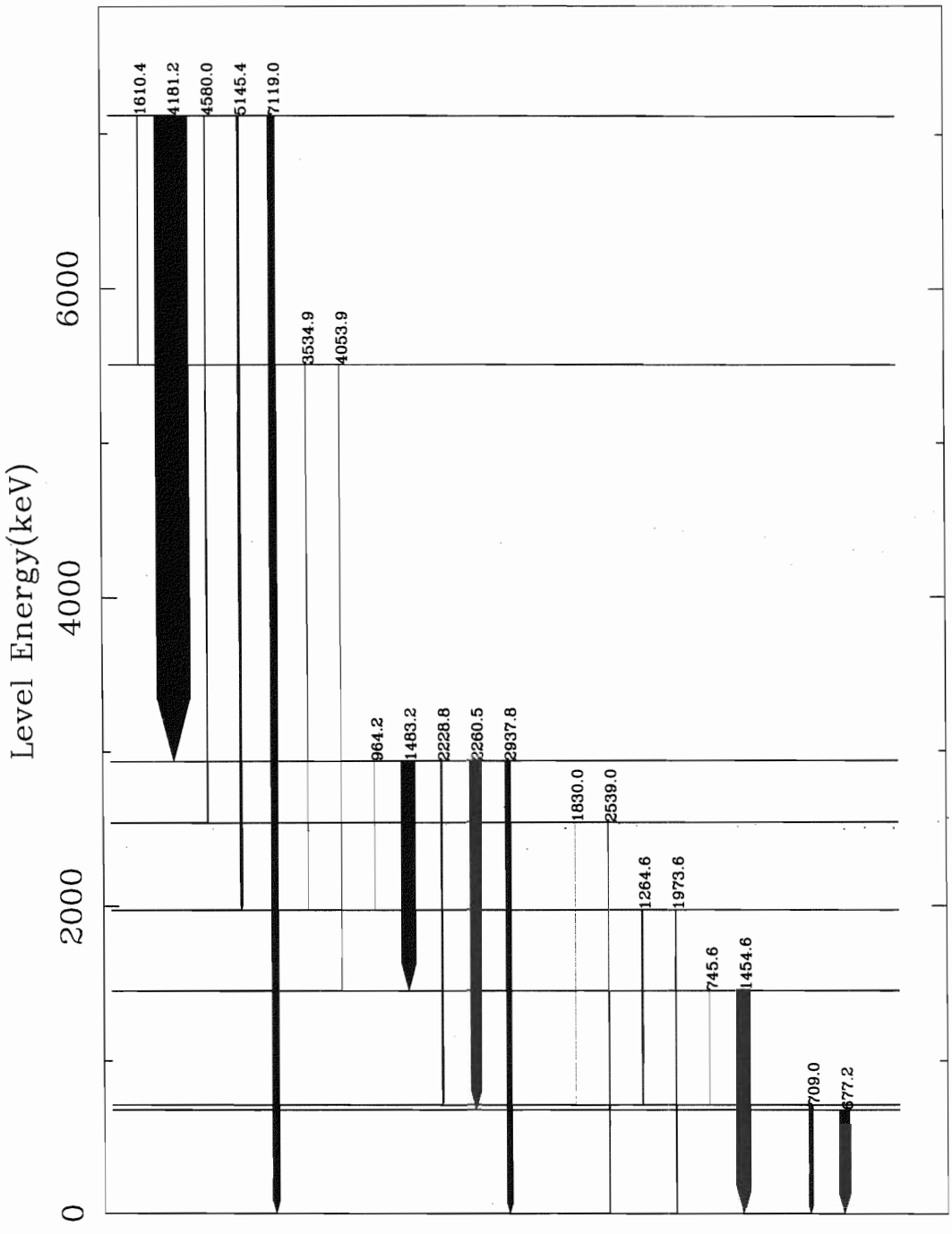

Figure 5.15. Decay scheme for the $E_x = 7119.1$ keV resonance.

$E_x = 2938$ keV should provide information helpful in making a definite assignment for this level and for the level at $E_x = 6006$ keV.

5.6.13 $E_p = 1668.5$ $E_x = 7207.5$

Limiting the transitions to E1, M1, E2, M2, and E3 gave $(0-3)$ J^π possibilities for this level. The RUL analysis restricted these possibilities to $(2, 3^+); 0$ and $(0-2); 1$. The $2^+; 0$ and $2^-; 0$ mixed M1/E2 transitions to the $1; 0$ level at $E_x = 5506$ keV are allowed for $0.67 \leq \delta_{E2/M1} \leq 2.51$.

The results of previous researchers are in disagreement for the J^π assignment of this level. Nelson and Ramstein et al. [Ram81] measured 0^+ for this level. Frankle [Fra91] and Reinecke et al. [Rei85] assigned 1^+ for this level based on the results of angular distribution measurements not allowing $J = 0$ for this level. However, an angular distribution study by LaBonte [LaB95] showed this result was unphysical. An assignment of $(0, 1)^+$ establishes $T = 1$ for this level based on the strength of the decay to the $E_x = 3019$ keV $(1^+; 0)$ and $E_x = 5506$ keV $(1; 0)$ levels. The final assignment is $(0, 1)^+; 1$ for this level. An angular distribution study of the decay to the levels at $E_x = 3019$ keV and $E_x = 5506$ keV should provide information helpful in making a definite assignment for this level.

5.6.14 $E_p = 1684.4$ $E_x = 7223.3$

Limiting the transitions to E1, M1, E2, M2, and E3 gave $(1-4^-)$ J^π possibilities for this level. The RUL analysis further restricted these possibilities to $(2, 3^+); 1$. This is consistent with the results of the analysis by Shriner [Shr95b] of the angular distribution measurements [LaB95] for this resonance. A $T = 1$ assignment is based on the strength of the transition to the $2^-; 0$ level at $E_x = 4144$ keV. This isospin assignment is also consistent with this level being the analog of a corresponding state in ^{30}Si [End90a]. 2^- is well established by previous research. Therefore the final assignment is $2^-; 1$.

5.6.15 $E_p = 1745.0$ $E_x = 7282.0$

Limiting the transitions to E1, M1, E2, M2, and E3 gave $(0^- - 5^-)$ J^π possibilities for this level. The RUL analysis further restricted these possibilities to $(1^+, 2^+, 3)$, $2^-; 0$ and $4^+; 1$. The negative parity assignment of Endt [End90a] is presumably erroneous [Fra91]. This assignment was based on an $\ell = 3$ measurement listed in an earlier compilation [End78]. However, Endt [End78] actually lists $\ell = 3$ for the two levels at $E_p = 1769.8$ keV and 1771.5 keV. From the results of Harris et al. [Har69], $J = 3$ is assigned to this level. An angular distribution study of the decay to the $(2^+; 1)$ levels at $E_x = 2938$ keV and $E_x = 4183$ keV should provide information helpful in restricting the possible assignments for this level.

5.6.16 $E_p = 1746.4$

This level was first observed by Frankle [Fra91] and listed as originating from the ^{29}Si(p,γ) reaction. However, the results of this work suggest that this level originates instead from the ^{13}C(p,γ) reaction at $E_p = 1747.6 \pm 0.9$ keV [Ajz91]. All primary decays from this level were also observed in the neighboring $E_x = 7282.0$ keV and $E_x = 7283.4$ keV levels. The 12 observed $\gamma-$rays from the $E_x = 9172.5$ keV level in ^{14}N decayed according to the known decay scheme [Ajz91] for this ^{14}N resonance. The areas of this level and the 7283.4 level (listed in Table 4.1) relative to each other are different from the relative areas of these two resonances as measured by Frankle [Fra91]. If this level originated from the ^{30}P nucleus, the relative areas of these two resonances should be the same in this work and in the work of Frankle [Fra91]. This difference suggests a different amount of the ^{13}C contaminant on the targets used for this work from the amount of this contaminant on the targets used by Frankle [Fra91]. Therefore, for the reasons discussed above, this level is assigned to ^{14}N.

5.6.17 $E_p = 1747.2$ $E_x = 7283.4$

Limiting the transitions to E1, M1, E2, M2, and E3 gave $(1-3^-)$ J^π possibilities for this level. The RUL analysis further restricted these possibilities to $2^+; 1$. 2^+ is well established

from previous research. The existence of a possible analog state in ^{30}Si [End90a] for this level is consistent with the $T = 1$ result of the RUL analysis. $2^+;1$ is assigned to this level. An angular distribution measurement of the primary transitions to the $E_x = 5206$ keV (3^+) level would help uniquely determine the isospin of the 5206-keV level.

Chapter 6

Summary

The research presented in this dissertation was primarily motivated by the interesting results of a study of the fluctuation properties of the ^{26}Al nuclide. These results indicated the need for tests of the Gaussian Orthogonal Ensemble (GOE) of Random Matrix Theory in additional nuclei. The nuclide ^{30}P seemed the most promising candidate. Empirical tests of the GOE place strict purity and completeness requirements on the spectroscopic data used to perform these tests. Therefore, there is a major effort at the High Resolution Laboratory (HRL) to establish a pure and complete level scheme of ^{30}P for $E_x < 8820$ keV. Upon completion of this effort, statistical tests will be performed on this nuclide to establish further the range of applicability of the GOE.

Excitation functions were obtained using the high-resolution proton beam at the HRL in the ^{29}Si(p,p), ^{29}Si(p,γ), and ^{29}Si(p,p$_1\gamma$) reactions in the proton energy interval $E_p = 1.0 - 2.0$ MeV. Three new resonances were observed in the ^{29}Si(p,γ) and ^{29}Si(p,p$_1\gamma$) reactions at $E_p = 1.0380$, 1.4333, and 1.5787 MeV. Absolute strengths were measured for 21 ^{29}Si(p,γ) resonances over this proton energy interval. These measurements, along with those of Frankle et al. [Fra92], represent a major step toward the complete determination of the ^{30}P level scheme.

A Compton-suppressed gamma-ray detection system equipped with HPGe detectors was used to collect gamma-ray decay data for 17 resonances from $E_x = 6597.7$ to 7283.3 keV. The combination of a high-resolution proton beam and a high-resolution γ-ray de-

tection system maximized the likelihood of resolving close-lying levels and observing weak γ-ray transitions. Extensive energy and efficiency gamma-ray calibrations were performed to ensure accurate construction of a level scheme as well as measurements of E_x and branching ratios for each resonance. A total of 33 states (30 of them bound states) were populated by the 153 primary decays of these 17 resonances. Selection rules for the primary gamma-ray transitions restricted the possible J, π, and T quantum numbers for each resonance. A total of 2938 reduced transition strengths were measured from the various assumed $J^\pi;T$ possibilities of the resonant levels. The measured reduced transition strengths for a particular primary transition were compared with their respective recommended upper limits [End93] for a particular decay type to further constrain the $J^\pi;T$ assignments of a resonant level. This set of quantum numbers was then combined with the results of previous research to make a final $J^\pi;T$ assignment for a given resonance. Of these 17 resonances, 10 were assigned an unambiguous J, 12 an unambiguous parity, and 6 an unambiguous T. For five resonances previous definite assignments were confirmed by the present study.

The results provided a major step forward toward the goal of a pure and complete level scheme for ^{30}P. The results of the high-resolution measurements of this work place the current spectroscopic knowledge of the ^{30}P nucleus on a much firmer foundation. In addition, the present results indicate the transitions for which angular distribution measurements will provide crucial additional information.

Appendix A

Results of Branching Ratio Measurements

This appendix summarizes the branching ratio measurements for the 17 ^{29}Si(p,γ) resonances studied in this work. For the 14 resonances previously studied, the results of the branching ratios from Reinecke et al. [Rei85] are also listed. The majority of the branching ratios measured in this work are in agreement with Reinecke et al. [Rei85], although most tables have newly discovered weak branches due to the higher sensitivity of the present measurements. The energies of the majority of the final states for primary decays are taken from Endt [End90a]. The energies of the new levels at $E_x = 5933.64$ and 6006.07 keV are taken from Bybee [Byb95] and Wallace [Wal96], respectively.

The branching ratios for the $E_x = 7223.3$ keV resonance have been modified as a result of angular distribution measurements [LaB95]. The angular distribution for an isolated resonance may be expressed as

$$W(\theta) = A_0 + \sum_{L=1}^{k} A_{2L} P_{2L}(cos\theta), \tag{A.1}$$

where $P_{2L}(cos\theta)$ are Legendre Polynomials and θ is the angle between the incident proton beam and the CSGe detector axis. The angle of $\theta = 55°$ used for the CSGe detector in these experiments is a minimum of the $P_2(cos\theta)$ term, which minimizes but does not eliminate the effect of the angular distribution on the intensities of the primary γ-rays. A

comparison of the fit (to the angular distribution data) at 55° to the extracted value of the A_0 term in Equation A.1 was used to correct [Shr95a] the intensities of the appropriate primary transitions for angular distribution effects. Of the angular distributions measured currently, these intensity corrections have been less than 10 %.

Table A.1. Branching ratios for the $E_x = 6597.7$ keV resonance.

	Present Work
E_f (keV)	BR (%)
1973.62	80 ± 5
2839.9	10 ± 1
3928.9	4.7 ± 0.6
4232.2	2.6 ± 0.5
4298.1	2.1 ± 0.5

Table A.2. Branching ratios for the $E_x = 6667.8$ keV resonance.

E_f (keV)	Present Work BR (%)	Previous Work BR (%)
1454.67	0.5 ± 0.1	–
1973.62	2.1 ± 0.3	2.1
2723.96	3.5 ± 0.3	3.7
2839.9	0.6 ± 0.1	0.8
2937.87	52 ± 3	54
3019.39	0.2 ± 0.1	0.3
3733.9	6.5 ± 0.9	5.2
3835.9	1.3 ± 0.2	1.7
4143.67	7.0 ± 0.5	6.7
4182.65	19 ± 1	21
4232.2	1.6 ± 0.2	–
4626.55	1.6 ± 0.2	1.6
5508.6	0.7 ± 0.2	–
5576.9	2.9 ± 0.3	2.9

Table A.3. Branching ratios for the $E_x = 6853.9$ keV resonance.

E_f (keV)	Present Work BR (%)	Previous Work BR (%)
0.0	2.8 ± 0.2	3.2
677.29	71 ± 3	70
709.02	0.8 ± 0.1	2.3
1973.62	0.32 ± 0.05	–
2539.03	0.38 ± 0.06	0.4
2723.96	2.1 ± 0.1	2.1
2937.87	15.3 ± 0.7	15
3019.39	0.14 ± 0.03	–
3928.9	0.24 ± 0.04	–
4422.4	0.15 ± 0.03	–
4468.33	4.7 ± 0.2	4.9
4502.32	2.0 ± 0.1	2.1

Table A.4. Branching ratios for the $E_x = 6873.4$ keV resonance.

E_f (keV)	Present Work BR (%)	Previous Work BR (%)
709.02	–	0.6
1454.67	37 ± 2	41
1973.62	13.8 ± 0.7	12
2723.96	7.5 ± 0.4	8.7
2839.9	2.2 ± 0.2	1.7
2937.87	29 ± 1	28
3928.9	1.2 ± 0.1	0.8
4143.67	1.5 ± 0.1	0.8
4182.65	4.8 ± 0.3	4.7
4232.2	1.7 ± 0.1	1.7
5508.6	1.8 ± 0.1	–

Table A.5. Branching ratios for the $E_x = 6876.5$ keV resonance.

E_f (keV)	Present Work BR (%)	Previous Work BR (%)
0.0	75 ± 3	83
709.02	2.4 ± 0.2	2.1
1454.67	7.2 ± 0.5	4.0
2723.96	4.0 ± 0.3	2.8
2839.9	2.3 ± 0.2	2.1
2937.87	2.4 ± 0.2	–
3019.39	4.8 ± 0.3	4.0
4143.67	0.9 ± 0.1	1.2
4182.65	1.2 ± 0.1	0.8

Table A.6. Branching ratios for the $E_x = 6921.0$ keV resonance.

E_f (keV)	Present Work BR (%)	Previous Work BR (%)
0.0	8 ± 1	4.0
677.29	63 ± 5	70
1454.67	9 ± 1	7.5
2723.96	0.7 ± 0.2	0.6
2937.87	1.3 ± 0.3	0.7
3835.9	0.5 ± 0.1	0.6
4143.67	1.5 ± 0.2	1.3
4468.33	13 ± 1	13
4502.32	2.7 ± 0.3	2.3

Table A.7. Branching ratios for the $E_x = 6978.3$ keV resonance.

E_f (keV)	Present Work BR (%)
1454.67	3.8 ± 0.9
1973.62	15 ± 2
2539.03	8 ± 1
2723.96	8 ± 1
2937.87	1.5 ± 0.5
3928.9	7.6 ± 0.9
4343.6	3.8 ± 0.6
5508.6	46 ± 3
5933.64 [a]	7.1 ± 0.8

[a] From [Byb95].

Table A.8. Branching ratios for the $E_x = 7014.9$ keV resonance.

E_f (keV)	Present Work BR (%)	Previous Work BR (%)
0.0	30 ± 1	34
709.02	10.5 ± 0.6	12
1973.62	0.35 ± 0.06	–
2539.03	3.9 ± 0.2	3.3
2723.96	0.69 ± 0.09	0.6
3019.39	10.2 ± 0.5	10
3733.9	1.7 ± 0.1	1.0
4143.67	11.4 ± 0.5	10
4182.65	2.0 ± 0.1	1.4
4502.32	26 ± 1	25
4626.55	3.0 ± 0.2	2.7

Table A.9. Branching ratios for the $E_x = 7045.0$ keV resonance.

E_f (keV)	Present Work BR (%)	Previous Work BR (%)
1973.62	21 ± 1	29
2539.03	34 ± 2	45
2839.9	5.0 ± 0.5	5
4143.67	18 ± 1	21
5508.6	3.0 ± 0.3	–
6006.07 [a]	4.2 ± 0.4	–
6094.60	14.4 ± 0.9	–

[a] From [Wal96].

Table A.10. Branching ratios for the $E_x = 7049.4$ keV resonance.

E_f (keV)	Present Work BR (%)	Previous Work BR (%)
1454.67	0.12 ± 0.02	–
1973.62	7.5 ± 0.3	8.0
2539.03	3.7 ± 0.2	3.8
2839.9	3.7 ± 0.2	4.0
3928.9	1.32 ± 0.07	1.2
4232.2	52 ± 2	52
4626.55	15.3 ± 0.6	15
4926.4	16.7 ± 0.7	16

Table A.11. Branching ratios for the $E_x = 7119.1$ keV resonance.

E_f (keV)	Present Work BR (%)
0.0	16 ± 2
1973.62	6.4 ± 0.8
2539.03	2.9 ± 0.5
2937.87	72 ± 4
5508.6	2.6 ± 0.3

Table A.12. Branching ratios for the $E_x = 7177$ keV resonance.

E_f (keV)	Present Work BR (%)	Previous Work BR (%)
0.0	28 ± 2	29
677.29	10.9 ± 0.8	11
709.02	47 ± 3	47
3019.39	9.7 ± 0.7	8.9
3733.9	2.7 ± 0.3	2.4
4143.67	1.5 ± 0.2	1.7

Table A.13. Branching ratios for the $E_x = 7203.0$ keV resonance.

E_f (keV)	Present Work BR (%)	Previous Work BR (%)
677.29	0.24 ± 0.08	–
709.02	3.8 ± 0.5	2.6
1454.67	2.0 ± 0.2	2.4
1973.62	1.0 ± 0.1	1.3
2539.03	0.16 ± 0.04	–
2723.96	1.5 ± 0.1	2.1
2937.87	86 ± 4	86
4422.4	0.30 ± 0.06	0.6
5508.6	4.7 ± 0.2	5.0
6006.07 [a]	0.25 ± 0.05	–

[a] From [Wal96].

Table A.14. Branching ratios for the $E_x = 7207.5$ keV resonance.

E_f (keV)	Present Work BR (%)	Previous Work BR (%)
709.02	5.8 ± 0.9	–
3019.39	72 ± 3	80
3733.9	3.7 ± 0.3	–
4937.9	3.1 ± 0.2	–
5506.1	15.7 ± 0.7	20

Table A.15. Branching ratios for the $E_x = 7223.3$ keV resonance.

E_f (keV)	Present Work[a] BR (%)	Previous Work BR (%)
0.0	19.1 ± 0.9	22
709.02	10.8 ± 0.6	10
1454.67	4.7 ± 0.3	5.8
1973.62	0.9 ± 0.1	0.4
2539.03	0.8 ± 0.1	0.7
2839.9	1.2 ± 0.1	1.5
3019.39	4.5 ± 0.3	2.8
3733.9	2.3 ± 0.1	2.4
4143.67	47 ± 2	45
4232.2	–	0.5
4626.55	9.3 ± 0.4	8.9

[a] Corrected for angular distribution effects.

Table A.16. Branching ratios for the $E_x = 7282.0$ keV resonance.

E_f (keV)	Present Work BR (%)	Previous Work BR (%)
1454.67	27 ± 1	28
2539.03	5.2 ± 0.2	4.9
2723.96	4.9 ± 0.2	5.0
2839.9	3.3 ± 0.2	3.1
2937.87	45 ± 2	46
3835.9	0.18 ± 0.03	–
4182.65	13.7 ± 0.6	13
5576.9	0.65 ± 0.05	–

Table A.17. Branching ratios for the $E_x = 7283.4$ keV resonance.

E_f (keV)	Present Work BR (%)	Previous Work BR (%)
0.0	19.0 ± 0.8	21
677.29	2.3 ± 0.1	1.7
709.02	2.0 ± 0.1	1.9
1454.67	3.4 ± 0.2	3.3
2723.96	11.6 ± 0.5	11
2937.87	0.51 ± 0.06	1.5
3733.9	5.9 ± 0.3	4.3
3835.9	2.9 ± 0.1	2.0
3928.9	0.55 ± 0.05	–
4422.4	35 ± 1	37
4736.4	3.7 ± 0.2	4.3
4941.0	10.2 ± 0.4	12
5206.4	2.8 ± 0.1	–

Appendix B

Results of RUL Analyses

This appendix summarizes in tables the main results of the RUL analyses performed on the 17 resonances studied in this work. In each table are listed the possible $J^\pi;T$ values which have been eliminated because the strength of at least one transition exceeded twice its respective *recommended upper limit* (RUL). Also listed are the final energy level of the transition, the transition character, reduced transition strength, and the RUL which would be applicable for a particular $J^\pi;T$ value. If several reduced transition strengths B exceeded their associated RULs [End93], the two transition strengths that exceeded their RUL by the greatest amount were listed in the table. No RULs for E3 isovector transitions were listed in Endt [End93] since transitions of this type were not observed in the experimental work included in that compilation.

However, for possible mixed M2 and E3 isovector (M2/E3 IV) transitions, a $B = 100$ W.u. was considered in this work an appropriate upper limit for the E3 component of these transitions. Also, for mixed multipolarity transitions with unknown mixing ratios, the reduced transitions strength B computed by assuming a *pure* transition for each component was listed separately in the table. In contrast, the B's listed for each component of mixed transitions with known mixing ratios (see table B.15) were computed using these ratios.

As noted in Sect. 5.6, the resonances at $E_x = 7045.0$ and 7207.5 keV have transitions that are not eliminated for a particular range of mixing ratios. These transitions were also included in the tables for these two resonances. Also, as discussed in Sect. 5.6, Γ_γ has not

been measured for the new resonances at $E_x = 6597.7, 6873.4$, and 7119.1 keV and also for the 6667.8 keV resonance. Therefore, only lower limits on the B's that were compared to their appropriate RULs were listed in the tables for these four resonances. For consistency, the footnotes to these tables follow the format of Wallace [Wal96].

Table B.1. Summary of RUL analysis for the $E_x = 6597.7$ keV resonance.

$J^\pi;T$ Assignment	E_f (keV)	$J^\pi;T$ (Final)	Transition Type	B (W.u.)	RUL (W.u.)
$2^+;0$	4232	$4^-;0$	M2/E3 IS	14.8/18,700	0.2/50
$2^+;1$	4232	$4^-;0$	M2/E3 IV	14.8/18,700	0.2/‡
$2^-;0$	4298	$4^+;0$	M2/E3 IS	13.8/18,400	0.2/50
$2^-;1$	4298	$4^+;0$	M2/E3 IV	13.8/18,400	5/‡

‡ No RUL given in [End93].

Table B.2. Summary of RUL analysis for the $E_x = 6667.8$ keV resonance.

$J^\pi;T$ Assignment	E_f (keV)	$J^\pi;T$ (Final)	Transition Type	B (W.u.)	RUL (W.u.)
$1^+;0$	4232	$4^-;0$	E3 IS	94,000	50
	4627	$3^-;0$	M2/E3 IS	191/324,000	0.2/50
$1^+;1$	4232	$4^-;0$	E3 IV	94,000	‡
	4627	$3^-;0$	M2/E3 IV	191/324,000	5/‡
$2^+;0$	4232	$4^-;0$	M2/E3 IS	47.3/56,400	0.2/50
$2^+;1$	4232	$4^-;0$	M2/E3 IV	47.3/56,400	5/‡
$3^-;0$	3019	$1^+;0$	M2/E3 IS	0.560/297	0.2/50
	3734	$1^+;0$	M2/E3 IS	54.1/44,500	0.2/50
$3^-;1$	3734	$1^+;0$	M2/E3 IV	54.1/44,500	5/‡
$4^-;0$ §	2938	$2^+;1$	M2/E3 IV	101/51,500	5/‡
	4183	$2^+;1$	M2/E3 IV	282/32,300	5/‡
$4^-;1$ §	2938	$2^+;1$	M2/E3 IS	101/51,500	0.2/50
	4183	$2^+;1$	M2/E3 IS	282/32,300	0.2/50

§ B of more than two transitions exceed twice their associated RUL.

‡ No RUL given in [End93].

Table B.3. Summary of RUL analysis for the $E_x = 6853.9$ keV resonance.

$J^\pi;T$ Assignment	E_f (keV)	$J^\pi;T$ (Final)	Transition Type	B (W.u.)	RUL (W.u.)
$1^-;0$ §	2539	$3^+;0$	M2/E3 IS	9.66/3670	0.2/50
	3929	$3^+;0$	M2/E3 IS	42.6/35,200	0.2/50
$1^-;1$	3929	$3^+;0$	M2/E3 IV	42.6/35,200	5/‡
$2^+;0$	4468	$0^+;1$	E2 IV	44.1	5
$2^-;0$	677	$0^+;1$	M2 IV	180	5
	4468	$0^+;1$	M2 IV	1390	5
$2^-;1$	677	$0^+;1$	M2 IS	180	0.2
	4468	$0^+;1$	M2 IS	1390	0.2
$3^-;0$ §	677	$0^+;1$	E3 IV	23,800	‡
	4468	$0^+;1$	E3 IV	†	‡
$3^-;1$ §	677	$0^+;1$	E3 IS	23,800	50
	4468	$0^+;1$	E3 IS	†	50

§ B of more than two transitions exceed twice their associated RUL.

† $B > 10^7$ W.u.

‡ No RUL given in [End93].

Table B.4. Summary of RUL analysis for the $E_x = 6873.4$ keV resonance.

$J^\pi;T$ Assignment	E_f (keV)	$J^\pi;T$ (Final)	Transition Type	B (W.u.)	RUL (W.u.)
$1^+;0$	4232	$4^-;0$	E3 IS	94,400	50
$1^+;1$	4232	$4^-;0$	E3 IV	94,400	‡
$2^+;0$	4232	$4^-;0$	M2/E3 IS	55.9/56,600	0.2/50
$2^+;1$	4232	$4^-;0$	M2/E3 IV	55.9/56,600	5/‡
$4^-;0$ §	1455	$2^+;0$	M2/E3 IS	18.6/4470	0.2/50
	4183	$2^+;1$	M2/E3 IV	79.9/78,000	5/‡
$4^-;1$ §	1455	$2^+;0$	M2/E3 IV	18.6/4470	5/‡
	4183	$2^+;1$	M2/E3 IS	79.9/78,000	0.2/50

§ B of more than two transitions exceed twice their associated RUL.

‡ No RUL given in [End93].

Table B.5. Summary of RUL analysis for the $E_x = 6876.5$ keV resonance.

$J^\pi;T$ Assignment	E_f (keV)	$J^\pi;T$ (Final)	Transition Type	B (W.u.)	RUL (W.u.)
$0^-;0$ §	1455	$2^+;0$	M2 IS	51.9	0.2
	2724	$2^+;0$	M2 IS	109	0.2
$0^-;1$ §	2938	$2^+;1$	M2 IS	85.6	0.2
	4183	$2^+;1$	M2 IS	286	0.2
$3^-;0$ §	0	$1^+;0$	M2/E3 IS	23.6/3500	0.2/50
	3019	$1^+;0$	M2/E3 IS	27.1/12,900	0.2/50
$3^-;1$ §	0	$1^+;0$	M2/E3 IV	23.6/3500	5/‡
	3019	$1^+;0$	M2/E3 IV	27.1/12900	5/‡
$4^-;0$ §	3019	$1^+;0$	E3 IS	10,000	50
	4183	$2^+;1$	M2/E3 IS	31.8/30,900	0.2/50
$4^-;1$ §	3019	$1^+;0$	E3 IV	10,000	‡
	4183	$2^+;1$	M2/E3 IV	31.8/30,900	5/‡

§ B of more than two transitions exceed twice their associated RUL.

‡ No RUL given in [End93].

Table B.6. Summary of RUL analysis for the $E_x = 6921.0$ keV resonance.

$J^\pi;T$ Assignment	E_f (keV)	$J^\pi;T$ (Final)	Transition Type	B (W.u.)	RUL (W.u.)
$1^+;1$	677	$0^+;1$	M1 IS	0.141	0.05
	4468	$0^+;1$	M1 IS	0.480	0.05
$1^-;1$	677	$0^+;1$	E1 IS	0.005	0.002
	4468	$0^+;1$	E1 IS	0.016	0.002
$2^+;0$	677	$0^+;1$	E2 IV	10.1	5
	4468	$0^+;1$	E2 IV	222	5
$2^+;1$	4468	$0^+;1$	E2 IS	222	100
$2^-;0$	677	$0^+;1$	M2 IV	317	5
	4468	$0^+;1$	M2 IV	6990	5
$2^-;1$	677	$0^+;1$	M2 IS	317	0.2
	4468	$0^+;1$	M2 IS	6990	0.2
$3^-;0$ §	4468	$0^+;1$	E3 IV	†	‡
	4502	$1^+;1$	M2/E3 IV	1110/†	5/‡
$3^-;1$ §	4468	$0^+;1$	E3 IS	†	50
	4502	$1^+;1$	M2/E3 IS	371/44,800	0.2/50

§ B of more than two transitions exceed twice their associated RUL.

† $B > 10^7$ W.u.

‡ No RUL given in [End93].

Table B.7. Summary of RUL analysis for the $E_x = 6978.3$ keV resonance.

$J^\pi;T$ Assignment	E_f (keV)	$J^\pi;T$ (Final)	Transition Type	B (W.u.)	RUL (W.u.)
$2^-;0$	4344	$5^+;0$	E3 IS	12,900	50
$2^-;1$	4344	$5^+;0$	E3 IV	12,900	‡
$4^-;0$	2724	$2^+;0$	M2/E3 IS	1.35/526	0.2/50
$5^-;0$ §	2539	$3^+;0$	M2/E3 IS	0.891/320	0.2/50
	3929	$3^+;0$	M2/E3 IS	5.53/4210	0.2/50
$5^-;1$ §	2539	$3^+;0$	M2/E3 IV	0.891/320	5/‡
	3929	$3^+;0$	M2/E3 IV	5.53/4210	5/‡

§ B of more than two transitions exceed twice their associated RUL.

‡ No RUL given in [End93].

Table B.8. Summary of RUL analysis for the $E_x = 7014.9$ keV resonance.

$J^\pi;T$ Assignment	E_f (keV)	$J^\pi;T$ (Final)	Transition Type	B (W.u.)	RUL (W.u.)
$1^-;0$	1974	$3^+;0$	M2/E3 IS	2.27/632	0.2/50
	2539	$3^+;0$	M2/E3 IV	45.9/16,200	5/‡
$1^-;1$	2539	$3^+;0$	M2/E3 IV	45.9/16,200	5/‡
	4627	$3^-;0$	E2 IV	25.9	5
$1^+;0$	4627	$3^-;0$	M2/E3 IS	815/†	0.2/50
$1^+;1$	4627	$3^-;0$	M2/E3 IV	815/†	5/‡
$2^-;1$	4502	$1^+;1$	E1 IS	0.005	0.002
$3^+;0$	4502	$1^+;1$	E2 IV	74.7	5
$3^-;0$ §	3019	$1^+;0$	M2/E3 IS	90.7/40200	0.2/50
	4502	$1^+;1$	M2/E3 IV	2350/†	5/‡
$3^-;1$ §	3019	$1^+;0$	M2/E3 IV	90.7/40,200	5/‡
	4502	$1^+;1$	M2/E3 IS	2350/†	0.2/50
$4^-;0$ §	3019	$1^+;0$	E3 IS	31,200	50
	4502	$1^+;1$	E3 IV	†	‡
$4^-;1$ §	4183	$2^+;1$	M2/E3 IS	77.3/68100	0.2/50
	4502	$1^+;1$	E3 IS	†	50

§ B of more than two transitions exceed twice their associated RUL.

† $B > 10^7$ W.u.

‡ No RUL given in [End93].

Table B.9. Summary of RUL analysis for the $E_x = 7045.0$ keV resonance.

$J^\pi;T$ Assignment	E_f (keV)	$J^\pi;T$ (Final)	Transition Type	B (W.u.)	RUL (W.u.)
$2^+;1$	6095	$3^-;1$	E1 IS	0.005	0.002
$2^-;1$	6095	$3^-;1$	M1/E2 IS	0.162/832	0.05/100
$3^-;1$ [a]	6095	$3^-;1$	M1/E2 IS	0.115/594	0.05/100

[a] This transition not eliminated for $0.396 \leq \delta_{E2/M1} \leq 0.712$,

Table B.10. Summary of RUL analysis for the $E_x = 7049.4$ keV resonance.

$J^\pi;T$ Assignment	E_f (keV)	$J^\pi;T$ (Final)	Transition Type	B (W.u.)	RUL (W.u.)
$1^+;0$ §	4232	$4^-;0$	E3 IS	†	50
	4926	$3^-;0$	M2/E3 IS	25,400/†	0.2/50
$1^+;1$ §	4232	$4^-;0$	E3 IV	†	‡
	4926	$3^-;0$	M2/E3 IV	25,400/†	5/‡
$2^+;0$ §	4232	$4^-;0$	M2/E3 IS	11,500/†	0.2/50
	4926	$3^-;0$	E1 IS	0.016	0.002
$2^+;1$	4232	$4^-;0$	M2/E3 IV	11,500/†	5/‡
$2^-;0$ §	4232	$4^-;0$	E2 IS	366	100
	4627	$3^-;0$	M1/E2 IS	0.290/229	0.05/100
$2^-;1$	4232	$4^-;0$	E2 IV	366	5
$3^+;0$ §	4232	$4^-;0$	E1 IS	0.015	0.002
	4926	$3^-;0$	E1 IS	0.011	0.002
$3^-;0$	4232	$4^-;0$	M1/E2 IS	0.447/261	0.05/100
	4627	$3^-;0$	M1/E2 IS	0.207/163	0.05/100
$4^+;0$ §	4232	$4^-;0$	E1 IS	0.011	0.002
	4926	$3^-;0$	E1 IS	0.009	0.002
$4^-;0$ §	4232	$4^-;0$	M1/E2 IS	0.348/203	0.05/100
	4926	$3^-;0$	M1/E2 IS	0.261/269	0.05/100
$5^-;0$ §	2840	$3^+;0$	M2/E3 IS	50.0/19,900	0.2/50
	3929	$3^+;0$	M2/E3 IS	79.7/57,800	0.2/50
$5^-;1$ §	3929	$3^+;0$	M2/E3 IV	79.7/57,800	5/‡
	4926	$3^-;0$	E2 IV	220	5

§ B of more than two transitions exceed twice their associated RUL.

† $B > 10^7$ W.u.

‡ No RUL given in [End93].

Table B.11. Summary of RUL analysis for the $E_x = 7119.1$ keV resonance.

$J^\pi;T$ Assignment	E_f (keV)	$J^\pi;T$ (Final)	Transition Type	B (W.u.)	RUL (W.u.)
$1^-;0$	1974	$3^+;0$	M2/E3 IS	2.50/667	0.2/50
	2539	$3^+;0$	M2/E3 IS	2.03/683	0.2/50
$4^-;0$	2938	$2^+;1$	M2/E3 IV	26.4/10,700	5/‡
$4^-;1$	2938	$2^+;1$	M2/E3 IS	26.4/10,700	0.2/50

‡ No RUL given in [End93].

Table B.12. Summary of RUL analysis for the $E_x = 7177$ keV resonance.

$J^\pi;T$ Assignment	E_f (keV)	$J^\pi;T$ (Final)	Transition Type	B (W.u.)	RUL (W.u.)
$2^-;0$	677	$0^+;1$	M2 IV	52.9	5
$2^-;1$	677	$0^+;1$	M2 IS	52.9	0.2
$3^-;0$ §	709	$1^+;0$	M2/E3 IS	167/28,200	0.2/50
	3019	$1^+;0$	M2/E3 IS	314/12,900	0.2/50
$3^-;1$ §	709	$1^+;0$	M2/E3 IV	167/28,200	5/‡
	3019	$1^+;0$	M2/E3 IV	314/12,900	5/‡

§ B of more than two transitions exceed twice their associated RUL.

‡ No RUL given in [End93].

Table B.13. Summary of RUL analysis for the $E_x = 7203.0$ keV resonance.

$J^\pi;T$ Assignment	E_f (keV)	$J^\pi;T$ (Final)	Transition Type	B (W.u.)	RUL (W.u.)
$1^-;0$	1974	$3^+;0$	M2/E3 IS	5.40/1400	0.2/50
	2539	$3^+;0$	M2/E3 IS	1.53/498	0.2/50
$1^-;1$	2938	$2^+;1$	E1 IS	0.005	0.002
$3^-;0$	709	$1^+;0$	M2/E3 IS	2.98/499	0.2/50

Table B.14. Summary of RUL analysis for the $E_x = 7207.5$ keV resonance.

$J^\pi;T$ Assignment	E_f (keV)	$J^\pi;T$ (Final)	Transition Type	B (W.u.)	RUL (W.u.)
$0^+;0$	3019	$1^+;0$	M1 IS	0.227	0.05
	5506	$1^+;0$	M1 IS	0.738	0.05
	5506	$1^-;0$	E1 IS	0.024	0.002
$0^-;0$	3019	$1^+;0$	E1 IS	0.007	0.002
	5506	$1^+;0$	E1 IS	0.024	0.002
	5506	$1^-;0$	M1 IS	0.738	0.05
$1^+;0$	5506	$1^+;0$	M1/E2 IS	0.246/394	0.05/100
	5506	$1^-;0$	E1 IS	0.008	0.002
$1^-;0$	5506	$1^+;0$	E1 IS	0.008	0.002
	5506	$1^-;0$	M1/E2 IS	0.246/394	0.05/100
$2^+;0$	5506	$1^+;0$ [a]	M1/E2 IS	0.148/237	0.05/100
	5506	$1^-;0$	E1 IS	0.005	0.002
$2^-;0$	5506	$1^+;0$	E1 IS	0.005	0.002
	5506	$1^-;0$ [a]	M1/E2 IS	0.148/237	0.05/100
$3^+;1$	5506	$1^+;0$	E2 IV	169	5
	5506	$1^-;0$	M2/E3 IV	5320/†	5/‡
$3^-;0$ §	3019	$1^+;0$	M2/E3 IS	270/109,000	0.2/50
	3734	$1^+;0$	M2/E3 IS	35.3/20,700	0.2/50
$3^-;1$ §	3019	$1^+;0$	M2/E3 IV	270/109,000	5/‡
	5506	$1^+;0$	M2/E3 IV	5320/†	5/‡
	5506	$1^-;0$	E2 IV	169	5

[a] This transition not eliminated for $0.668 \leq \delta_{E2/M1} \leq 2.51$.

§ B of more than two transitions exceed twice their associated RUL.

† $B > 10^7$ W.u.

‡ No RUL given in [End93].

Table B.15. Summary of RUL analysis for the $E_x = 7223.3$ keV resonance.

$J^\pi;T$ Assignment	E_f (keV)	$J^\pi;T$ (Final)	Transition Type	B (W.u.)	RUL (W.u.)
$1^+;0$	4144	$2^-;0$	E1 IS	0.047	0.002
$1^+;1$	4627 [a]	$3^-;0$	M2/E3 IV	10,200/95.9	5/‡
$1^-;0$ §	2539	$3^+;0$	M2/E3 IS	45.8/14,800	0.2/50
	2840	$3^+;0$	M2/E3 IS	95.7/35,200	0.2/50
$1^-;1$ §	2539	$3^+;0$	M2/E3 IV	45.8/14,800	5/‡
	2840	$3^+;0$	M2/E3 IV	95.7/35,200	5/‡
$2^+;0$	4144	$2^-;0$	E1 IS	0.028	0.002
	4627	$3^-;0$	E1 IS	0.009	0.002
$2^-;0$	4144 [a]	$2^-;0$	M1/E2 IS	0.851/1.60	0.05/100
	4627 [a]	$3^-;0$	M1/E2 IS	0.282/0.002	0.05/100
$3^+;0$	4144	$2^-;0$	E1 IS	0.020	0.002
	4627	$3^-;0$	E1 IS	0.007	0.002
$3^-;0$ §	3019	$1^+;0$	M2/E3 IS	190/75,800	0.2/50
	3734	$1^+;0$	M2/E3 IS	246/143,000	0.2/50
$3^-;1$ §	3019	$1^+;0$	M2/E3 IV	190/75,800	5/‡
	3734	$1^+;0$	M2/E3 IV	246/143,000	5/‡
$4^-;0$ §	3019	$1^+;0$	E3 IS	59,000	50
	3734	$1^+;0$	E3 IS	111,000	50
$4^-;1$	1455	$2^+;0$	M2/E3 IV	31.7/6730	5/‡
	4144	$2^-;0$	E2 IV	232	5

§ B of more than two transitions exceed twice their associated RUL.

‡ No RUL given in [End93].

[a] mixing ratio is known for this transition

Table B.16. Summary of RUL analysis for the $E_x = 7282.0$ keV resonance.

$J^\pi;T$ Assignment	E_f (keV)	$J^\pi;T$ (Final)	Transition Type	B (W.u.)	RUL (W.u.)
$0^-;0$ §	1455	$2^+;0$	M2 IV	733	5
	2938	$2^+;1$	M2 IV	5300	5
$0^-;1$ §	2938	$2^+;1$	M2 IS	5300	0.2
	4183	$2^+;1$	M2 IS	8740	0.2
$1^-;0$	2539	$3^+;0$	M2/E3 IS	132/41,400	0.2/50
	2840	$3^+;0$	M2/E3 IS	116/41,600	0.2/50
$1^-;1$ §	2539	$3^+;0$	M2/E3 IV	132/41,400	5/‡
	2840	$3^+;0$	M2/E3 IV	116/41,600	5/‡
$2^-;1$	2938	$2^+;1$	E1 IS	0.005	0.002
$4^+;0$	2938	$2^+;1$	E2 IV	18.7	5
	4183	$2^+;1$	E2 IV	30.9	5
$4^-;0$ §	1455	$2^+;0$	M2/E3 IS	81.4/16,900	0.2/50
	2724	$2^+;0$	M2/E3 IS	50.5/17,200	0.2/50
$4^-;1$ §	4183	$2^+;1$	M2/E3 IS	971/714,000	0.2/50
	5577	$1^+;1$	E3 IS	†	50
	5577	$2^+;1$	M2/E3 IS	914/†	0.2/50
$5^-;0$	1455	$2^+;0$	E3 IS	13,900	50
	2724	$2^+;0$	E3 IS	14,000	50
$5^-;1$	1455	$2^+;0$	E3 IV	13,900	‡
	2724	$2^+;0$	E3 IV	14,000	‡

§ B of more than two transitions exceed twice their associated RUL.

† $B > 10^7$ W.u.

‡ No RUL given in [End93].

Table B.17. Summary of RUL analysis for the $E_x = 7283.4$ keV resonance.

$J^\pi;T$ Assignment	E_f (keV)	$J^\pi;T$ (Final)	Transition Type	B (W.u.)	RUL (W.u.)
$1^+;0$ §	4422	$2^+;0$	M1/E2 IS	1.31/743	0.05/100
	4941	$1^+;0$	M1/E2 IS	0.696/588	0.05/100
$1^+;1$	4736	$3^+;0$	E2 IV	140	5
	5206	$3^+;0$	E2 IV	295	5
	5206	$3^+;1$	E2 IS	295	100
$1^-;0$ §	3929	$3^+;0$	M2/E3 IS	166/104,000	0.2/50
	4736	$3^+;0$	M2/E3 IS	4410/†	0.2/50
$1^-;1$ §	4736	$3^+;0$	M2/E3 IV	4410/†	5/‡
	5206	$3^+;0$	M2/E3 IV	9260/†	5/‡
	5206	$3^+;1$	M2/E3 IS	9260/†	0.2/50
$2^+;0$	4941	$1^+;0$	M1/E2 IS	0.417/353	0.05/100
$2^-;0$ §	4422	$2^+;0$	E1 IS	0.026	0.002
	4941	$1^+;0$	E1 IS	0.014	0.002
$2^-;1$	677	$0^+;1$	M2 IS	14.0	0.2
$3^-;0$ §	3734	$1^+;0$	M2/E3 IS	574/322,000	0.2/50
	4941	$1^+;0$	M2/E3 IS	7929/†	0.2/50
$3^-;1$ §	3734	$1^+;0$	M2/E3 IV	574/322,000	5/‡
	4941	$1^+;0$	M2/E3 IV	7929/†	5/‡

§ B of more than two transitions exceed twice their associated RUL.

† $B > 10^7$ W.u.

‡ No RUL given in [End93].

Bibliography

[Ajz91] F. Ajzenberg-Selove, "The Energy levels of Light Nuclei $A = 13 - 15$", Nuclear Physics **A523**, 44 (1991).

[Aud93] G. Audi and A. H. Wapstra, "The 1993 Atomic Mass Evaluation (II) Nuclear Reaction and Separation Energies", Nuclear Physics **A565**, 66 (1993).

[Bev92] P. R. Bevington and K. Robinson, *Data Reduction and Error Analysis for the Physical Sciences*, McGraw-Hill, New York, second edition, 1992.

[Bie60] L. C. Biedenharn, "Angular Correlations in Nuclear Spectroscopy", in *Nuclear Spectroscopy, Part B*, edited by F. Ajzenberg-Selove, pages 732–810, Academic Press, New York, 1960.

[Bla52] J. M. Blatt and L. C. Biedenharn, "The Angular Distribution of Scattering and Reaction Cross Sections", Reviews of Modern Physics **24**, 258 (1952).

[Bla91] J. M. Blatt and V. F. Weisskopf, *Theoretical Nuclear Physics*, Dover Publications, Mineola, NY, 1991.

[Boh36] N. Bohr, "Neutron Capture and Nuclear Constitution", Nature **137**, 344 (1936).

[Boh69] A. Bohr and B. Mottelson, *Nuclear Structure*, W. A. Benjamin, New York, 1969.

[Boh84] O. Bohigas, M. J. Giannoni, and C. Schmit, "Characterization of Chaotic Quantum Spectra and Universality of Level Fluctuation Laws", Physical Review Letters **52**, 1 (1984).

[Boh85] O. Bohigas, R. U. Haq, and A. Pandey, "Higher-Order Correlations in Spectra of Complex Systems", Physical Review Letters **54**, 1645 (1985).

[Bro73] T. A. Brody, "A Statistical Measure for the Repulsion of Energy Levels", Lett. Nuovo Cimento **7** (1973).

[Bro81] T. A. Brody et al., "Random Matrix Physics: Spectrum and Strength Functions", Reviews of Modern Physics **53**, 385 (1981).

[Bul89] J. S. Bull, *Entrance Channel Correlations in* ^{40}Ca, Ph.D. thesis, Duke University, 1989.

[Byb95] C. R. Bybee, *Fourier Transform as Signature of Chaos in Nuclei and Data Acquisition for Compton-Suppressed Spectrometer*, Ph.D. thesis, North Carolina State University, 1995.

[Cor90] A. B. Corripio, *Tuning of Industrial Control Systems*, Instrument Society of America, Research Triangle Park, NC., first edition, 1990.

[Dra94] J. M. Drake, *Resonance Tests of Detailed Balance and Design of Compton Suppression Spectrometer*, Ph.D. thesis, North Carolina State University, 1994.

[Dys62] F. J. Dyson, "A Brownian-Motion Model for the Eigenvalues of a Random Matrix", Journal of Mathematical Physics **3**, 1191 (1962).

[Dys63] F. J. Dyson and M. L. Mehta, "Statistical Theory of the Energy Levels of Complex Systems. IV", Journal of Mathematical Physics **4**, 701 (1963).

[End78] P. M. Endt and C. V. der Leun, "Energy levels of A = 21-44 nuclei", Nuclear Physics **A310**, 285 (1978).

[End86] P. M. Endt, P. de Wit, and C. Alderliesten, "The ^{25}Mg(p, γ)^{26}Al and ^{25}Mg(p, p$'$) Resonances for $E_p = 0.31 - 1.84$ MeV", Nuclear Physics **A459**, 61 (1986).

[End88a] P. M. Endt, P. de Wit, and C. Alderliesten, "The ^{25}Mg(p, γ)^{26}Al Reaction; Branchings, Energies, and Lifetimes", Nuclear Physics **A476**, 333 (1988).

[End88b] P. M. Endt et al., "Spins parities and isospins of ^{26}Al levels: shell-model aspects", Nuclear Physics **A487**, 221 (1988).

[End90a] P. M. Endt, "Energy levels of $A = 21 - 44$ nuclei", Nuclear Physics **A521**, 1 (1990).

[End90b] P. M. Endt, C. Alderliesten, F. Zijderhand, A. A. Wolters, and A. G. M. van Hees, "Spectroscopic information on ^{24}Mg and ^{28}Si from proton capture", Nuclear Physics **A510**, 209 (1990).

[End93] P. M. Endt, "Gamma-ray transitions in $A = 5 - 44$ nuclei (IV)", Atomic Data and Nuclear Data Tables **55**, 171 (1993).

[Fer34] E. Fermi et al., Ricererca Scientifica **5**, 282 (1934).

[Fer65] A. J. Ferguson, *Angular Correlation Methods in Gamma-ray Spectroscopy*, North-Holland, Amsterdam, 1965.

[Fow48] W. A. Fowler, C. C. Lauritsen, and T. Lauritsen, "Gamma-Radiation from Excited States of Light Nuclei", Review of Modern Physics **20**, 236 (1948).

[Fra91] S. C. Frankle, *Nuclear Resonance Spectroscopy in ^{30}P*, Ph.D. thesis, North Carolina State University, 1991.

[Fra92] S. C. Frankle, G. E. Mitchell, J. F. Shriner, Jr., E. G. Bilpuch, and C. R. Westerfeldt, "Proton resonances in ^{30}P", Physical Review C **45**, 2746 (1992).

[Guh90] T. Guhr and H. A. Weidenmüller, "Isospin Mixing and Spectral Fluctuation Properties", Ann. Phys. **199**, 412 (1990).

[Haf35] L. R. Hafsted and M. A. Tuve, "Carbon Radioactivity and Other Resonance Transmutations by Protons", Physical Review **48**, 306 (1935).

[Haq82] R. U. Haq, A. Pandey, and O. Bohigas, "Fluctuation Properties of Nuclear Energy Levels: Do Theory and Experiment Agree?", Physical Review Letters **48**, 1086 (1982).

[Har69] G. I. Harris, A. K. Hyder, Jr., and J. Walinga, "Properties of ^{30}P Levels from the ^{29}Si(p,γ) Reaction (II)", Physical Review **187**, 1413 (1969).

[Hub54] R. Huby, "Phase of Matrix Elements in Nuclear Reactions and Radioactive Decay", Proceedings of the Physical Society **67A**, 1103 (1954).

[Jac75] J. D. Jackson, *Classical Electrodynamics*, John Wiley and Sons, New York, second edition, 1975.

[Joh94] G. W. Johnson, *LabView Graphical Programming*, McGraw-Hill, New York, first edition, 1994.

[Kno89] G. F. Knoll, *Radiation Detection and Measurement*, John Wiley & Sons, New York, second edition, 1989.

[Kra88] K. Krane, *Introductory Nuclear Physics*, John Wiley and Sons, 1988, 1988.

[LaB95] M. A. LaBonte, "Angular Distribution Study of the ^{29}Si(p,γ) Reaction", Master's thesis, North Carolina State University, 1995.

[Lan58] A. M. Lane and R. G. Thomas, "R-matrix Theory of Nuclear Reactions", Reviews of Modern Physics **30**, 257 (1958).

[Led78] C. M. Lederer and V. S. Shirley, *Table of Isotopes*, John Wiley & Sons, New York, seventh edition, 1978.

[Lio72] H. I. Liou et al., "Neutron Resonance Spectroscopy VIII. The Separated Isotopes of Erbium: Evidence of Dyson's Theory Concerning Level Spacings", Physical Review C **5**, 974 (1972).

[Mar68] J. B. Marion and F. C. Young, *Nuclear Reaction Analysis*, John Wiley & Sons, New York, 1968.

[Mit88] G. E. Mitchell et al., "Broken Symmetries and Chaotic Behavior in ^{26}Al", Physical Review Letters **61**, 1473 (1988).

[Moa51] C. D. Moak, H. Reese, Jr., and W. M. Good, "Proton resonances in ^{30}P", Nucleonics **9**, 19 (1951).

[Nel83a] R. O. Nelson, E. G. Bilpuch, C. R. Westerfeldt, and G. E. Mitchell, "Proton resonances in ^{30}P", Physical Review C **27**, 930 (1983).

[Nel83b] R. O. Nelson, *Proton Resonance Spectroscopy in ^{28}Si and ^{30}P*, Ph.D. thesis, Duke University, 1983.

[Pan81] A. Pandey, "Statistical Properties of Many-Particle Spectra. IV. New Ensembles by Stieltjes Transform Methods", Annals of Physics **134**, 110 (1981).

[Par58] P. B. Parks and R. M. Williamson, "Proton resonances in ^{30}P", Rev. Sci. Instrum. **29**, 834 (1958).

[Por65] C. E. Porter, editor, *Statistical Theories of Spectra: Fluctuations*, Academic, New York, 1965.

[Rad89] D. C. Radford, *GELIFT Reference Manual*, Chalk River Nuclear Laboratories, Chalk River, Ontario, 1989.

[Ram81] B. Ramstein and L. H. Rosier, "Investigation of States in ^{30}P Via the ^{30}Si(^{3}He,t) Reaction at 30 MeV", Nuclear Physics **A363**, 110 (1981).

[Rei85] J. P. L. Reinecke et al., "The energy levels of ^{30}P", Nuclear Physics **A435**, 333 (1985).

[Rii79] M. Riihonen, J. Keinonen, and A. Anttila, "Hydrogen Burning of $^{29-30}$Si in Explosive Carbon Burning", Nuclear Physics **A3**, 251 (1979).

[Rin80] P. Ring and P. Schuck, *The Nuclear Many-Body Problem*, Springer-Verlag, New York, 1980.

[Ros67] H. J. Rose and D. M. Brink, "Angular distributions of gamma rays in terms of phase-defined reduced matrix elements", Review of Modern Physics **39**, 306 (1967).

[Rut51] J. G. Rutherglen and J. F. Cole, "Proton resonances in ^{30}P", Nature **160**, 545 (1951).

[Sha54] W. T. Sharp et al., "Table of Coefficients for Angular Distribution Analysis", Technical Report CRT-556, Atomic Energy of Canada Limited, 1954.

[Shr90] J. F. Shriner, Jr. et al., "Fluctuation Properties of States in ^{26}Al", Zeitschrift für Physik A **335**, 393 (1990).

[Shr91] J. F. Shriner, Jr., G. E. Mitchell, and T. von Egidy, "Fluctuation Properties of Spacings of Low-Lying Nuclear Levels", Zeitschrift für Physik A **338**, 309 (1991).

[Shr95a] J. D. Shriner, 1995, private communication.

[Shr95b] J. F. Shriner, Jr., 1995, private communication.

[Sie87] P. J. Siemens and A. S. Jensen, *Elements of Nuclei: Many-Body Physics with the Strong Interaction*, Addison-Wesley, New York, 1987.

[Sim78] J. J. Simpson et al., "Isospin Impurity in the Compound Nucleus from a Comparison of Fluctuations in Mirror Reactions", Physical Review Letters **40**, 154 (1978).

[Sod87] J. P. Soderstrum, M. A. Boyd, C. R. Gould, and N. R. Roberson, *XSYS Reference Manual*, Triangle Universities Nuclear Laboratory, Durham, NC, sixth edition, 1987.

[Ver78] A. Vermeer and B. A. Strasters, "The Corona Stabilizer System of a Van de Graaff Generator", Nuclear Instrumentation and Methods **57**, 427 (1978).

[Vog59] E. Vogt, "Resonance Reactions, Theoretical", in *Nuclear Reactions, Volume 1*, edited by P. M. Endt and M. DeMeur, pages 215–258, North-Holland Publishing Company, Amsterdam, 1959.

[Wal96] P. M. Wallace, *A High Resolution Study of the $^{29}Si(p,\gamma)$ Reaction*, Ph.D. thesis, Duke University, 1996.

[Wat81] W. A. Watson, E. G. Bilpuch, and G. E. Mitchell, "Statistical Tests Applied to Proton Resonances in ^{57}Co", Zeitschrift für Physik A **300**, 89 (1981).

[Wei51] V. F. Weisskopf, "Transition probabilities in nuclei", Physical Review **83**, 1073 (1951).

[Wes87] C. R. Westerfeldt, R. O. Nelson, E. G. Bilpuch, and G. E. Mitchell, *The TUNL High Resolution Laboratory System and Operating Procedures*, Triangle Universities Nuclear Laboratory, Durham, NC, second edition, 1987.

[Wes88] C. R. Westerfeldt, R. O. Nelson, E. G. Bilpuch, and G. E. Mitchell, "A microcomputer-based system for measuring excitation functions with good energy resolution", Nuclear Instruments and Methods in Physics Research **A270**, 467 (1988).

[Wes95] C. R. Westerfeldt, J. F. Shriner, Jr., and G. A. Vavrina, *The TUNL High Resolution Laboratory System and Operating Procedures*, Triangle Universities Nuclear Laboratory, Durham, NC, third edition, 1995.

[Wig47] E. P. Wigner and L. Eisenbud, "Higher Angular Momenta and Long Range Interaction in Resonance Reactions", Physical Review **72**, 29 (1947).

[Wig57] E. P. Wigner, "Statistical Properties of Real Symmetric Matrices with Many Dimensions", Can. Math. Congr. Proc. (1957).

[Wil60] D. H. Wilkinson, "Analysis of Gamma Decay Data", in *Nuclear Spectroscopy, Part B*, edited by F. Ajzenberg-Selove, pages 852–889, Academic Press, New York, 1960.

[Wim74] J. F. Wimpey, *Electromagnetic Decay of Fragmented Analogue States in ^{45}Sc and ^{63}Cu*, Ph.D. thesis, North Carolina State University, 1974.